POLITECNICO
MILANO 1863

School of Industrial and Information Engineering
Master of Science in Mechanical Engineering

Selective Laser Beam Melting of AlSi10Mg Alloy

Supervisor: Prof. Carlo Alberto BIFFI

Assistant Supervisor: Dr. Jacopo FIOCCHI
                        Dr. Alessandro CONSALVO
                        Dr. Ausonio TUISSI

Master of Science Thesis of:
Edoardo FELLA I.D.823163

Academic Year 2015/2016

Ringraziamenti

Prima di cominciare vorrei dedicare qualche parola a chi mi ha supportato in tutto questo cammino, aiutandomi a superare le difficoltà (che non sono state poche).

Ringrazio il prof. Carlo Biffi per avermi proposto questo argomento di tesi sicuramente innovativo, dandomi la possibilità di entrare nel mondo del lavoro. Ringrazio anche i membri del CNR di Lecco per avermi affiancato nell'utilizzo dei diversi strumenti resi disponibili per la mia ricerca. Un ringraziamento particolare lo dedico a Jacopo Fiocchi per il costante supporto ed impegno mostrato nei miei confronti. Grazie!

Ringrazio l'azienda Renishaw S.p.A. per avermi dato l'opportunità di lavorare a contatto con la macchina laser in maniera autonoma. Grazie in particolare ad Enrico Orsi, Alessandro Consalvo ed Andrea Penna per avermi trasmesso tutte le conoscenze necessarie per poter svolgere al meglio il mio lavoro. Ovviamente non dimentico tutti i colleghi che mi hanno accolto alleggerendo il peso della distanza. Grazie!

E come dimenticarsi dei miei compagni di studio ma soprattutto compagni di vita, persone che hanno lasciato una traccia indelebile nei miei ricordi. Ringrazio Matteo Carzaniga, Paolo Stangoni, Micheal Caggio, Francesco Corti, Angelo Cattaneo, Pietro Maroni e Stefano Mauri per essere stati dei compagni di risate in momenti difficili. Auguro a tutti loro il meglio dalla vita! Ci si vede presto! Grazie ragazzi!!!!

E che dire di loro, quel fantastico gruppo di amici che mi accompagna da una vita, che mi ha visto crescere ed arrivare fin qui. Siete stati la mia forza e la mia distrazione, insomma il giusto mix per raggiungere l'obiettivo: la Laurea. Grazie di Cuore!!!!!

Un immenso GRAZIE lo dedico alla mia famiglia, per avermi dato la possibilità di costruirmi un futuro e per aver creduto costantemente in me. Grazie Mamma, per la fiducia dimostrata in tutti questi anni e grazie Papà per avermi fatto sentire 'Tutto Cervello' anche quando non passavo un esame. Siete la mia fonte di ispirazione. Grazie al mio fratellone, per l'orgoglio dimostrato ogni giorno nei miei confronti, sei stato e sarai sempre la mia marcia in più. Grazie al mio fratellino, che in un modo o nell'altro mi ha dato modo di sfogare il troppo studio. Sei il mio costante svago.

Infine voglio ringraziare la mia ragazza Erica, che subentrata in corsa ha dato una sterzata alla mia vita in tutti i sensi, rimettendo ordine ed aiutandomi a gestirla meglio. Tu hai vissuto da più vicino il mio percorso di studio scollegandomi da tutto quando era troppo. Grazie per esserci sempre stata, ma soprattutto grazie per essere qui di fianco a me in questo momento che non dimenticherò mai. Sei la mia Donna. Grazie Davvero!!

Contents

Chapter 1

State Of Art

Chapter 2

Chapter 3

Chapter 4

Chapter 5

Figure List

Table List

Abstract

The aim of this thesis work is an experimental study concerning the characterization of AlSi10Mg alloy produced via additive manufacturing (AM) with the technology of powder bed laser melting.

The work has been focused on the study of the laser melting process on mechanical and microstructural properties of the material produced. Experiments have been performed by using AlSi10Mg powder and *Renishaw AM250* machine provided with a pulsed wave laser of ytterbium fiber.

Design of experiments was implemented in order to study the effect of the main process parameters, such as power, interaction time and build plate temperature, on porosity, microstructure, calorimetric and mechanical properties.

Key Words: AlSi10Mg, powder bed laser melting, selective laser beam melting, additive manufacturing.

Sommmario

L'obbiettivo di questa tesi è lo studio sperimentale riguardante la caratterizzazione della lega AlSi10Mg prodotta tramite Produzione Additiva attraverso la tecnologia della fusione laser su letto di polvere

Il lavoro è stato focalizzato sullo studio del processo di fusione laser sulle proprie proprietà microstrutturali e meccaniche del materiale prodotto. Gli esperimenti sono stati eseguiti utilizzando polvere di AlSi10Mg e la macchina *Renishaw AM250* fornita di un laser ad onda pulsata in fibra all'Itterbio.

Il design degli esperimenti sono stati implementati per studiare l'effetto dei parametri principali di processo, come potenza, tempo di interazione e temperatura della piastra, sulla porosità, microstruttura, e proprietà meccaniche e calorimetriche

Parole chiave: AlSi10Mg, fusione laser su letto di polvere, fusione laser selettiva, produzione additiva.

Introduction

The powder bed laser melting is an additive manufacturing technique able to process any type of metallic material in order to produce items with a good accuracy and relevant mechanical properties comparable and often superior to those of conventionally produced parts.

At the beginning of the development of the technology for the metal additive, the focus was primarily to obtain parts ensuring that the overall appearance, dimensions and surface finish were satisfactory; in particular, it was necessary to ensure that users were satisfied from the point of view of the visual examination and dimensional measurement. The transition from metal sintering to the metal melting has made possible to transfer this technology to different fields, for example the dental one, where finish and detail are fundamental for clinical and aesthetic requirements. Also the residual porosity has its importance in dental sector, but is limited to values that prevent the formation of bubbles in the ceramic during the passages in furnaces, performed to achieve the aesthetic coating. Similar observations can be made for the medical sectors, where the customized production and the qualification requirements are very limited but easier to fulfill than those for other areas. The dental application has reached its peak of success in the recent past but nowadays, the additive manufacturing technology has been transferred to other sectors, where the requirements begin to be more limited and difficult to reach. The application fields in question are the aviation, power generation and specialized automotive fields. All these sectors have different mechanical and metallurgical requirements that need to be satisfied in terms of fatigue resistance, residual porosity and dimensional quality. Just think to the fatigue resistance requirements influenced by different factors such as the porosity, the geometry and the operating environment. In all these cases, the lean manufacturing will only works if there are a number of regulatory conditions favorable and if the materials are better known than they are now.

Additive Manufacturing

Additive manufacturing (AM) is a term used to describe the technologies that build 3D objects from a digital model by adding layer-upon-layer of material in different 2D shapes (www.renishaw.com). The principle of additive manufacturing can also be known by other names, including ALM (Additive Layer Manufacturing), 3D printing and laser melting or sintering.

This process is composed by different phases (see Fig.1). At first a 3D object is designed using CAD design software. This file is then converted into the required type used by the 3D printing / additive manufacturing machine, using a file preparation software interface. The geometry is then divided into individual slices of constant thickness creating a 2D representation of the object. The additive manufacturing system is filled with the desired material, which may be plastics, metal powders or wood. These consumables are used by the 3D printer to 'print' the final object, layer by layer. Various materials require different systems for fusing the layers together. On metal systems the materials are atomized metal powders that are fully melted to join the layers together.

The process takes place in an inert chamber full of argon to ensure that no chemical transformation (such as oxidation) will degrade the mechanical properties and, in general, the final quality of the product. The powder size is lower than 60 µm and it is consolidated by using a high energy density fiber laser. The powder is deposited on a mobile build plate, which moves along the z axis, and it has a thin layer thickness between 25 and 50 µm. After the powder distribution on the build plate, the laser beam scans the powder bed and melt the new layer (see Fig.1) on the x-y plane with the previous layer and after the build plate lowering the process restarts.
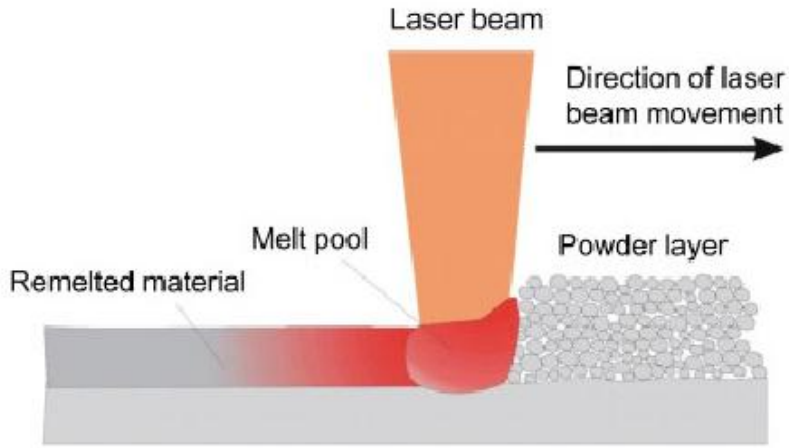
Fig.1: Schematic representation of power bed laser melting.

The process is repeated, building up complex geometries, layer by layer, until the part has been completed (see Fig.2).
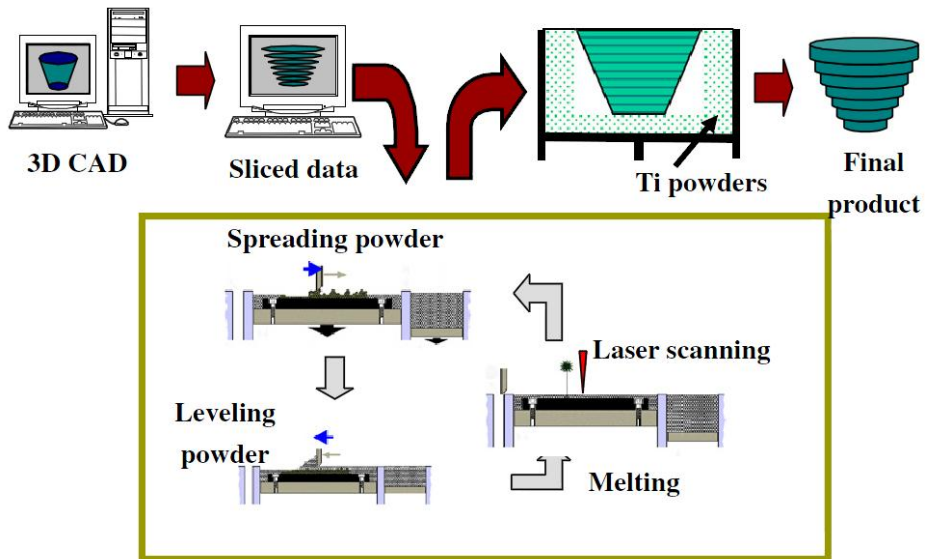
Fig.2: Schematic representation of the laser fusion process (Deepak K., 2011).

Different factors influence the final density and the mechanical properties of the laser melting fabricated component; some factors are correlated to physical components of the system (for example the type of the laser), other are linked to the adjustment actuated during the installation phase of the machine and they are no longer updated, just in case of maintenance (for example the settings of the collimation and of the focusing of the laser beam). Finally there are those factors on which it is possible to interfere in order to adjust the laser melting modes, the so called *process parameters*. They need to be optimized by considering the metallic alloy which will be used during the process, in order to avoid defects inside the final component. These parameters include the laser beam power, the thickness layer with which the 3D model is sliced, the hatching distance that is the distance among two parallel scanning tracks, and the interaction time between powder and laser beam. Differently from other powder bed laser melting machines, in this research it has been used a laser melting machine generating a not continuous scan track; each scan track is composed by a series of points with the same distance from each other. In fact, it is possible to consider the point distance and the exposition time as a variable process parameters, rather than the scanning velocity.

Comparison between additive manufacturing and traditional manufacturing techniques

The additive manufacturing technique can be compared to the traditional (subtractive) manufacturing techniques rely on the removal of material through cutting, milling and drilling (www.renishaw.com) resulting in:

- High levels of wasted material.

- Long product lead times.

- The requirement for tooling and fixtures.

- Complex, multi stage processes.

- Component complexity is limited by process tooling paths.

Whilst additive manufacturing has great potential it is still a relatively new technology and there are key areas for improvement and consideration when adopting the technology (www.renishaw.com). The main limitation and advantages of the additive manufacturing technology (including the laser melting process) are:

- Surface finish and accuracy: component anisotropy can become an issue dependent on layer thickness and orientation of a surface, which can result in 'stair stepping' (i.e. ridges appearing in the final component as a result of the layer building process).Whilst part finish is improving it is still not comparable to that of subtractive systems.

- Process speed: building layer by layer can be a time consuming process, particularly for larger component manufacture.

- Size of components: it can be produced are limited to machine chamber size.
- Skills shortage: A completely new design process must be considered when (re)designing a component for additive manufacture. Aspects such as structural integrity, material properties, part orientation and component weight must be fully understood to ensure the process is effective. The technology and its advantages and limitations must be widely understood for additive manufacturing machines to be used for industrial applications on a widespread basis.

- Software: the software used by additive manufacturing machines can seem complex, and it will need further development as the manufacturing process advances. A lot of existing CAD software is designed for more traditional manufacturing techniques, and interfaces can be unintuitive and hard to use, particularly for non-experts.

- Expense: as with other new technologies, additive manufacturing machines can represent a sizable capital investment, which may be prohibitive.

- Standardization: there is a requirement for international standards and practices for additive manufacturing which will enable performance measurement, monitoring and assurances. Standard practices will also facilitate partnerships between users and system manufacturers and help the technology and usage to continue to develop.

On the contrary, this new technology offers different advantages that allows to change the approach in the design phase redefining the feasibility concept, overcoming the main limitation of the conventional machining techniques, in particular they are:
- Minimal wasted material.

- Consolidated assemblies of parts.

- The ability to create previously unachievable complex shapes and geometries such as internal pathways, voids and structures.

- Designers can easily create completely bespoke / customized models and objects.

- Topological optimization: reduce weight by optimizing part geometry based on design loads.

- Complex parts that previously would have been manufactured separately and joined together due to geometric restrictions, can now be made as a single piece.

Through the utilization of additive manufacturing it is possible to optimize the design of components and objects, so as to optimize design and weight (see Fig.3): one way of achieving this is topological optimization (www.renishaw.com). Topological optimization software is the term given to programs that are used to determine the 'logical place' for material. Material is removed from areas of low stress until a design optimized for load bearing has evolved. The resulting model represents a component that is both light and strong, but can look unconventional.

Fig.3: Mountain bike was developed by Renishaw and Empire Cycles using additive manufacturing, and topologic optimization (www.renishaw.com).

In this contest the present work of thesis has been performed in order to investigate the effect of the main process parameters (laser power, interaction time and plate temperature) in the selective laser beam melting process, performed on AlSi10Mg powder.

In the first chapter of the thesis, state of art about the selective laser beam melting process is reported and analyzed. In details, a description regarding the application of the laser additive technique applied on Aluminum alloys is reported.

In the second chapter, objectives of the present thesis are presented, highlighting innovative aspects of this research.

In the third chapter, the experimental procedures are reported; materials equipments used in this work as well as characterization methodologies are introduced. The production of the samples via selective laser beam melting were performed in Renishaw S.p.a in Torino while the characterizations of the results were done in the laboratory of CNR-ICMATE (ex IENI) in Lecco.

In the fourth chapter, the results obtained on AlSi10Mg alloy are presented. The study of the mechanical and metallurgical modifications imposed by the laser melting process were investigated in function of the process parameters investigated. Some comparison with a conventionally prepared Al alloy are also taken into account for defining the main peculiarities of the additive manufacturing process.

Finally, the main conclusions regarding the results obtained and reported and discussed. The future developments, linked to the next activities regarding this work, are listed, too.

Chapter 1

State Of Art

1.1) The Laser Melting process

The selective laser beam melting process is an additive manufacturing technique that allows to fabricate metallic parts having high mechanical properties and complex geometries difficult or even impossible to produce via conventional process machining. The laser melting techniques make possible to change the rule of the engineering design giving the possibility to concept the component focusing only on the functionality without considering the technological feasibility. For example, it is possible to create cooling channels with complex geometries in the inner part of the components which work at high temperatures, allowing better performances and optimizing the cooling. Other advantages offered by the laser melting technique is the substantial reduction of the production phase, consequently it reduces the entire production time of the manufacture cycle. These aspects are very important in all that fields in which the components are produced in a limited amount and their design is continuously changed as happens in the biomedical field and in the racing world, in which the possibility to bring an adjustment immediately testing the efficiency of the modification could be a remarkable advantage.

However, the main limitation of the laser melting process is the long production time with respect the conventional manufacturing technique, because currently this technology does not give the possibility to fabricate big quantities per time unit. This drawback can be overcome considering the possibility gives by the laser melting process to produce reticular structures having fine mesh and, where it is possible, substituting the fullness with this type of structures able to keep the same mechanical properties, if the fabrication is anticipated by an appropriate design phase. This allows process cost lowering, both for the reduction of the production time and of the material consumption.

Fig.1.1: Example of reticular structure realized via laser melting technique. This type of structure guarantees the lightness satisfying the mechanical properties of the component (www.renishaw.com).

The main challenges of the laser melting technique include the surface roughness and the part accuracy or layered residual stresses, which are reinforced by the thermal gradients due to full melting and solidification in a very short time (E. Yasa, 2011). Some density test demonstrate that it is possible to produce full dense objects (98-99%) with residual porosity due to various reason such as the evaporation of elements with a high vapor pressure, trapped gas, bad surface quality, reduction in the solubility of the dissolved elements in the molten pool during cooling and solidification. Some mechanical properties, such as fatigue and toughness, are strongly dependent on remaining porosity as well as the microstructures after selective laser fusion process in which high cooling rates occur.

The powder particle around the molten pool are involved in the melting process causing the enlargement of the molten pool; this phenomenon is known as the bobble effect which is responsible to the formation of the elevated edges that worsen the flatness and the geometry of the laser melting parts top surfaces. The limitation of the bad surface quality can be enhanced by employing different surface modification technologies including mechanical, chemical and thermal processes. Laser re-melting may improve the surface quality allowing the improvement of the mechanical properties, without need for additional production equipment and without any removal of the part from the building platform avoiding fixation errors.

The residual porosity in laser melting parts may be detrimental for some mechanical properties, such as wear performance, toughness or ductility. By the laser re-melting technique is possible to increase the density as high as possible until the required level.

For density improvement, every layer can be scanned twice using different laser re-melting parameters such as scan spacing, scan speed, number of re-melting scans or laser power. Higher re-melting scan speeds in combination with low laser power, resulted in higher density (E. Yasa, 2011). About the scan spacing should be low enough to ensure good connection between scan tracks.

Considering the distortions, the residual stresses and the porosity, in order to minimize theme the powder in the build platform can be maintained at an elevated temperature (below the melting point of the powder).

The most common solutions include:

- Infrared heaters, placed on the building platform to maintain high temperature around the part that is processed;
- A pre-heating of the powder prior to spreading over the build area;
- Resistive heaters, around the building platform.

This solutions offer also the possibility to minimize the laser power requirements of the process, at the same time, to improve the absorption of the laser beam and prevent the deformation of the part during the build due to thermal distortions and to reduce the temperature gradients. But using the pre-heat technique, it must consider that a cooling period is required, in order to avoid a possible powder degradation due to a premature exposure to the external atmosphere in which is present oxygen and the powder cannot be recovered and used for further processes. If necessary, at the end of the process further finishing operations are performed.

1.1.1) The process equipment

The laser fusion technology is composed by a laser system, a set of optical laser beam focusing, a powder feeding system (loader and roller or coater) and a control center (Sabina L. Campanelli) (see Fig.1.2). The laser melting process is based on a principle in such manner that the powder is applied in very thin layers on a building platform and melted due to the thermal energy induced by a laser beam. The part is built by melting and re-solidification of the powder particles, before the building platform is lowered and coated with a new layer of powder. In order to achieve this result, a coating device with a silicon wiper applies the new layer of powder onto the previous layer. The laser beam is being redirected across the surface of the powder bed (identified as the *x-y*-plane) by scanner optics (pivoted mirrors) in such a way that the powder particles can be selectively melted where desired (Rehme, 2009).
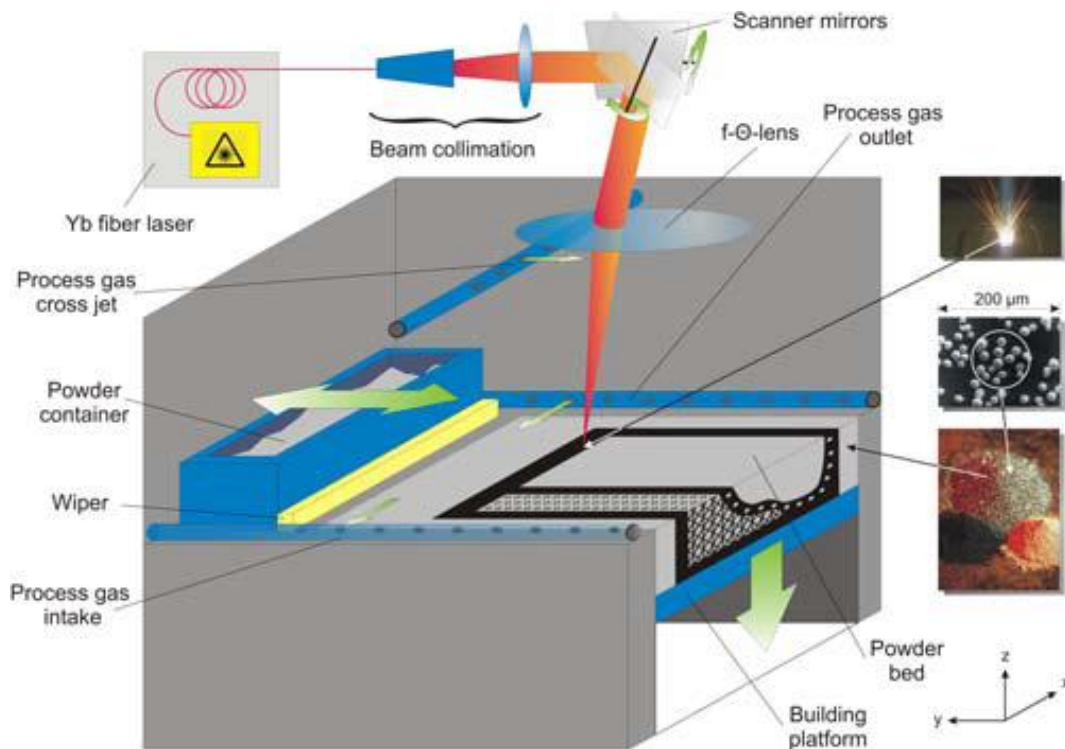
Fig.1.2: Cross section machined by laser melting technique (Rehme, 2009).

As said previously, the piece to be achieved should be drawn using a three dimensional solid or surface modeler, and hence the process start from the development of the mathematical model in a CAD format compatible with the management software of the rapid prototyping machine. The currently accepted graphic standard by all manufactures is the STL (solid to layer), introduced by 3D Systems.

The STL file is then processed for the orientation phase, that allows to select the best growth direction of the piece and consequently it influences the dimensional accuracy and production time, and the slicing step, instead, that is critical because it determines the accuracy of the product. The object is divided into a certain number of slices, with orthogonal planes to the direction of growth, obtaining the thickness layers and a profile of each section, which describe the trajectory of the scanning laser beam.

The laser melting technology uses as starting material the metallic powder, which is deposited on the build plate with a uniform layer thickness equal to that of the sections in which the 3D object file has been divided. The laser machine software, reading the 3D model, produces one by one each layer on x-y plane consolidating the metallic powder through its fusion via laser beam that draws the geometries of the single layer above the powder bed. The optical system is composed by emitter fiber laser, a collimator, a rotating mirror system able to reflect and direct the laser beam in the x-y plane and a F-Theta lens, having the function to focalize the laser in the exact point on the powder bed. Due to the fact that the spot diameter is almost 100 μm and the positional accuracy in the order of tens of micron, the machine is able to reproduce the part geometry with very high precision.

When the layer scanning is terminated, the build plate, which is placed on a mobile elevator, is lowered along the z-axis of a quantity equal to the thickness layer of the section into which the 3D model has been decomposed. At this point, a new layer of powder is deposited over the previous processed one, and the laser will proceed with the powder bed melting and the partial re-melting of the one below. In this way it is possible to create a continue structure. The process is repeated until the completion of the part.

During the growth, the object is supported by the powder bed that has not be processed and by the supports that are structures build by the laser during the process. These supports are built considering that the final removal process of the part from the build plate need to be easy but at the same time they have to securely sustain the components during the machining. The supports play also the fundamental role to allow a correct heath distribution of that zones that do not directly lie on the substrate, but they are placed on the powder bed. The powder has a lower thermal diffusion with respect the melted and consolidated material, and they do not allow an adequate heath distribution from the areas near to the molten pool. When the entire process is completed, the build plate comes to

the initial plane and it is possible to remove the component from the not processed powder. The unused powder is collected in a special tank and subsequently filtered by a mechanical sieving system. By this way the powder becomes free from impurities and can be used again for the next jobs.
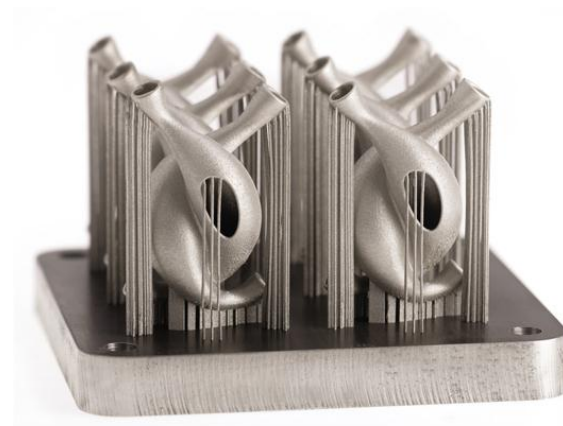
Fig.1.3: Example of support made by laser melting technique (www.renishaw.com).

Being the molten pool very little, the specific surface is big and this factor, joint with the factor that often the processed materials such as Aluminum an Titanium are analogous with the oxigen, becomes important to preserve the material from the risk of oxidation and, for this reason, the process takes place inside a closed chamber, filled with argon, with an oxygen amount lower than 2000 ppm (0.2%). The argon inside the chamber is steadily recirculated by a gas pump, in this way, it is prevented both the material oxidation and the particulate removal developed during the process. The captured particles from the gas stream are retained by a filter installed before the entrance of the pump.

1.1.2) The powders characteristic

The laser melting process is based on the component production through the consolidation of different layers of metallic powder progressively overlapped between each other. For this reason the powder characteristics influence the entire process result. The morphology and the powder size influence the fluidity of the powders and so on the easiness with which they are spread on the build plate in uniform way. The uniformity of the thickness layer is an important aspect: each area with a higher thickness layer could lie the reduction of the re-melting deepness, weakening the bond with the substrate reducing the global quality of the component. Should also be considered that, since the smaller particles exhibiting in equal volume greater surface area, working with powder beds having fine particles result in more absorption of laser energy, a higher temperature of the melted powders and a greater kinetic in the coalescence process. Together with the powder size, also the powder geometry influence the process, in fact, powders having irregular geometries spread with preferential orientation, causing anisotropy during the cooling. Furthermore, using powders with different geometries the risk to have zone with low particles concentration will be higher, and these zones tend to consolidate more rapidly compared to the others, increasing the risk of porosity and of residual tensions inside the component (Yadroitsev *et al*., 2012). For these reasons in the laser melting process, the use of spherical powders is recommended. The powder produced via gas atomization are preferred to those that are water-atomized, which are more irregular.
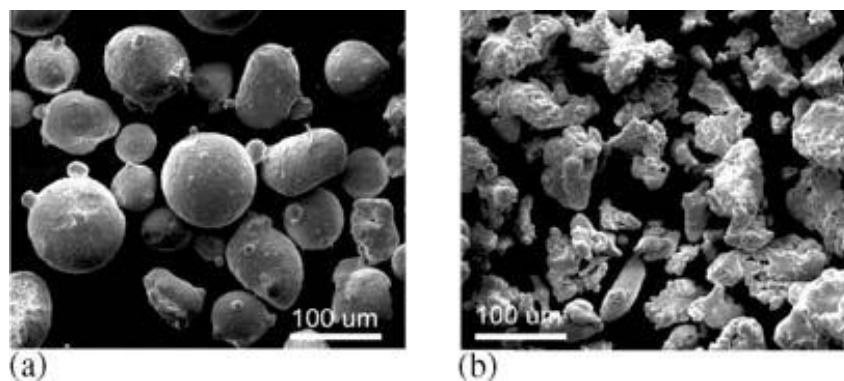
Fig.1.4: SEM images of (a) gas-atomized and (b) water-atomized H13 tool steel powder (Pinkerton e Li, 2005).

It is crucial to maintain the unused powder in a cool, dry place; due to the fine particle size they may in fact retain high moisture contents which may affect their rheological properties, reducing their ability to flow through the narrow passages and to be uniformly distributed on the build plate. Any excesses of residual moisture can be eliminated by

subjecting the powder to a heat treatment prior to its use. The temperature of the treatment should be sufficient to evaporate the excess moisture but not such as to trigger phenomena (phase changes, recrystallization, sintering, melting, etc..) Such as to alter the physical properties of the powder. For most of the cases are recommended soaking treatments at temperatures of between 110 ° C and 180 ° C for 12 hours; it is advisable to consult the specifications of the powder in question.

In a first time, high strength powder mixtures were used for the DMLS process (Direct Metal Laser Sintering). These mixtures contained two type of metal powders, such as Fe-Cu, WC-Co, TiC-Ni/Co/Mo, TiCN-Ni, TiB_2-Cu and Fe_3C-Fe. The process aimed to melts only the powder having the lower melting point. After, it has spread the use of commercial alloy such as titanium in powder bed laser melting process, due to its high mechanical properties combined with its very low weight. Abe (Abe F., 2001) has studied the behavior of nickel base alloys and has reported that the process does not exhibit balling phenomenon but only part deflections and cracking.

It must be considered that the process parameters for a given material are optimized to a specific type of powder and can not guarantee the same results when applied to a powder with the same chemical composition but with different particle size and morphological characteristics. For this reason, the manufacturers of laser melting machines should provide to the clients, not only the optimal parameters for processing a given material, but also the same type of powders for which such parameters have been developed.

1.1.3) The laser melting application fields

The fields of application of the laser melting technology are different, thanks to the high flexibility of the process and the possibility to generate parts with a complex geometry and different sizes. In this chapter are illustrated some examples of application fields of this technology, which are different (www.renishaw.com):

- Automotive: passenger, commercial, motorsport.

- Aeronautical: civil aerospace, space.

- Consumer: fashion, jewelry, lighting, furniture, entertainment, art.

- Medical: customization of implants, bone, teeth, hearing aids, surgical guides.

- Power and communications: sonar body, housing, fuel cells.

- Production and manufacture.

Below, different image representing the application fields of this type of technology. In Fig.1.5 it is possible to see the selective laser fusion process reliability, passing from the CAD model to the final product.
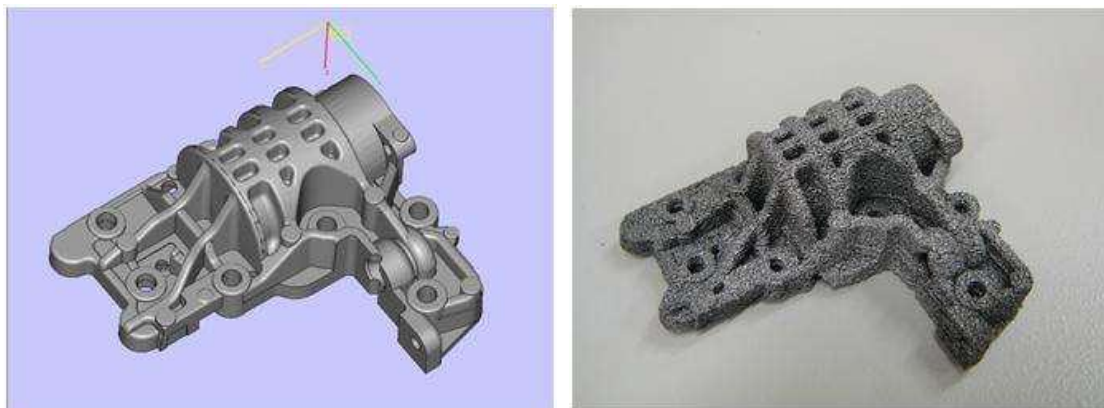
Fig.1.5: An aluminum alloy prototype of automatic transmission part, passing from the 3D CAD model to the final product (Hideki KYOGOKU, 2010).

The Fig.1.6 illustrates an example in which AM is a key enabler for the design and topology optimization. This includes the design for light-weight structuring with a weight reduction by typically up to 50% e.g. in the case of automotive power turbine components as well as the "design for performance" rather than "design for manufacturing".
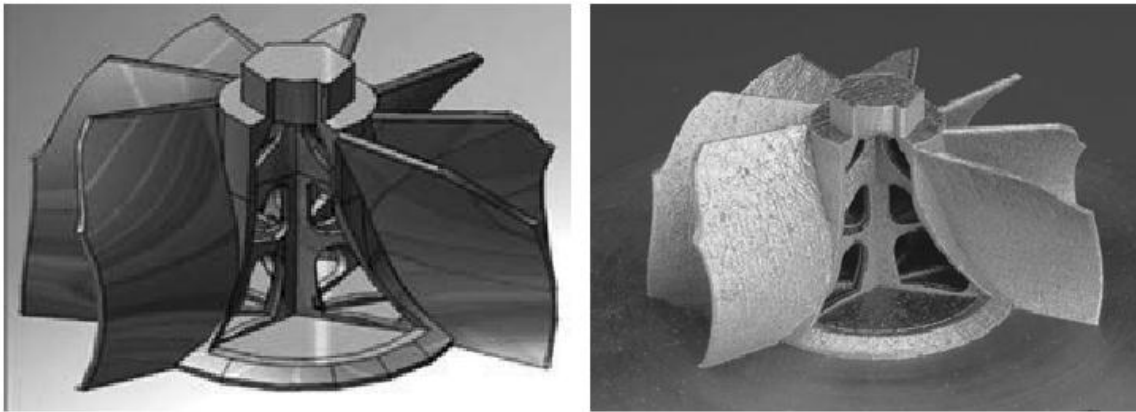
Fig.1.6: CAD image of a part created with an internal structure designed to reduce weight (left), component made out of IN718 by means of AM with a weight saving internal structure (right), (Buchbinder, D., 2011).

Fig.1.7 depicts the CAD picture of the selected part. It is a mold insert for plastic injection molding. To increase the productivity of the manufacturing process, spiral-cooling channels were designed inside the mold and incorporated in the CAD data.
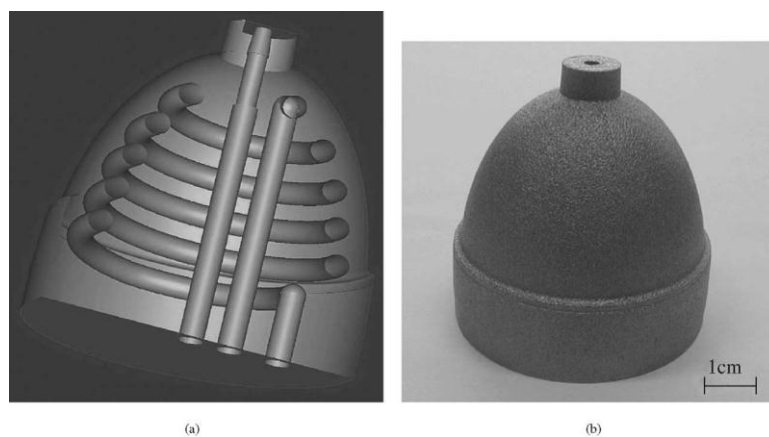
Fig.1.7: The CAD picture (a) and the laser-sintered part (b) made from LaserTool, (A. Simchi, 2003).

In Fig.1.8 a sample acetabular prosthesis manufactured by selective laser fusion. The cup has a complex, fine-scaled scaffold structure on its outer surface, which is aimed at improving osseointegration.
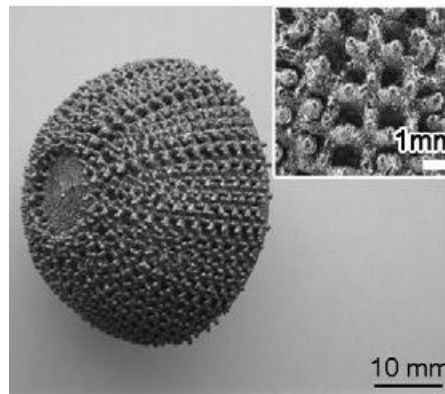
Fig.1.8 Example of precise acetabular cup in Ti–24Nb–4Zr–8Sn alloy produced by SLM, (L.C. Zhang, 2011).

In Fig.1.9, on the left it is represented an example of a wide range of biomedical prosthesis with a great variety of geometric shape, while on the right it is illustrated a complex example of the great quality, fidelity of shapes in maxilofacial implantolgy, (Drd. Ing. Ciobota Nastase-Dan1, 2009).

Fig.1.9: Example of prosthesis production via selective laser fusion (on the left) and maxilofacial implantolgy (on the right).

1.2) Aluminum alloys

The aluminum is one of the most spread element in the world. In nature, it is present combined with other elements (www.ing.unitn.it). The main properties of the Aluminum are:

- Low specific weight; it is almost one third of that of the steel and copper alloy;
- High corrosion resistance;
- High thermal and electrical conductivity;
- Atoxicity;
- High plasticity and ductility;
- Low power radiation;
- High weldability;

In order to improve the mechanical properties of this metal, which is principally soft and ductile, it is combined with other elements, and its characteristics radically change. As concern the aluminum alloy, the common peculiarity are:

- Low melting temperature between 510 and 650 °C
- Low specific weight, between 2,66 and 2,85 gr/cm^3
- Very high thermal and electrical conductivity

Each alloy element has its own effect on the aluminum:

- The Silicon improves the castability and it reduces the expansion coefficient
- The Magnesium increases the corrosion resistance
- The Manganese increases the mechanical and corrosion resistance
- The Copper increases the mechanical resistance, specially the hot mechanical properties
- The Zinc, primarily when it is associated to the Mg, increases the mechanical resistance

Tab.1.1 International classification used a four digit system, whose first is the primarily alloying element, the letter following the name indicates the alloy treatment.

1xxx	Al with minimum purity 99,00%
2xxx	Al-Cu alloys
3xxx	Al-Mn alloys
4xxx	Al-Si alloys
5xxx	Al-Mg alloys
6xxx	Al-Mg-Si alloys
7xxx	Al-Zn alloys
8xxx	Al with other alloying elements
9xxx	experimental series

1.2.1) The AlSi10Mg in laser melting processes

The aluminum alloy used in my thesis is AlSi10Mg. This is a widely used alloy for aluminum castings. The hypoeutectic alloy is near the eutectic composition (12.5% Si) which is responsible for the excellent casting properties. Fig.1.10 shows the phase diagram of Al–Si. Minor additions of magnesium (0.3–0.5% are most beneficial) allow hardenability by natural or artificial ageing (E. Brandl, 2012).
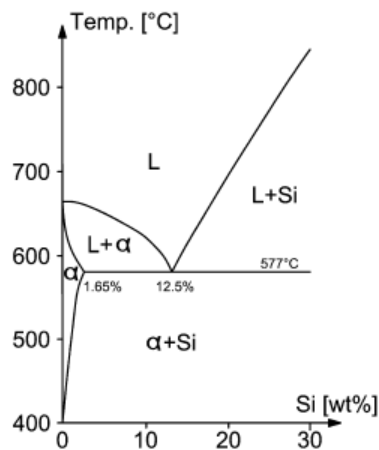
Fig.1.10: Phase diagram of Aluminium–Silicon Erhard (E. Brandl, 2012).

Tab.1.2 shows the chemical composition of the AlSi10Mg alloy used. The compositions of all batches measured were within this specification.

Tab.1.2 Chemical composition of the alloy AlSi10Mg (E. Brandl, 2012).

Al	Si	Fe	Cu	Mn	Mg	Zn	Ti
Balance	9.0-11	0.3	0.03	0.001-0.4	0.2-0.5	0.1	0.15

According to the phase diagram, the microstructure (Fig.1.11) is characterized by the size and arrangement of the:

- α-Al matrix (bright phase),

- eutectic Si-particles (dark phase).
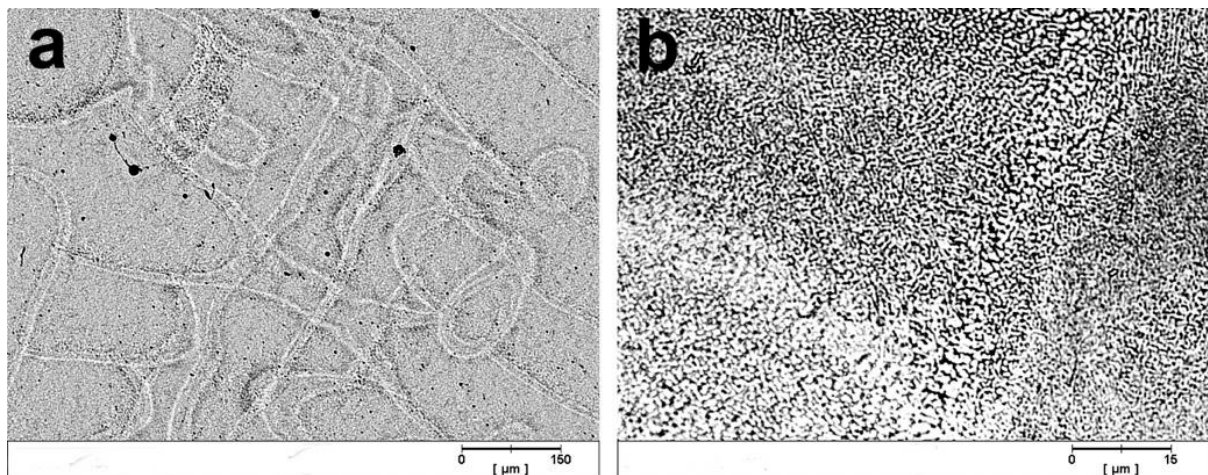
Fig.1.11: Typical microstructure of AlSi10Mg before peak-hardening (build platform temperature = 30°C/as-built); plane is perpendicular to the longitudinal axis of the sample; (a) macro view, and (b) micro view (E. Brandl, 2012).
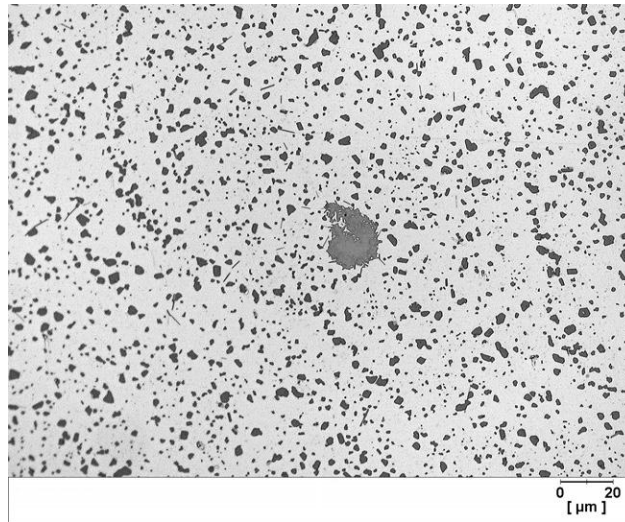
Fig.1.12: Typical microstructure of batch (build platform temperature=30°C/Peak-hardened); plane is perpendicular to the longitudinal axis of the sample (E. Brandl, 2012).

However, the aluminum powders is a material that is not widely used in powder bed laser melting process. Different researchers, among which E. Louvis *et al.* (2011), investigated the laser melting processing of AlSi10Mg. They discovered that it is possible to produce parts of near 100% relative density by using a laser power higher than 150W and a laser beam diameter of 200 μm.

There are a number of difficulties in the laser melting processing of aluminum powders. Firstly, laser melting critically depends on being able to spread a thin powder layer, which is difficult because aluminum powders are light with poor flowability, especially in the presence of moisture. Consequently, aluminum alloy powders are unsuitable for many existing powder deposition mechanisms, even though they are effective for other metal powders of the same particle shape and size distribution. Secondly, although the laser melting technology uses shorter wavelength radiation than laser sintering process (1.06 μm compared to 10.6 μm of CO_2 lasers) which favours its absorption by metals (Steen, 2003), the high reflectivity of aluminum (91%) increases the laser power required for melting. This effect becomes more significant with increased beam overlap as although the metal as a powder bed has a high absorptivity (multiple reflections and absorptions within the particle bed modelled by Gusarov and Kruth (2005), any neighbouring overlapping solidified hatch is highly reflective.

Another reason why higher laser powers are required is the high thermal conductivity of aluminum (compared to other materials used in laser melting process such as stainless steel and titanium), which leads to the rapid dissipation of heat away from the scanned track. This phenomenon is most significant during the first layer of the build, which is on

the solid aluminum substrate, according to Fischer et al. (2002) who showed that the heat conductivity of powder layers is lower than that of dense materials. The high thermal conductivity also determine the width of the single track of aluminum alloy, which is fairly narrow compared to that of other metals such as alloy steels and is close to the laser spot diameter (Hideki KYOGOKU, 2010).

Nevertheless, the main obstacle to the effective sintering and melt processing of aluminum alloys is oxidation. The thermodynamic stability of aluminum sesquioxide, (see note 1) makes difficult the removal of the oxide film present on the surface of the metal powder.

The origin of the oxide could be via alloying addition into the metal powder or air/gas entrapment via turbulent flow during laser melting process (Campbell J, 1991). For example the Mg additions promotes the formation of spinel ($MgAl_2O_4$) in thin layers and Si, the formation of mullite ($Al_2O_3SiO_2$, which is rare silicate), (Dunkley JJ.1998).

In Fig.1.13 it is possible to observe the oxide formation inside an aluminum laser melting part.
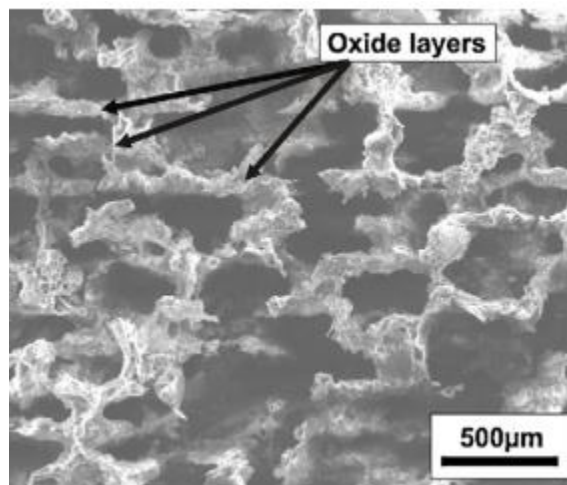
Fig.1.13: SEM Micrographs of a 6061 sample section produced by using the laser melting technique (Eleftherios Louvis, 2011).

During the laser melting processing, the overall gas oxygen inside the chamber of the laser melting machines is almost 0.1–0.2%. This is low enough to allow the processing of stainless steel and titanium, probably because the oxides formed are either easier to break up and so enter the melt pool or because they are vaporized during heating by the laser . However, the effect of the oxygen still present in the chamber on the aluminum specimens (Eleftherios Louvis, 2011) can be seen on their top surfaces which are

discoloured compared to the other surfaces. The oxidation phenomenon occurs not only on the top surface of the aluminum part but also on each of the scanned layers during the process. In the same research Eleftherios Louvis discovered that oxide layer was formed not only between two different powder bed layers but also among two different scanned tracks on *x-y* plane. It appears therefore that although bonding was occurring between the layers with the oxides breaking up this was not true between tracks. The quality of aluminum or aluminum alloy parts produced by laser melting is controlled by the formation of oxide films in a similar way to conventional casting and that an understanding of the behavior of these films and how to disrupt them is essential to improving the parts. Although the constant reaction between the alloy and the atmosphere as the material is processed will reduce the oxygen content of the gas by forming oxides, even at very low oxygen concentrations oxide films will form. These oxide films have a number of effects including the passivation of the surface of the molten metal, reducing its reactivity and increasing the difficulty of penetrating the surface, while actually lowering the surface tension. The creation of a part by the laser melting technique can be considered as the movement of a melt pool across a surface by the addition of powder at the front of the pool and the freezing of material at the back. If the component produced is to be 100% dense it is important that the underlying and surrounding solid partially re-melts so that the regions wet and fuse with the melt pool. However, with aluminum and its alloys this description is incomplete as there is an adherent solid oxide layer formed both on the underlying solid and on the melt pool, and even when sufficient heat is applied to partially re-melt the underlying metal there are still two thin oxide films separating the regions of molten metal. Therefore the wetting and fusing of the aluminum regions is controlled by the disruption or disassociation of these oxides, not by the melting of the different regions.

Marangoni forces that stir the melt pool are the most likely mechanism by which these other oxide films are disrupted and with these experiments the melt pool seems to disrupt the lower oxide films but not the sides, creating the 'walls' of oxides (see Fig.1.14).
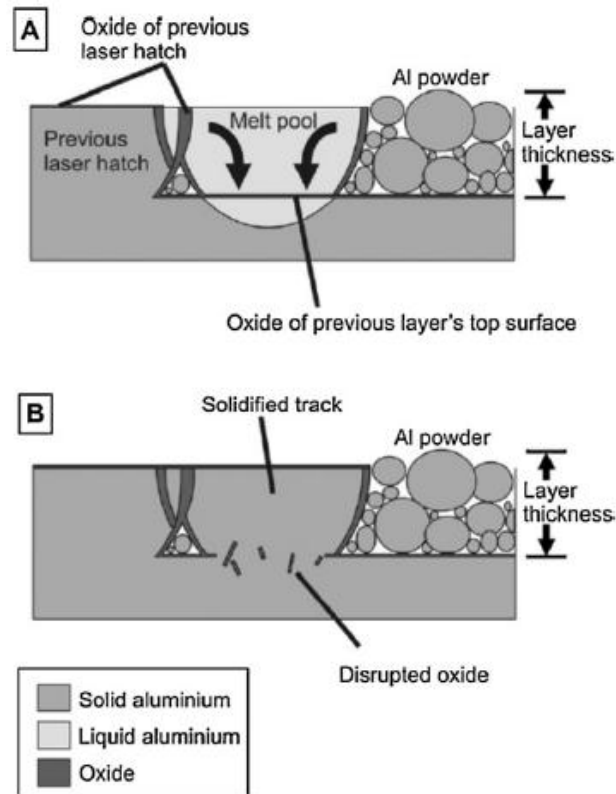
Fig.1.14: (A) Marangoni convection in the molten pool. (B) Oxide disruption and solidification of the molten pool.

As concern the oxidation problem, the atmosphere plays a fundamental role in the laser melting process, that is the reason why it must be controlled in order to prevent undesired reactions. As concern the atmosphere effect, the role of the argon, nitrogen and helium was investigated on the densification process of the aluminum alloy (Wang XJ, 2014), and the results have shown that no significant effect occurred on the densification process of the melted powder. These outcomes are in contrast with that provided by other experiments (Asgharzadeh H, 2005), (Simchi A, 2003), in which the laser sintered of metal powder under argon atmospheres yielded better densification in comparison to nitrogen atmospheres, especially at high scan rates. These contradictions are due to a different chemical nature during the reactions occurring in the laser melting process.

1.2.2) Adduction of the alloying elements to the aluminum powder.

Laser induced in-situ chemical reactions have also been employed to fabricate Al/Fe$_2$O$_3$ and Al/TiO$_2$/B$_4$C metal matrix composites (MMCs) (Dadbakhsh, 2012), (Ghosh SK, 2014). In this process the laser thermal energy is able to overcome the activation energy of the reactants thereby yielding adequate thermal energy to form chemical compounds. This technique gives rise to a fine and uniform distribution of compounds, improving the consolidation and the release of exothermic energy that promotes the laser melting response of the reactants. The occurrence of balling inhibits the inter-particulate melting as a consequence of the presence of oxide film on the surface of powder particles which prevent the wettability of the liquid metal with its solid form due to the initiation of Marangoni convection (Kruth J-P, 2007), (Kruth J-P, 2005). Another obstruction to the laser melting process is the occurrence of part distortion due to high temperature gradients.

The alloying elements, magnesium and silicon, to the aluminum powders have no predominant effect on the processing map boundaries but they have a significant effect on the nature of the evolved surface morphology during laser melting/sintering processes of aluminum powders. The Fe_2O_3 adduction to the pure aluminum powders used in the laser melting process caused an *in-situ* reaction between Al and Fe_2O_3 powder releasing extra heat and extra energy promoting the formation of a molten pool and improving the laser melting processability over a wide range of parameter (Dadbakhsh S., 2012). The released energy is proportional to the Fe_2O_3 content and it makes possible the control of the surface quality and roughness. The increasing content of Fe_2O_3 has a negative effect on density but a positive effect on hardness that increases significantly thanks to the superior microstructural features of a particle reinforced matrix. The adduction of Fe_2O_3 powder determines the expansion of the processing windows and it stabilizes the laser melting processing of pure aluminum powders to scanning rates higher than 500 m/s, allowing the increase of the production rate and the reduction of the energy consumption during the laser melting process.

The adduction of alloying elements causes the variation of the absorption coefficient changing the morphology of the scanned track (Hideki KYOGOKU, 2010). The outcomes of an experiment in which a Al-12Si powder was used have shown that in the case of the addition of laser absorption material the melting mechanism during the laser melting process can be enhanced. By adding the absorption material, the scanned track pass from the partially melted track in case of low amount of absorption material, to the melted and balled continuous track and smoothly continuous tracks in case of high amount of it.

1.2.3) Loss of alloying elements

High temperature during the powder bed laser melting process, when high power density is employed could lead the selective vaporization of alloying elements whose melting point is lower of that of base alloy, in this case aluminum (E.O. Olakanmi, 2015). The vaporization of alloying elements starts some mechanisms of transportation of vaporization elements from the bulk to the surface of the molten pool, of vaporization of elements at the liquid/vapor interface and mechanisms of transportation of the vaporized species into the surrounding gas phases. The losses of alloying elements following the vaporization process, may induce to a reduction of the mechanical properties, for example: the reduction of Mg content in aluminum alloy due to vaporization process may result in the loss of precipitation strengthening, causing the reduction in yield strength, hardness (Zhao H, 2001) and corrosion resistance. The reduction of alloying elements end hence the instauration of vaporization mechanisms could lead to an instability of the process and consequently to a high level of porosity. This is why is fundamental to control the temperature in the molten pool during the laser melting process and hence the correlated energy density by adjusting the parameters. The vaporization rate increases with the dissipated energy density. Combining medium or high power with high scanning rates is critical to avoid vaporization (Collur MM, 1987).

1.3) The laser melting process parameters and their effects on material properties.

In order to overcome the main difficult challenges concerning the surface quality, the porosity and the residual stress inside the part, it is required a careful study of the main process parameter in order to have the process control and achieve the product requirements.

The physical phenomena involved in laser melting process when the laser beam hits the powder bed include the absorption and the scattering of the radiation, the thermal diffusion, the phase transformation, the interface migration from solid phase to the liquid phase, the fluid flux due to the surface tension and to the mass transport in the molten pool (Yadroitsev, 2010). For this reason it is difficult to describe what happens during the process with a mathematical model and the used approach when searching for optimal settings to process a new material is purely empirical, i.e. based on the production of test components and the subsequent evaluation of their quality. Metallic powders have a higher degree of contamination by moisture, organics, absorbed gases, oxide nitrides films on particle surfaces (Das S., 2003). These contaminants determine the inhibition of the wetting, which promotes the interlayer bonding and the densification of the melted powder, but also the reduction of the mechanical properties and the worsening of the part geometry of the consolidated component during the powder bed laser melting.

These parameters should be optimized individually for each material with which it works, in order to minimize the porosity and obtain a good cohesion between the different layers. These parameters usually include:

- Laser Power (LP): is the power of the laser beam that scans and melts the metal powder: increasing the power of the laser can increase the depth of penetration of the melt and allowing an increase in the scanning speed ensuring the same transfer of energy to the material;

- Hatch Distance (HD): is the distance between two adjacent scanning tracks of the laser: increasing it, the production speed is increased but it is reduced the portion of the re-melted material, increasing the possibility of encountering residual porosity;

- Scan Speed (SS): is the speed with which the laser beam moves over the bed of powder by melting the scan tracks, is a parameter which strongly influences the speed of the process but also its quality.

In the market there are some laser melting machines, for example the Renishaw AM250, that work differently from those of conventional plants. they do not perform continuous melting traces, but rather they consist of series of equally spaced points, on each of which

the laser beam interacts with the powder for a specific time. When working with these machines, the scanning speed is not one of the parameters on which you can intervene to optimize the melting process, rather it is decomposed in two other parameters:

- Exposure Time (ET): it is the laser-powder interaction time, if excessive can cause the evaporation of metallic particulate, if too small can cause an partial (but not entire) melting of the material;

- Point Distance (PD): is the distance between the equally-spaced points which constitute each scanning track: as in the case of the Hatch Distance, the increase of this distance will increase the production speed will decrease and a portion of the re-melted material.

In Fig.1.15 you have a representation of some of the above parameters.
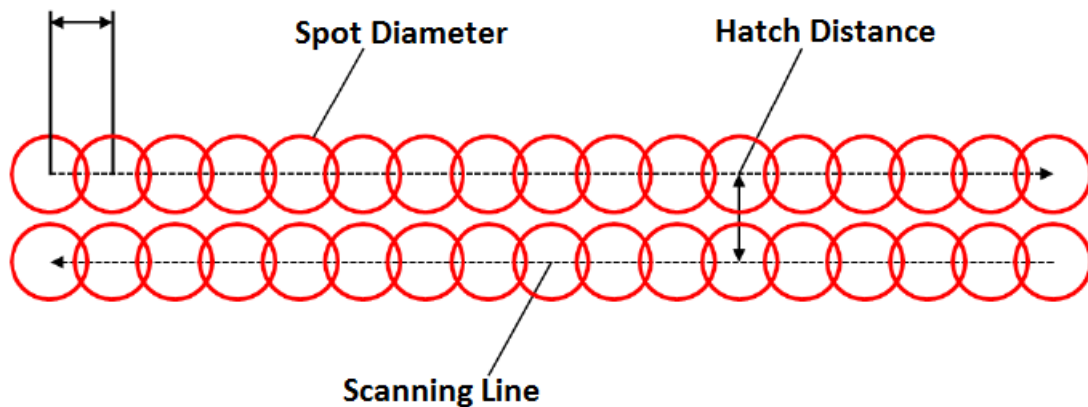
Fig.1.15: Example of some of the main process parameters in the laser melting process.

In Tab.1.3 a summary of the main process parameters determining the surface quality of the fabricated part and the characteristics of the powder material affected by the process.

Tab.1.3: process parameters and material variables influencing the process and the densification mechanism of fabricated part (E.O. Olakanmi, 2015).

SLM processing parameters	Material properties
Laser power	Viscosity
Scan rates	Surface tension
Atmospheric control	Particle size and distribution
Gas flow	Particle shape
Heaters (Bed temperature)	Absorptivity/reflectivity
Laser Type	Thermal conductivity
Scan radius	Specific heat
Scan vector length	Emissivity
Scan spacing	Melting temperature
Thickness of layers	Component ratio
Machine (specific type)	Chemical composition

The laser power, scan speed, and the interaction between the scan speed and the scan spacing have major influence on the porosity development in the laser melting processed AlSi10Mg alloy builds (Read N., 2015). The main laser melting parameters have to ensure the process stability and the reproducibility reducing the resource consumption. It is an established fact that high temperature developed during the process leads to a low contact angle and viscosity and high Marangoni flow thus improving the densification (German RM., 1985). The Marangoni flow can be describe as the initiation of thermocapillary forces for fluid flow as a consequence of the temperature gradient in the molten pool which gives rise to a corresponding differential surface tension between the edge and the center of the molten pool (E.O. Olakanmi, 2015).
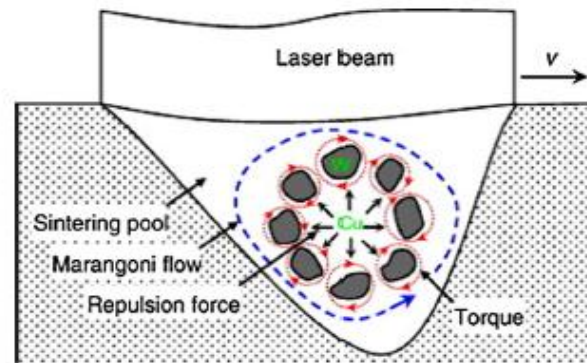
Fig.1.16: Schematic illustration of Marangoni flow as applied to the direct SLS of W–Cu 2-phase direct SLS.

1.3.1) The energy density

Laser power density is the most influencing process parameter in laser melting process. Studies on laser sintering/ melting of powder report that preheating powder and substrate can reduce requirements to laser power, improve radiation absorptivity of the powder and wettability of the substrate. Theoretically, the effect of preheating can be roughly estimated from the expression

$$Q = \rho c_p (T_m - T_0) + L_f$$

where Q is the energy necessary to melt a unit volume of material, ρ is the density of bulk material, c_p is the specific heat, Tm is the melting point, T_0 is the initial temperature, and L_f is the latent heat of fusion. For example, energy required for melting of a certain volume of stainless steel grade 316L (ρ_{bulk}= 7800 kg/m3, c_p = 515 J/kg K, T_m = 1673 K, L_f = 275 kJ/K) preheated to 900 °C (1173 K) is 43% less than for the same material at 80 °C. In additive manufacturing, traditionally used preheating systems are infrared heaters or resistive

heaters placed near/around the building platform to maintain high temperature around the workpiece or feed cartridges to preheat the powder before spreading over the build area (I. Yadroitsev, 2013). The energy input strongly influences the response of a powder–substrate system and therefore has to be carefully controlled for laser melting part quality. The volume of powder involved in laser melting track formation is determined basically by laser power, laser beam diameter (spot size), time of laser irradiation (scanning speed), powder layer thickness, and physical properties of the powder and substrate materials (absorptivity, thermal conductivity, surface tension, viscosity, etc.). At a high laser energy input (low-speed scanning), a large volume of powder is involved in the track formation;

capillary and thermo-capillary flows (Marangoni effect) can significantly affect the shape of the track and its continuity. On the other hand, with increase in laser scanning speed, width-to-length ratio of the molten pool decreases, and the molten pool becomes narrower. Application of higher scanning speeds leads to capillary instability of the free/segmental cylinder. With the increase of the scanning speed, the track width, the width of the contact zone and the re-melted depth decrease. Finally, for each powder material and set of laser radiation parameters, there exists a range of optimum scanning speeds (Yadroitsev et al., 2013).

The densification of the SLM parts is mainly a function of the laser energy density defined by the following equation:

$$\psi = P / uhd$$

where ψ is the specific laser energy input (J/mm^3), P is the laser power (W), u is the scan rate (mm/s); and h is the scan spacing (mm) and d is the layer thickness (mm). As it is possible to observe in Eq.(2) the energy density increases with increasing the laser power and decreasing the scanning rates, the scan spacing and the layer thickness (E.O. Olakanmi, 2015). The duration of the laser-material interaction controls the degree of consolidation that may be obtained in a material system.

By varying the scanning velocity u and the scanning space, which is the distance between two scanned tracks it is possible to correct the amount of the liquid phase due to the thermal energy induced in the material (E.O. Olakanmi, 2015). At low scan speed, small scan spacing and relatively high laser power, the amount of liquid phase generated is higher and sintering time is longer. Using high scan speed and scan spacing and low values of laser power it is possible to obtain short sintering time and low volume fraction of liquid consequently the liquid phase is not enough or has sufficient time to enhance wettability.

High laser power combined with low scanning rates would generate the laser melting, while high or low laser powers with higher scanning rates would result in laser sintering. Olakanmi *et al.* (2008-2013) during their studies about Al, Al-Mg, and Al-Si powders with CO_2 laser, have defined a sort of energy density threshold between the laser melting and the laser sintering phenomena. Their results underlined that energy densities in the range of 12-16 J/mm^2 were found to be the limit below which laser sintering phenomenon (at 100-240 mm/s and 50-150 W) was predominant and above which (at 50 – 150 mm/s and 100-240 W) laser melting occurred.

Special attention should be devoted to the layer thickness. The thickness of each single layer of powder is a fundamental parameter to ensure the cohesion between the different layers that make up a part produced via laser melting. For this purpose it is essential that

it is less than the depth of the molten pool created by the laser, so as to ensure the partial re-melting of the substrate and so its welding to the current one. However it is good that the thickness of the layers is greater than the average diameter of the particles of the powder used, to ensure a uniform distribution of the powder which constitutes each layer. It is good also to consider that, although the accuracy and the surface finish of component produced via laser melting tend to improve with reduction of the thickness of the layers, reducing this thickness beyond a certain limit will lead to excessive growth of production times without making significant advantages in terms of quality (Yadroitsev , 2012). According to the process requirements, it is possible to balance the importance between the quality of the part and the productivity of the process by an appropriate choice of the layer thickness. It is important to underline that the process parameters developed for a specific metallic alloy, they are optimized relatively a specific range of layer thickness. Changing the layer thickness only also a few micron could affect the global feasibility of the process.

It is possible to check if the amount of the energy density induced in the material is high enough to guarantee the melting between two subsequent layers by using the processing windows. The processing windows for pure-Al, pre-alloyed Al-Mg, and AlSi12 powders were investigated by employing laser power and laser scanning speed in the range of 20-240 W and 20-250 mm/s respectively at constant scan spacing at 0,1mm (E.O. Olakanmi, 2013), (E.O. Olakanmi, 2008). The four regions of behavior identified for all powders were: no marking, partial marking, good consolidation, and excessive balling. The processing windows shows a similar trend for all powders. The region of low partial marking, even though coherently bonded, is characterized by the low strength of the single layer samples easy to fracture. The region of good consolidation is characterized by coherently bonded layers having high strength. In the laser melting process is preferred to construct the multiple layers remaining within the region of good consolidation, while the region of excessive balling which is undesirable is characterized by the formation of large size molten pools inhibiting the subsequent layers construction.

Fig.1.17 shows the relationship between various regions of processing map and surface morphology at laser power of 150W, scan spacing of 0,1 mm, and varying the scanning rates for aluminum alloy powders when its single layer were produced on the bed powder substrate. At scanning rates below 80mm/s, pores appeared larger in size and the inter-agglomerates were fully dense. Increasing the scanning rates between 80 mm/s and 150 mm/s when laser power varies from 120 W and 240 W. resulted in the formation of quite dense structure consisting in small pores (region of minimal balling). Varying the laser power from 50 W to 240 W at high scanning rates (150-240 mm/s), the surface morphology was smooth, but less dense whit lateral pores (region of partial marking). These considerations were conform to the discoveries made by Niu and Chang (Niu HJ,

2000). The pre-alloyed elements in aluminum powders influence the evolution of the nature of its surface morphology during laser melting processing.
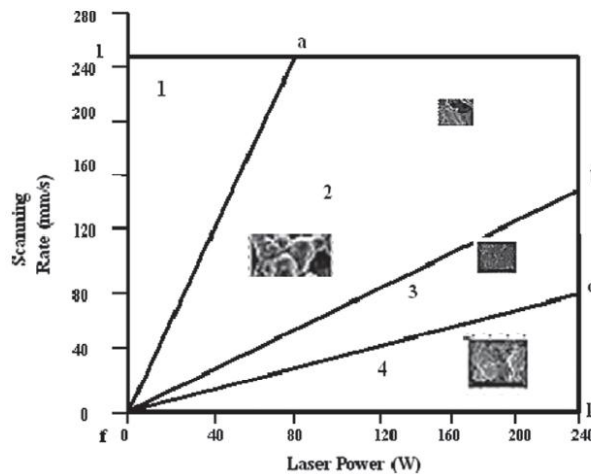
Fig.1.17: Different region indicating how the combination of the Laser Power and the Scanning Rate interfere on the material: 1)No Marking, 2) Partial Marking, 3)Good consolidation, 4)Excessive Balling.

The processing windows' regions with the relative surface morphologies could be attributed to the following reasons:

- The "no marking" region is due to the combination between extremely short duration of the laser-material interaction and lowest energy density (less than 3.2 J/mm^2) which permit the no inter-particulate bonding to take place due to the utilization of scanning velocities above the 50 mm/s at laser powers less than 80 W during the laser sintering process.
- The "partial marking" region is determine by the generation of lower energy density (3.3-10 J/mm^2) resulting from the adoption of laser powers ranging from above 80 to 240 W at scan rates between 80 and 250 mm/s. An inadequate liquid phase is produced which produces low inter-particulate bonding.
- The "good consolidation" region is made by almost dense structure (e.g. 60-80%) consisting of closed pores due to higher energy densities in the range of 12 to less 30 J/mm^2 which leads to the formation of adequate amount of liquid phase promoting the full melting. This results are in agreement with that of Khan and Dickens (Khan M, 2012). The energy densities in this region can vary from 100 to 240 W in laser power and from 80 to 200 mm/s in scan rates. The energy densities in this specific range increase the powder bed temperature, while

reducing the viscosity of the molten pool in the SLM processed powders, improving the densification process with the solid powdered particles.
- The "excessive balling" region is associated to the occurrence of rough and 100% dense structures and it is caused by the highest range of energy densities resulting from the combined effect of higher laser powers at the lower scan rates (80 mm/s or less). Energy densities from 30 J/mm^2 or more is believed to have led the formation of excess amount of liquid phase resulting in the balling formation (Zhang B, 2012).

On the basis of this results, in the next chapter the energy density borderline and the main differences between the laser sintering and the laser melting process will be illustrated.

1.3.2) Laser sintering process and laser melting

As result of the previous discussion, it is possible to state that an energy density function in the range of 12-16 J/mm^2 was found to be the threshold below which the powder bed laser sintering was predominant and above which the aluminum powder bed laser melting occurred. This implies that both the microstructure and the processing window shape of laser sintering/melting are dependent on the laser energy density (see Eq.1) (E.O. Olakanmi, 2015).

The main difference between the laser melting and the laser sintering process is that, while in the first case the energy density is sufficiently high to melt different metallic powder particles between them, in the second case the laser energy provided is sufficiently to induce a temperature in the powder as close as possible to the melting point of the metal particles, but without exceeding it, in order to avoid melting, so that the binding at the interfacial grain contact area occur. The principle of the sintering process with the metal powder is based on the particle fusion at a temperature below the melting point. During the sintering process, a neck forms between the two adjacent powder particles. This reduces the surface area and increases the tendency of the powder to aggregate. The driving force for this reduction of the free surface energy of the particles and the densification is proportional to this reduction (Dongdong Gu, 2010).
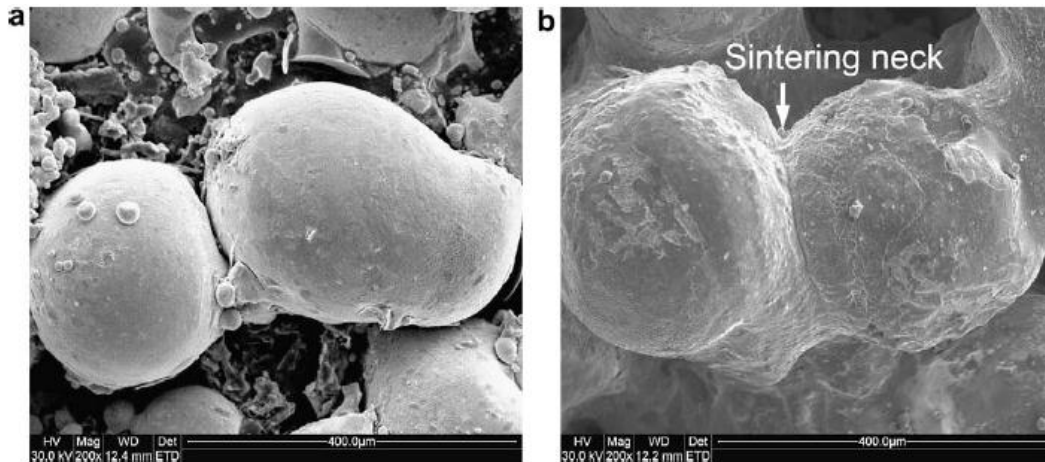
Fig.1.18: SEM images showing typical microstructures of laser sintered stainless steel powder at different laser powers: (a) P = 350 W; (b) P = 400 W (Dongdong Gu, 2010).

When the sintering process occurs (for example due to a not sufficiently high energy density) some problem such as porosity, distortion, and delamination can also occur but a more substantial problem is balling phenomenon. For larger temperatures than the sintering temperature (or complete melting), the molten metal tends to form a spherical, ball-type structure which has bigger dimensions than particle size. As the laser spot size is usually bigger than the particle size, many particles get melted together and forma a bigger spherical droplet. Because of the large size of the droplet, it is connected with other droplets only at certain points on its contour. This is the so-called balling effect, which will be illustrated more in details in the chapter concerning the microstructural and metallurgical defects of the laser melting process.

1.3.3) Effect of the energy density on the densification process

It has established (E.O. Olakanmi, 2015) that the resultant fractional sintered density of laser melting/sintering processed parts is directly correlated with the specific laser energy input incident on a powder bed. The fractional density ρ of these powders is an exponential function of the specific laser energy input ψ:

$$\rho = C_1 - C_2 \, exp(-K\psi)$$

where C_1, C_2 and K (densification coefficient) are material constants of the specific powders under investigation. As said before, the scan speed and the scan spacing influence the wettability of the material and hence the densification process in particular, if wettability is increased (low scan speed, small scan spacing and relatively high laser

power), it is promoted the densification process. Otherwise, if the interaction time between laser and material is not high enough (high scan speed) and the energy density is low (high scan spacing and low values of the laser power), the sintering time are reduced together with the fraction of the liquid phase, reducing also the occurrence of the densification process.

There appears to be a maximum sintered density which may be achieved in powder bed laser melting/sintering processes at a critical value of the specific laser energy input. Above this critical value, it is unsuitable to increase densification further because the increased lifetime of liquid phase promotes the balling phenomenon which inhibits densification.

1.4) Microstructural and metallurgical defects in laser melting fabricated parts

The high thermal gradient together with the high cooling rates induced in the material during the laser melting process, can strongly affect the final microstructure of the fabricated part. In the laser melting process it is possible to employ transient cooling patterns to control grain sizes and shape, phase percentages, and the phase compositions in order to promote the desirable mechanical properties. Longer laser-material interaction or higher energy density during laser melting process (hence lower scanning rates and/or higher laser power) lead to the formation of a superheated molten pool and high temperature (E.O. Olakanmi, 2015). These conditions determine longer time to start the solidifying process of the liquid material and the temperature of the base material becomes higher, thus lowering both the temperature gradient at the interface and the cooling rate. A coarse microstructure may result in this case. Lowering the laser power and/or using high scanning rates, the superheating does not occur and the temperature gradient is high enough to guarantee fast cooling rate leading the formation of fine microstructure.

Also the powder bed temperature, the build orientation and the post process heat treatment on the material, affect the microstructure of the processed part (Brandl E, 2012). In particular, the heat affected zones microstructure of laser melted AlSi10Mg part, during the laser melting processes they could be characterized by inhomogeneities, coarsed cellular dendrites of α-Al and inter-dendritic Si-particles. The post heat treatment has the larger effect homogenizing the microstructure by dissolving dendrites, laser traces, and heat affected zones, while the building direction has the minimum effect on the microstructure of laser melted AlSi10Mg parts.

In their study I. Rosenthal *et al*. (2014) have analyzed the microstructure of AlSi10Mg parts produced via the laser melting technology. They have considered that the macrostructure is determined by the way with which the different individual melt pools are combined, as represented in Fig.1.19. In which two cross-sectional views are shown: top and front views.
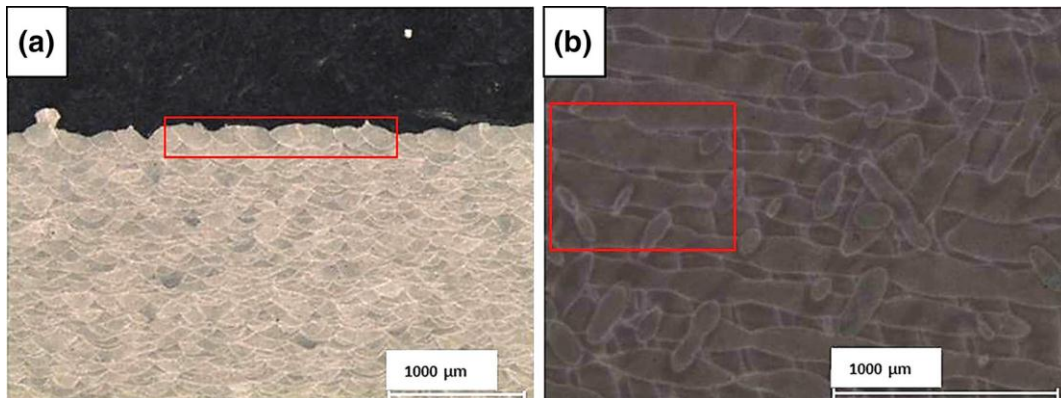
Fig.1.19: Macrostructure of the specimens, example for track segments are marked in *red*: (a) front view of the "fish scale" morphology with melt pool overlapping; (b) top view showing variation of the shape and discontinuity of the melt pools produced in different layers (I. Rosenthal, 2014).

The machine used was a 400 W Nd-YAG laser, and a scanning velocity of 1 m/s was applied and the particle size was in the range of 25-50 µm; by knowing this, it was determine that the pool height was about 150 µm and the width about 300 µm (see Fig.1.20).

Fig.1.20: Close up of track segments, showing the dimensions of the half-cylindrical melt pools. Early formation of a defect can be seen marked by the arrow (I. Rosenthal, 2014).

The applied hatch spacing of 200 µm caused an overlap of about 33% of the melt pool width between neighboring scan tracks, causing the partial re-melting of the material. During the build process, each initial seam was re-melted locally up to four times, ensuring chemical homogeneity and microstructural regularity of the final structure. The

combined effect of directional cooling and rapid solidification induced by repeated thermal cycles has a profound influence on the microstructures of the alloy deposited as explained in the previous paragraph. The microstructure of the additive manufacturing samples differs completely from those fabricated by casting (as seen in Fig.1.21). This has a direct effect on mechanical properties and is addressed in the mechanical properties section.
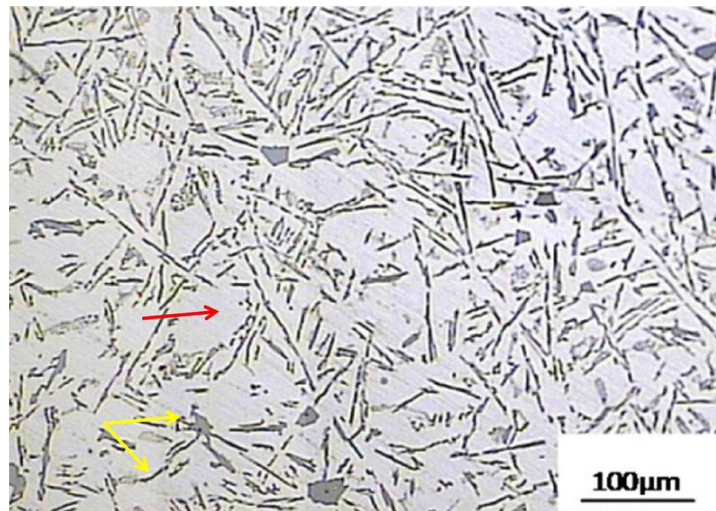
Fig.1.21: Typical microstructure of an Al–Si cast alloy. *Red* arrow marks the Al matrix; *Yellow* arrows mark the Si particles in the eutectic mixture (I. Rosenthal, 2014).

Three main areas of different microstructures are observed in the samples (Fig.1.22), namely 1-coarse fusion zone (FZ), 3-fine FZ cellular structure inside the melt pool, and 2-heat-affected zone (HAZ) appearing as broken cells between the FZs. The relatively narrow HAZ is attributed to the limited amount of heat from the concentrated laser beam.
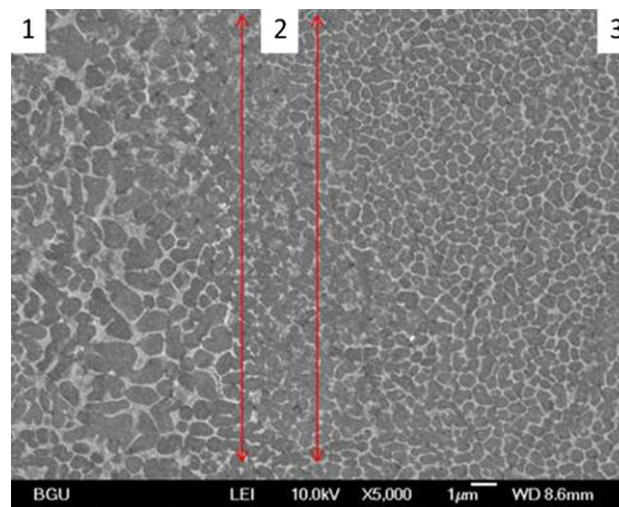
Fig.1.22: Microstructures of the fusion zone; 1-coarse fusion zone; 2-heat-affected zone; 3-fine fusion zone (I. Rosenthal, 2014).

1.4.1) Effect of the molten pool geometry on the microstructure and epitaxial solidification

The geometry of the molten pool depends on different process parameters (E.O. Olakanmi, 2015). For example, when the heat input is just enough to melt the powder and the energy density is less than a critical value, the melt pool will show a cylindrical geometry due to high surface tension. In this case the contact are between two subsequent layers will be smaller, also the heat conduction and hence the cooling rate will be reduced. Considering a multiple layers laser melted product, the substrate layer are pre-heated or partially melted influencing the cooling rate and hence the microstructure.

The epitaxial solidification is the growth process of an atomic layer above a material substrate, in which the structure of the growth material is a function of that of the substrate (E.O. Olakanmi, 2015). Hence, the growth depends on characterizing parameters of the substrate (for example orientation and temperature) and of the material to be placed. In order to better explain this concept, the SLM process could be linked to the fusion welding. The two processes can be compared, however the main difference is that in fusion welding the base metal and the weld metal may have similar but not necessarily the same composition, while in the laser melting processes the substrate layer and the new layer of the metallic powder to be melted have the same composition. In order to have a good weld the dilution is the main requirement. Dilution is the partial localized re-melting of the base material that provides a continuous interface free of oxide films or other contaminants between solidifying liquid weld metal and the base metal. Along the solid-liquid interface occurs the grain growth. In the pwder bed laser melting process the

epitaxial solidification mechanism leads to the formation of a nucleus of solid from its melt in contact with a substrate as it occurs in the fusion welding process, the fusion energy required for the initiation of nucleation is a function of the wetting angle (θ) between the substrate and the new solid formed layer.

The relationship between wetting angle and interfacial energies is illustrated in the following equations:

$$W_a = (\gamma_{SV} + \gamma_{LV} - \gamma_{SL}) = \gamma_{LV} * (1 + cos\theta)$$

$$cos\,\theta = \left(W_a / \gamma_{LV}\right) - 1$$

where γ_{LV} is the surface tension of the liquid-vapor interface, γ_{SV} is the surface tension of the solid-vapor interface, γ_{SL} the surface tension of the solid-liquid interface and θ is the contact angle. During the epitaxial solidification, both the contact angle, (θ), and the free energy ΔG^*, become zero, and the growth of the solid initiates without any difficulty or better any barrier:

$$\Delta G_{het} = S(\theta) * (-V_S\,\Delta G_V + A_S \gamma_{SL}) = S(\theta) * (-^4/_3\,\pi r^3 \Delta G_V + 4\pi r^2 \gamma_{SL})$$

ΔG_V is the free energy change per unit volume directly linked to the nucleus formation, V_S is the volume of the nucleus, A_S is the surface area of the new interface created by the solid nucleus and the liquid, and $S(\theta)$ is the shape factor function of the contact angle.

r^* ,that is the critical radius for heterogeneous nucleation, is obtained deriving the ΔG_{het} with respect the radius and setting the first the first derivative equal to zero obtaining

$$r^* = (2\gamma_{SL}) / \Delta G_V$$

the associated free energy barrier ΔG^*, for heterogeneous nucleation is obtained by substituting in the expression the critical radius r^*:

$$\Delta G^* = 16\pi \gamma_{SL}^3 * S(\theta)/3\Delta G_V^3$$

During the powder bed fusion, the main condition for the epitaxial solidification occurrence is the partially re-melting of the substrate, to promote the growth from the prior grains. In order to promote this phenomenon, the laser melting process parameters have to be choice considering that the provided energy density need to be able to re-melt a sufficient amount of substrate material. Thus, it is possible to obtain a strong interlayer bond resulting in full density components. Being the powder bed laser melting a localized solidification process occurring via epitaxial growth, the microstructure can be controlled, or better, it is possible to obtain finer and more uniform grain resulting in better

mechanical properties. For example, it can consider that re-melting the previous layer makes possible the removal of contaminants, the breaking down of oxide films, the providing at the atomic level of a clean solid-liquid interface;

Microstructure may be predicted by analysis of the variables R, growth rate, and G, temperature gradient at the solid–liquid interface. High G/R ratio corresponds to a stable planar front of crystallization while low G/R ratio causes instability of the crystallization front and dendritic solidification. Cellular growth corresponds to intermediate magnitudes of the G/R parameter.

Characteristic length of the microstructure is governed by $R \times G$, i.e., the cooling rate value. The higher cooling rate, the finer microstructure features are (cell spacing, inter-dendritic space, size of dendrites, etc.) (I. Yadroitsev, 2013).

The mechanism of distortion, irregularities and drops formation may be associated with thermophysical properties of the material, granulomorphometric characteristics of the powder, peculiarities of its deposition and spreading, layer thickness, energy parameters of laser radiation, laser scanning speed, and melt hydrodynamics (Yadroitsev et al., 2013).

1.4.2) The balling effect

The *balling effect* is a typical phenomena related to the laser sintering/melting process severely degrading the process quality itself. Different researchers aimed to deepen more in details this type of phenomena occurring during the process. Dongdong Gu *et al.*(2009), during the investigation of the balling phenomena of a stainless steel powder have distinguished mainly two type of balling phenomenon: the first is the coarsened balls caused by limited liquid formation and the second is micrometer-scaled balls induced by melt splashes (see Fig.1.23).

They have associated this phenomena to the amount of the liquid formation which depends on the operating temperature controlled by two main parameters, i.e., the laser power and the scan speed. Let's now consider the first case, that of the coarsened balls. For a given scan speed, the supersolidus sintering temperature decreases with lowering the laser power, resulting in a smaller amount of liquid formation. The viscosity of the liquid-solid mixture, thus, becomes considerably high, handicapping liquid flow and particle rearrangement. This in turn decreases the overall rheological performance of the liquid in conjunction with solid particles. Consequently, the molten materials in each spot irradiating zone tend to aggregate into an individual coarsened sphere approximately the diameter of laser beam. The initiation of this kind of balling phenomenon is schematically depicted in Fig.1.23.
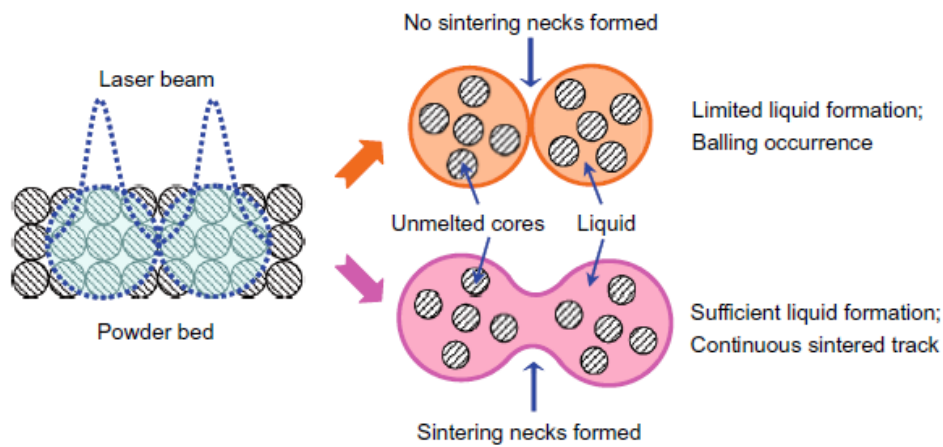
Fig.1.23: Two different types of balling phenomena distinguished by Dongdong Gu *et al.*(2009).

In this situation, no efficient bonding is obtained between the neighboring balls, since the limited amount of liquid prevents the sufficient growth of sintering necks between metal agglomerates. On the other hand, a low laser power results in a limited undercooling degree of the melt. Thus, coarsened and discontinuous dendritic structures are developed in surface layer of these solidified balls, producing an inherent weakness in laser sintered powder.

As concern the second case, when a sufficient amount of liquid phase is generated by using a relatively high laser power, laser sintering at a high scan speed the laser process tends to shape the melt into a continuous cylindrical molten track due to a considerably short stay time of laser spot on each irradiating region. However, the present molten track is in a highly unstable state. With increasing the scan speed used, the linear energy density of laser input decreases, resulting in a decrease in the working temperature. and, accordingly, the diameter of cylindrical molten track. The melt instability, consequently, increases significantly. Under this condition, a number of small-sized liquid droplets tend to splash from the surface of the molten track, due to the reduction in the surface energy of liquid at short length scales. After solidification, a large amount of micrometer- scaled spherical splashes are formed around the sintered surface, resulting in the second of balling phenomenon.

The conclusions of the experiments was that increasing the input energy density, which was realized by increasing laser power, lowering scan speed, or decreasing powder layer thickness, gave a high feasibility in alleviating balling phenomena.

Ruidi Li *et al.* (2012) have investigated the effect of the oxygen content on the balling phenomena of a stainless steel and it was possible to observe that the oxygen content in atmosphere plays a crucial effect on the balling characteristics. At a relative low oxygen

content the morphologies of as-received scan tracks were clear and overlapped in a favorable condition, yielding a flat surface without big-sized balling except a small number of small sized balling when the oxygen content was increased the scan tracks became indistinct, coupled with the generation of visible big-sized balling. At a more higher oxygen content, the scan tracks became discontinuous, accompanied with serious balling phenomenon and deteriorative surface condition. It was reasonable to conclude that oxygen in atmosphere has a pronounced effect on ball formation, due to the oxidation of molten pool and accordingly worsened wetting characteristic with oxide at the wetting interface.
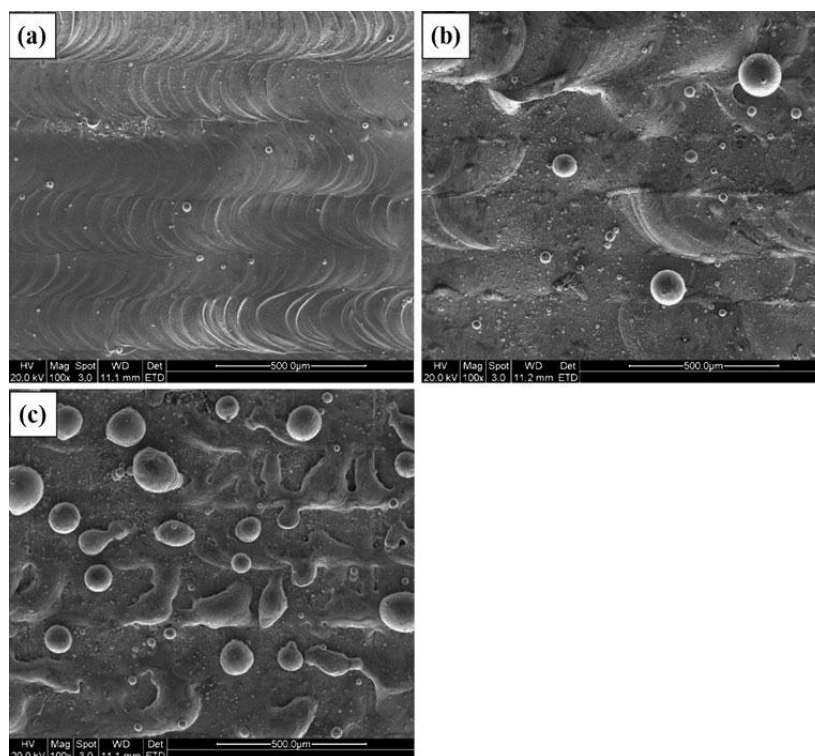
Fig.1.24: SEM image showing the balling characteristics in a stainless steel under different oxygen contents in atmosphere: a 0.1%; b 2%; c 10%; (Ruidi Li, 2012).

1.4.3) Porosity

The powder bed laser melting process has the advantage that the powder which remains unused during the process can be recycled in the subsequent process. However, it is necessary to pay attention to all that factors, such as incomplete melting, entrapment of gases by surface turbulence, porosity following the shrinkage and the moisture, which is present in the atmosphere, affecting the powder triggering different phenomenon during the laser melting process. The main causes of the porosities in the laser melting processed parts are: the incomplete melting porosity, the entrapment of gases by surface turbulence and porosity following shrinkage. When insufficient dissipation of the laser energy density into the powder layer thickness poor fusion porosity could occur. Instead the entrapment of the gas bubbles could result from an unstable scan track, because the vapor formation process is not uniform in the material (E.O. Olakanmi, 2015). This is why the powder bed laser melting processes need to guarantee the stability balancing the involved active forces. With the formation of a vapor cavity, the fluid forces of the molten pool tend to be balanced by the vaporization pressure within the cavity. In order to reduce the porosity the scan track must be kept stable by employing high power and speed (Kobryn PA, 2000). The use of continuous wave Nd:Yag lasers results in a less severe plasma effects with respect the CO_2, thanks to its shorter wavelength (of Nd:Yag).

Some differences in the results can occur by varying the laser processing mode from pulsed wave (PW) to the continuous wave (CW). In particular, there is a scanning speed in PW mode, at which the degree of porosity inside the material reaches the maximum. Imposing high energy density (low scanning rates/high laser power) and reducing the depth of the scan track at low energy density (high scanning rates/low laser power) may induce the delay solidification time and hence the gas escaping. Pulsed laser system may provide the possibility to control the energy dissipation into the powder bed and substrate and thereby control the solidified microstructure, porosity, and solidification cracking (Fischer P, 2004). It is recommended to shorten the off-time of the pulse to less than the solidification time of the molten pool (E.O. Olakanmi, 2015). A pulsed shape with gradually decreasing peak power levels or possibly combined with the use of a CW laser beam can also be used to reduce or prevent porosity and cracking (Abe F, 2001). Using a CW lasers a more stable scan track can be obtained.

The surface turbulent flow of liquid metal in the molten pools could be another important mechanism in the porosity formation. Gases are entrapped into the liquid metal in molten pool via surface turbulence (but not bulk turbulence). The gas species could be vapor, shielding gas, or their combination. The shrinkage porosity occurs during the solidification as a consequence of inadequate metal feeding (Olakanmi EO, 2011).

During their study, C. Weingarten *et al.* (2015) have investigated the presence of the moisture in the laser melting process and if the hydrogen porosity in AlSi10Mg parts built up with laser melting technique can be lowered by efficient drying of the powder as well as by the modification of the process parameters.

At first it was investigated the influence of the moisture on the gas pore density. In a first step of the examination, the gas content of the voids was studied. The results of the examination indicate that approx. 96% of the gas content in the voids is hydrogen. In order to determine the hydrogen sources in the laser melting process, two measurements were performed. The hydrogen content of the moisture on the surface of the powder particles was measured by Karl–Fischer-Titration (KFT), which shows that a virgin powder batch contains 0.015 mass-% H2O on the surface of the powder grains, and it was discovered that it is the dominating hydrogen source and has to be reduced by a drying process. The amount of trapped hydrogen in the powder material depends on the powder atomization process

Two methods were investigated in order to to reduce the moisture on the powder surface. The first method is an external drying of the powder in a furnace at a constant temperature. The influence of two different external drying temperatures ($T_{heat,1}$ = 90°C, $T_{heat,2}$= 200°C) was studied by manufacturing laser melted samples with each powder and measuring the pore density of each sample. It is shown that the drying of the powder may reduce the porosity by up to 35% at a drying temperature of $T_{heat,1}$= 90°C and at $T_{heat,2}$= 200°C by more than 50%.
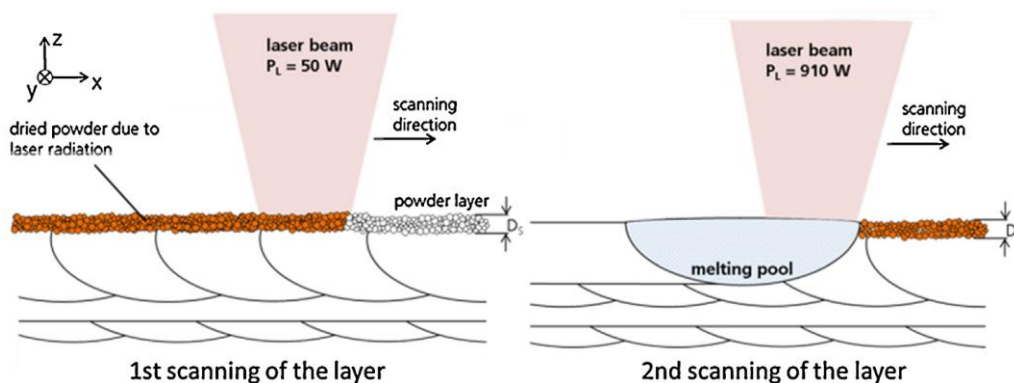
Fig.1.25: Schematic illustration of the internal laser drying process (C. Weingarten 2015).

The second method to reduce the moisture at the powder surface is an internal laser drying. For this purpose the powder is dried during the process right after the layer deposition. The heat source for the drying is laser radiation with low power. Hence, each scan vector in the layer will be scanned twice. The first scanning of the whole surface is to reduce the moisture without melting the powder. The second scanning of each scan vector is the melting process. Visual inspections show that the first scanning with a laser power of P= 50 W leads to a soft sintering of the powder.

The results show that this drying method reduces the pore density from ρ_P= 1.6% to ρ_P=0.3% when a laser beam diameter of 0.3 mm and scan speed of 1000 mm/s are used. The density of the laser melting sample is raised up to over 99.5%.

As second step the influence of the scan speed on the hydrogen pore density was investigated, in particular the influence of the scan speed while using a laser beam diameter $d_{s,1}$= 0.3 mm. An increase of the scan speed results in a decrease of the pore density. From 1000 to 2500 mm/s (without powder drying) a decrease from ρ_P= 1.2% to ρ_P= 0.5% can be achieved. This is a reduction of approx. 60%. Because the intensity of the energy decreases from approx. 12.9 to 1.2 kW/mm^2 while the laser beam diameter increases from 0.3 to 1 mm, a lower scan speed (150–350 mm/s) has to be used to manufacture laser melting samples without imperfections. The scan speed used is limited by the process window to obtain sound parts without, for example, appearance of spattering or agglomeration. In contrast to the pore density of the samples built up with $d_{s,1}$= 0.3 mm the pore density of the samples built up with $d_{s,2}$= 1 mm increases from 3.3% to 9.3% for scan speed below 300 mm/s. When the span speed is raised to above 350 mm/s, gas porosity falls.

Laser melting samples built up with a laser beam diameter of 1 mm have a significantly higher pore density than those built up with a laser beam diameter of 0.3 mm. The cause for this difference is the depth of the heat-affected zone (HAZ). With the HAZ the zone of the temperature interval below melting temperature is described, which affects the solid material in terms of recrystallization, pore growth, etc. The HAZ is not mainly caused by the difference of the beam cross section in the focus position but by the different scan speed. In case of constant laser power, the scan speed has to be reduced by increasing the laser beam diameter to build up dense components. High scan speeds (vs> 1000 mm/s) lead to a short interaction time between laser radiation and material as well as a rapid cooling.

In the third step it was analyzed the influence of the laser beam diameter on the hydrogen pore density. The laser melting samples were built up with the two different beam diameters $d_{s,1}$= 0.3 mm and $d_{s,2}$= 1 mm. The temperature distribution of the melting

process in laser melting process was calculated with a FEM simulation. The results have shown that when the laser beam diameter $d_{s,1}$ is used, a higher local maximum temperature $T_{max,1} \approx 3200°C$ is reached. This is caused by the higher intensity. By contrast the local maximum temperature of $d_{s,2}$ $T_{max,2} \approx 2200°C$ does not reach the evaporation temperature of aluminum (TV=2470°C). Another difference is the penetration depth of the heat. At $d_{s,2}$ (vs= 200 mm/s), the heat extends deeper into the solid material. The melt pool depth using $d_{s,1}$ in the analytical solution is approx. 0.15 mm and approx. 0.52 mm using $d_{s,2}$. The melt pool length amounts to 0.66 mm ($d_{s,1}$) and 1.7 mm ($d_{s,2}$).
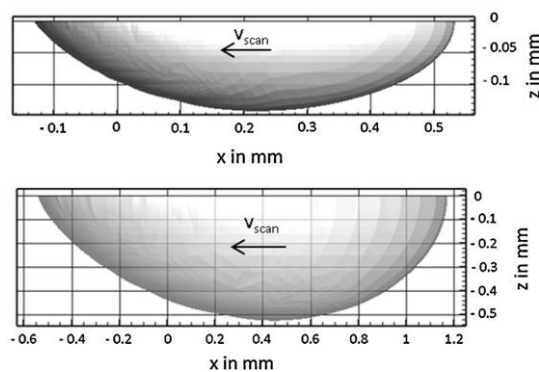
Fig.1.26: Melt pool geometry in the quasi steady-state condition. Upper: $d_{s,1}$; below: $d_{s,2}$; (C. Weingarten 2015).

In addition to the influence of the scan speed and the laser beam diameter, the influence of the process parameter "scan break" was investigated. The scan break (T_s) describes the time between the end of the scan vector and the starting point of the following scan vector. When the scan break increases, the work piece cools down, which, therefore, means there is a lower local preheating temperature of the following scan track. Laser melted samples with different scan breaks of 0, 25 and 50 ms were built up and analyzed for the hydrogen pore density, using a laser beam diameter of 0.3 mm. The results have shown that increasing the scan break from 0 to 50 ms, the pore density is reduced by 87% (vs= 1000 mm/s) and 75% (vs= 2000 mm/s).
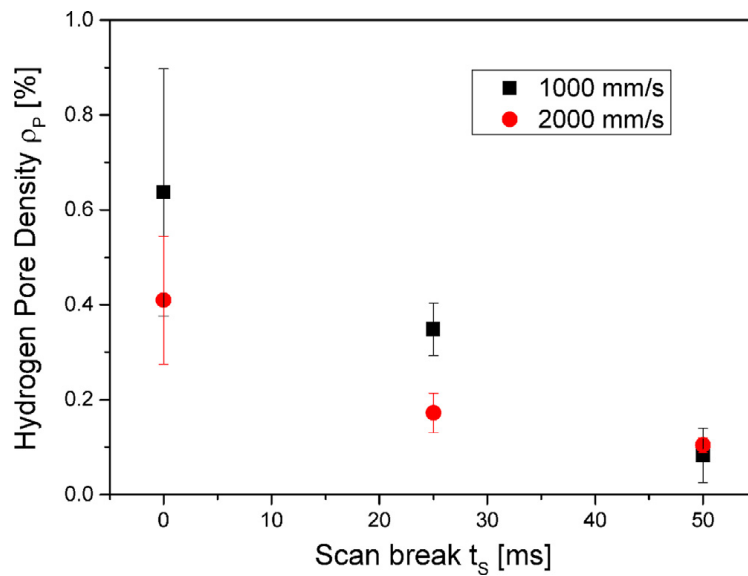
Fig.1.27: Hydrogen pore density of SLM samples depending on the scan break, $d_{s,2}$ = 0.3 mm, P=910W. (C. Weingarten 2015).

When the hydrogen porosity occurs the moisture (H_2O) reacts by contact with aluminum by means of the following equation:

$$3H_2O + 2Al \rightarrow Al_2O_3 + 3H_2$$
$$H_2 \rightarrow 2H_{ab}$$
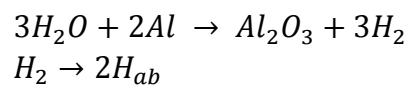
where H_{ab} is the absorbed hydrogen in the melt.

Physical mechanism of pore growth in laser melting process is explained in Fig.1.28.
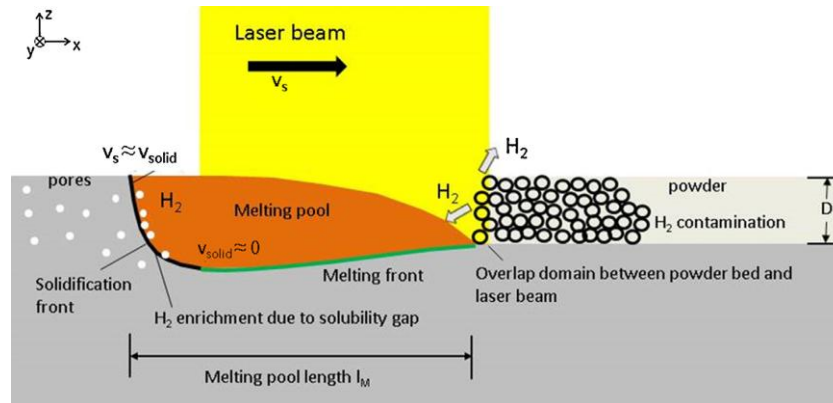
Fig.1.28: Schematic overview of the interaction zone between laser radiation and powder (C. Weingarten 2015).

The laser beam moves in scanning direction and its energy absorbed by the powder. A melt pool is created, which is deeper than the layer thickness, resulting in metallurgical bonding between the layers. The solid–liquid interface consists of the melting front and the solidification front. The melt can be enriched with hydrogen by the interaction of the melt front and the powder particles. If the local solubility limit of the melt is reached, pore nucleation is initiated. The growth of the pores is diffusion controlled such that the further hydrogen supply takes place over the gaseous liquid interface of the pore. The supply rate of hydrogen is limited by the diffusion process of hydrogen within the boundary layer of the pore and the local solidification rate. That means that the growth is stopped if the pore is captured by the solidification front. The laser melting process occurs generating high solidification rate, and thus the solubility is increased. When more hydrogen atoms are trapped and the solubility exceeds the equilibrium solubility of the solid phase, a metastable state is generated. This metastable state can relax by pore precipitation during heat treatment for precipitation hardening. If the melt pool surface is free from oxides or other contamination, the so-called Marangoni convection is involved. If the surface tension coefficient is negative, the flow direction on the melt pool surface is directed radially outwards from the center to the melt-pool boundary. The pore formation can be reduced when the powder particle contamination with hydrogen is lowered or an adequate process management is used. When the scan speed is increased, the solidification increases and, thereby, a metastable phase is generated. The influence of the processing strategy onto the Marangoni convection is difficult to predict because the surface tension coefficient is sensitive to the temperature and chemical composition.

1.4.4) Cracking

The large solidification temperature range, high coefficient of thermal expansion, and the large solidification shrinkage could be the main causes of crack formation (E.O. Olakanmi, 2015). The main cracks type encountered in the powder bed laser melting process are the liquation cracks, which are due to the high amount of alloying elements with low melting point, and solidification cracks, which are a function of the interaction among the increased strain rate and the total strain resulting from external displacement and internal free shrinkage related to the ductility curve. However, the solidification cracking in aluminum alloy parts are influenced by temperature range of dendrite coherence, and the amount of liquid available during freezing. The lacking of diffusion processes during laser melting processes due to rapid solidification contributes to enhance the crack formation. The addition of alloying element with the aim to narrow the critical solidification range can also alter the molten pool composition to avoid cracking. Alloying elements and impurities are segregated at the grain boundaries (Liu R, 2006), (Sreeja Kumari SS, 2007).

The solidification cracking is correlated to the laser melting process parameter, in particular, in aluminum alloys, an optimum laser energy density exists at which a crack-free fully dense part is obtainable. Above this value, solidification cracking occurs and below this value, a disorderly liquid solidification front and balling effect result in crack formation due to an enhanced instability of the liquid caused by Marangoni convection (E.O. Olakanmi, 2015). The rapid cooling enhances the development of high thermal shrinkage and increases stress gradient that promote high crack initiation rate, also it reduces the time required for residual liquid to refill and restore the initiated cracks.

1.4.5) Laser re-melting

In order to overcome some limitations of the laser melting process, e.g. high surface roughness and residual porosity, the laser re-melting can be applied during or after the process itself (E. Yasa., 2011) That is, after scanning layer (intermediate or final layer) and meting the powder, the same slice is scanned again before putting a new layer of powder. However this technique increases the production time and can be considered as ultimate solution for applications where a density of 98-99% is not sufficient or where part density is very critical for crack formation and propagation. Laser re-melting can also be applied only to the last layer or the outer skin of the part if the only aim is to enhance the surface quality or shell density.

Being the insufficient surface quality one of the most limitation of the laser melting process, it can be enhanced by employing a variety of surface modification technologies, including mechanical (e.g. abrasive sandblasting), chemical (e.g. acid etching or ECM) and thermal processes (e.g. plasma spray). Laser re-melting may be an easy solution for improving the surface quality of the outer surfaces of laser melting parts without need for additional production equipment and for removing the part from the building platform which avoids fixation errors.

Another limit that can be overcome by using this technique is the residual porosity which, as already said, may be detrimental for some mechanical properties, such as the wear performance, toughness or ductility. Thus, laser re-melting may be an ultimate solution where highest possible density is required.

Multi-pass re-melting influences microstructure of the previously synthesized tracks and layers. The last scan not only re-melts parts of previous tracks but affects regions beneath, causing thermally activated diffusional processes like phase transformation, grain growth, precipitations etc. As a result, a multilayered object with non-uniform microstructure, grain size and shapes, non-equilibrium phases is formed. therefore changing the process parameters and scanning strategy would affect the final microstructure and properties (Yadroitsev et al., 2013).

1.5) Mechanical properties of the laser melted parts

It is object of interest to understand how the final density of the product affects the mechanical properties and the effect of the pores on the structural integrity as concern the impact energy, the fracture toughness, and the fatigue strength). The problem correlated to the pores is that they reduce the effective load capacity of a material, acting as stress concentrators inducing the crack initiation. They also influence the fatigue behavior (Grayson GN, 2004), in particular the crack initiation occurs at the surface or just below in close proximity to the sub-surface pores. The fatigue fracture surface is characterized by veins of oxide caused by the presence of residue alumina film on the aluminum powder particles.

In order to better understand the nature of the failure it is required to have an analysis of the microstructure and of the fracture surface. The presence of the dimples on the SEM fractured surface indicates that the failure is ductile while the brittle fracture is characterized by cleavage with each fractured grain flat and differently oriented (Callister WD., 2007). The impact energy and the fracture toughness are also sensitive to pores. The impact energy is the energy needed to fracture the sample, while the fracture toughness is the energy required to growth the crack (German RM., 1998).

1.5.1) Tensile strength

The tensile strength is primarily dependent on the fractional density. As observed in other studies, higher laser sintering/laser melting part densities were obtained by using a lower layer thickness (Agarwala M, 1995), (Simchi A, 2003). However, the minimum layer thickness that can be successfully employed is determined by various factors and most importantly by the maximum particle size in the system.

A further study was carried out, in order to evaluate the influence of the build direction on the tensile strength, by K. Kempana *et al.* (2012) and E. Brandl *et al.* (2012), in which different mechanical properties were analyzed on AlSi10Mg fabricated parts with different building orientation (Fig.1.29).
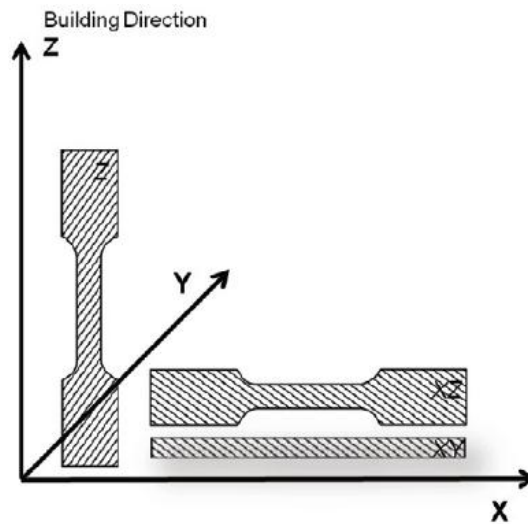
Fig.1.29: Building direction of test samples (K. Kempena, 2012).

A first observation shows that laser melted AlSi10Mg parts have mechanical properties higher or at least comparable to the casted AlSi10Mg material (as it is possible to see in Tab.1.4).

Tab.1.4: Mechanical properties for laser melted parts and cast + aged parts (K. Kempena, 2012).

	E [GPa]	UTS [GPa]	ε_{break} %	HV
XY direction	68 ± 3	391 ± 6	5,55 ± 0,4	127
Z direction		396 ± 6	3,47 ± 0,6	
Conventional and aged				86
High pressure die casting F*				95-105
High pressure die casting T6*				130-133

*For the high pressure die casting AlSi10Mg parts, the properties for as-cast (F) as well as for the aged (T6) condition are given.

The Vickers hardness of the as built laser melted parts is much higher (almost 30Hv) than the hardness of the high pressure die casted (HPDC) AlSi10Mg in the as-cast condition and almost as high as the HPDC AlSi10Mg in the aged condition. The ultimate tensile strength of the as built AlSi10Mg laser melting parts is always higher than those of the HPDC in both conditions. The elongation of the as-built AlSi10Mg parts in the Z-direction is comparable to the HPDC parts, while the elongation for parts built in XY-direction is almost 2% higher. Although the strength and hardness is higher, the Charpy impact energy (Tab.1.5) of the as-built SLM samples is still superior to that of the conventionally casted AlSi10Mg material.

Tab.1.5: results of Charpy impact testing (K. Kempena, 2012).

	Impact Energy [J]
XY-direction	3,94 ± 0,50
Z-direction	3,69 ± 0,48
As-cast	2,5 – 3,0

From the tensile test results, it was possible to observe that the laser melted samples show anisotropy in their properties. A comparison between the stress-strain curves for the two directions show a different strengthening behavior (see Fig.1.30). As a result, the elongation at break is seen to be lower for the XY oriented samples compared to the Z oriented samples.
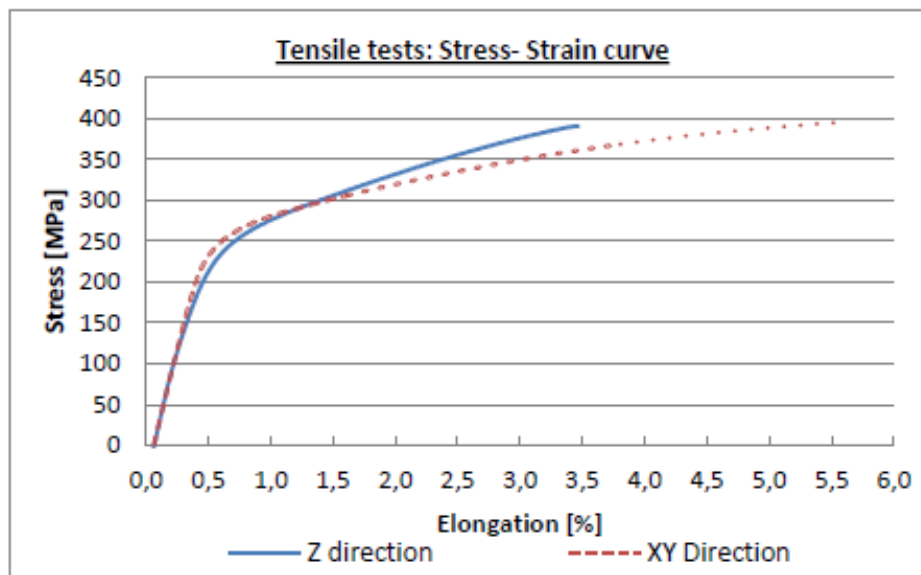
Fig.1.30: Stress-Strain curve for SLM-parts produced in different directions (K. Kempena, 2012).

While tensile tests show a significant difference in ductility between parts produced in XY-direction and parts produced in Z-direction, this difference in ductility is not significant for Charpy test results. In tensile tests, deformation is much slower (0.4 mm/mm min^{-1}) than for Charpy impact tests. Furthermore, it is interesting to notice that all samples were seen to break at UTS (Ultimate Tensile Stress).

Upon observation of the fracture surface of a tensile sample, it can be seen that larges pores near the border of the sample initiate the fracture. These 'borderline pores' are formed at the beginning/end of a scan vector. As illustrated in Fig.1.31, these borderline pores are more numerous in parts produced in the Z direction, compared to parts produced in the XY direction. These pores are the largest defects present in the part. At a high stress

level (i.e. 395MPa for both testing directions), they will become the critical defects which initiate inhomogeneous deformation. Because of their location close to the sample border, they lack space for extensive deformation and easily cause complete fracture of the sample. Due to the faster strengthening of the Z direction, this high stress level is reached sooner and as a result the elongation in tensile test is lower: 3,47% compared to 5,55% for XY oriented samples.
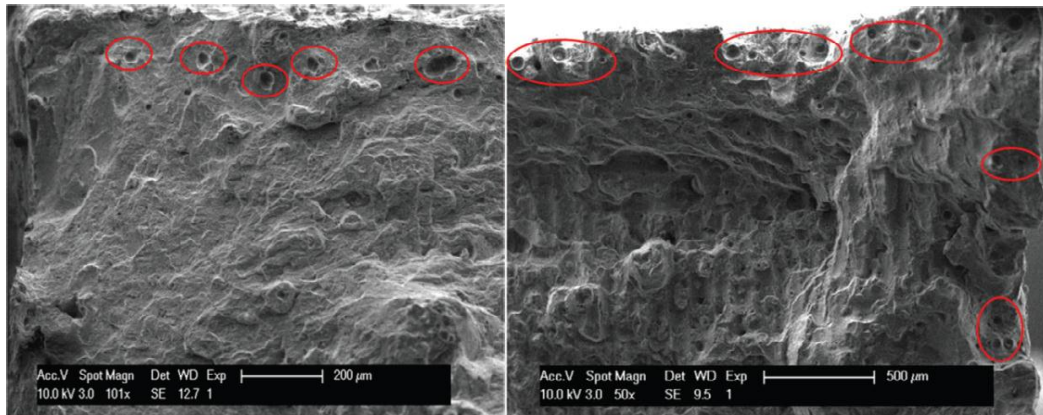
Fig.1.31: Tensile sample fracture surfaces show presence of borderline porosity: in one direction for XY-samples (on the left), in two directions for Z-samples (on the right), (K. Kempena, 2012).

For the researchers were possible to conclude that the SLM AlSi10Mg parts have mechanical properties, such as UTS, elongation, impact energy and Hardness (as we will see), higher or at least comparable to the casted AlSi10Mg material, because of the very fine microstructure and fine distribution of the Si phase (K. Kempena, 2012).

The powder properties is also a significant factor influencing the tensile strength of selective laser melting fabricated parts. The outcomes of a study (Spierings AB, 2011), in which three different powder granulations has been used, has shown that two powders having different particle size distribution, but of finer granulation, had a comparable high tensile strength; in contrast to the last powder having lower tensile strength. This behavior was attributed to the larger pores correlated to the coarser powder in comparison to the finest one.

The energy absorption requirement of bigger particles to achieve full melting is higher in comparison to the smaller particles as explained by Eq (9):

$$\frac{E_{av}}{E_{need}} = \frac{A * I_0 * \pi * r^2}{\left(\frac{4}{3}\right)\pi * r^3 * \rho * \left(C_p \Delta T_m + L_m\right)} = \frac{1}{r} * \frac{3AI_0}{4\rho(C_p \Delta T_m + L_m)}$$

Where C_p and L_m are the specific or latent heat of the fusion, respectively. A is the absorption coefficient of the powder material and I_0 the intensity of the laser beam. According to this study, processing coarse powders via laser melting leads to a generally higher effective powder layer thicknesses which reduces the amount of energy reaching the underlying surface. Consequently, reducing the thermal penetration depth prevents a reliable connection of the layers via the re-melting process of the underlying surface, resulting in more inhomogeneus regions like cracks and incomplete fusion in the material. This decrease the fracture toughness (K_{IC}), because the cracks have their long axis in parallel to the layer orientation so that the external loads perpendicular to the layers open the cracks. This explains the reduction in the tensile strength of samples made of coarse powders and built in the vertical direction (90°).

1.5.2) Fatigue

Similarly the conventional fabricated parts, the presence or absence of microstructural defects, such as porosity or shrinkage cavities, influences the fatigue behavior of the material. In laser melting components the presence of low melting porosity in between their layers reduces the effective load-bearing area perpendicular to the layers in z-direction and causes a stress concentration (notch effect), reducing the static and dynamic strength along this direction (E.O. Olakanmi, 2015). By varying the powder bed temperature, peak hardening heat treatment, and the build direction it has been possible to study the variation on the microstructure and the fatigue response of laser melting processed AlSi10Mg (Brandl E, 2012) alloy.

The study conduced by E. Brandl *et al.* (2012) was interesting from the point of view of the high cycle fatigue (HCF) properties. In this study some AlSi10Mg samples were fabricated by using the laser melting technique, at different build platform temperature (30°C-300°C) and by setting three different build direction (respect to the *x-y* plane the three build angle were 0°, 45°, 90°) (Fig.1.32)
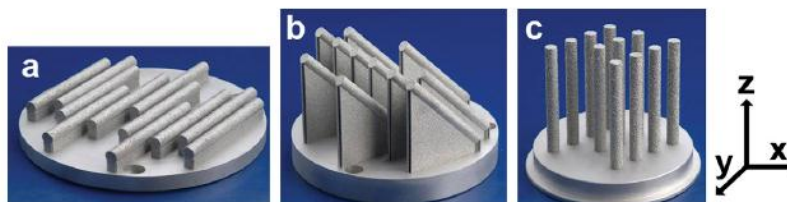
Fig.1.32: Samples (static tensile) built in different directions: (a) 0°, (b) 45°, and (c) 90° (E. Brandl, 2012).

Some samples were peak-hardened (PH) to T6 condition:

- Solution heat treatment for 6 h at 525 °C.
- Room temperature water quench.
- Artificial aging for 7 h at 165 °C.

The particular peak-hardening (chosen from experience) usually results in maximum tensile and yield strengths with adequate elongation. Peak-hardening was carried out before final machining of the samples to remove the surface layer that was influenced from the treatment (e.g. residual stresses, distortions, inclusions).

Different mechanical tests were carried out and the fatigue resistance have shown a different behavior according to the build direction. Fig.s 1.33-1.35 show the fatigue resistance (σ_{max}), i.e. $\sigma_{max} = \sigma_{min}/0,1$, versus number of cycles. The maximum stresses σ_{max} applied were determined with respect to the yield strengths of the batches, previously published.

The 30 °C/0°/ Peak-hardened batch (#10) shows the highest fatigue resistance and the as-built batches (#13, #15, #17) show the lowest one. According to DIN EN 1706 , the fatigue resistance to rotating bending of EN AC-AlSi10Mg(Fe) at 5×10^7 cycles is σ_{max} = 60–90 MPa. All batches tested exceed this range (mostly by far). It was possible to observe that:

- For the 30 °C/Peak-hardened samples: the fatigue resistance is higher in 0° than in 45° and 90°direction.
- For the 300 °C samples: peak-hardening increases the fatigue resistance considerably.
- For the 300 °C samples: the fatigue resistance is comparable in 0°, 45°,and 90° direction.
- For the peak-hardened samples: the fatigue resistance in 45° and 90° direction is significantly higher when built at 300 °C than at 30 °C.
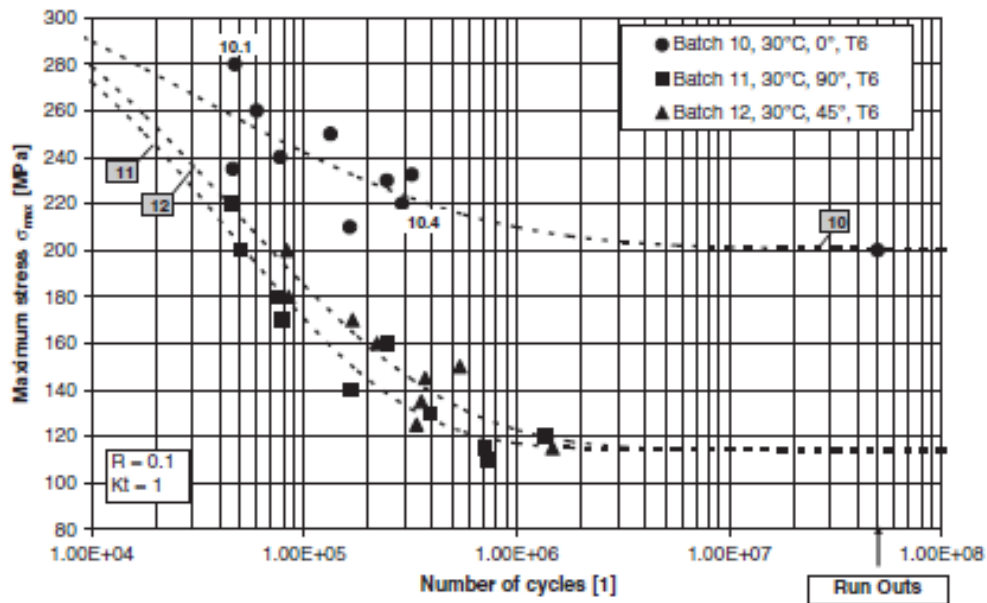
Fig.1.33: Fatigue resistance and Weibull distribution (50% probability of failure) of batches that are built at 30 °C platform temperature (E. Brandl, 2012).
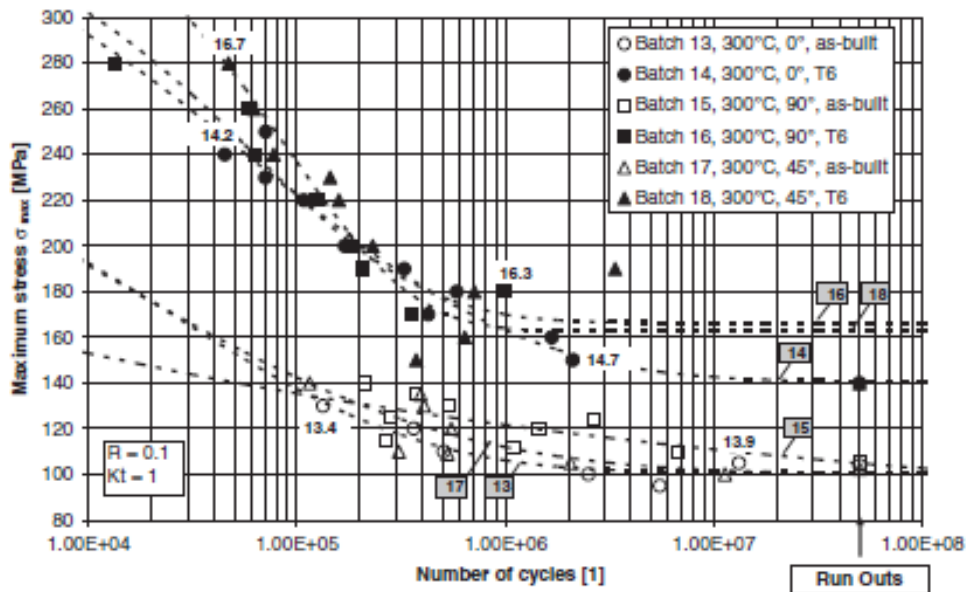
Fig.1.34: Fatigue resistance and Weibull distribution (50% probability of failure) of batches that are built at 300 °C platform temperature (E. Brandl, 2012).
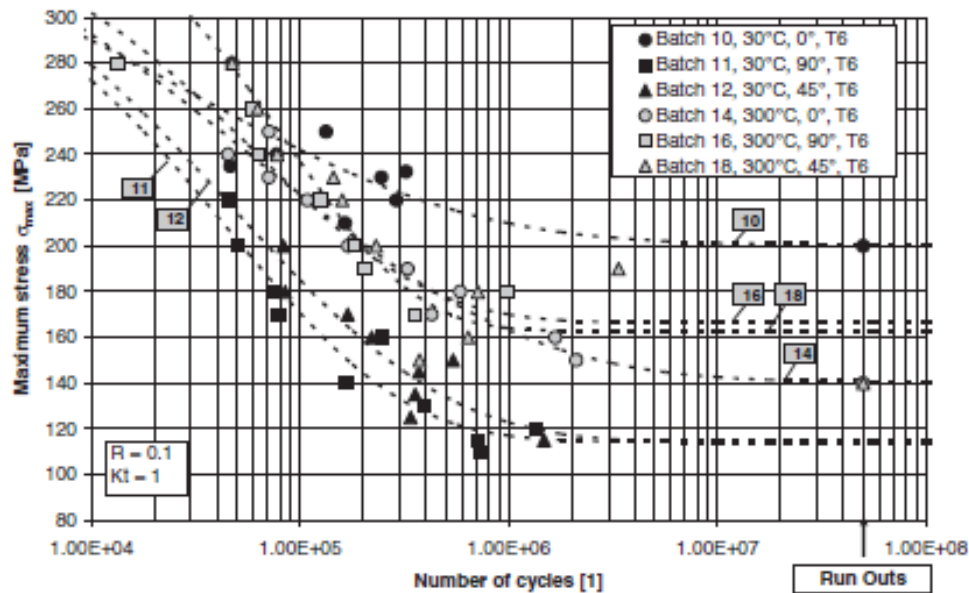
Fig.1.35: Fatigue resistance and Weibull distribution (50% probability of failure) of batches that are peak-hardened (PH) (E. Brandl, 2012).

The tensile test have highlighted that the building orientation with which the sample is built, did not influence the tensile properties of the fabricated part; this consideration is in accordance with that of K. Kempana *et al.* (2012), in which different mechanical properties were analyzed on AlSi10Mg fabricated parts with different building orientation.

The heating of the powder bed reduces the amount of the metallurgical defects because of the reduction of the thermal gradient and hence the cooling rate is reduced. The final effect is a global reduction of the thermal distortion since fewer stresses are developed. As concern the crack initiation the analysis of the fracture behavior of the laser melting parts shows that the crack always starts in correspondence of the imperfections on the top surface or at the substrate. This is due to the localized stress conditions and the plastic deformations induced by the surface discontinuities, where the notch effect promotes crack formation (Ammar HR, 2008, Qian G, 2011).

(A)   (B)
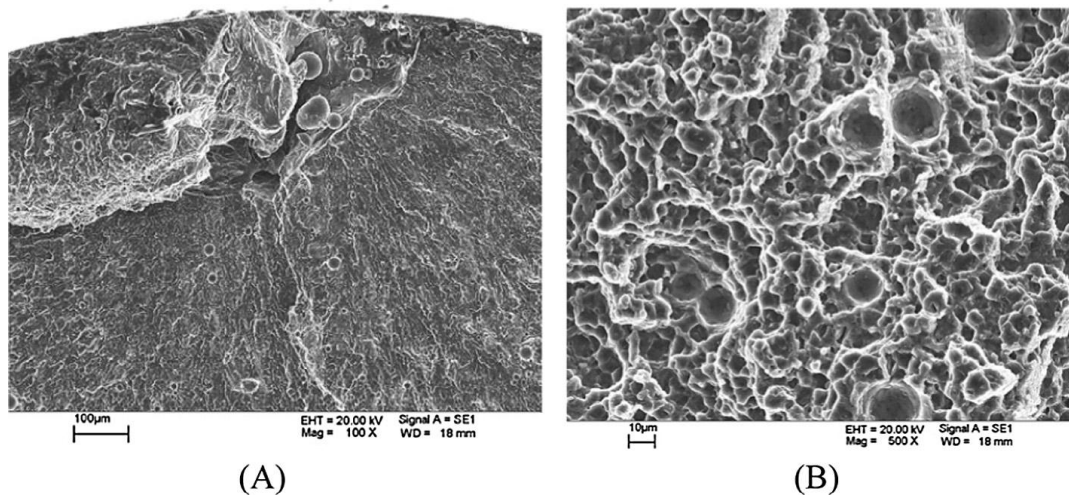
Fig.1.36: typical fracture surfaces of SLM processed AlSi10Mg parts (powder bed temperature of 300°C): (A) crack initiation site and (B) area of forced fracture (Brandl E, 2012).

1.5.3) Hardness and wear resistance

The hardness is another mechanical properties strongly dependent by the process at which the alloy is submitted. While in the cast parts the high hardness and strength is reached during the heat treatment (after process) by the formation of **Mg2Si** precipitates, in SLM parts, significantly higher hardness and strengths are already reached in the as-built state, i.e. non heat treated condition (K. Kempena, 2012). These result from the very fine microstructure and fine distribution of the Si phase in AlSi10Mg SLM parts due the rapid cooling and solidification, and probably also from the presence of **Mg2Si** although those precipitates were not observed by XRD analysis made by K. Kempena *et al.* (2012). The remarkably fine microstructure consisting of small Al-matrix cells/dendrites decorated with Si phase is shown in Fig.1.37.
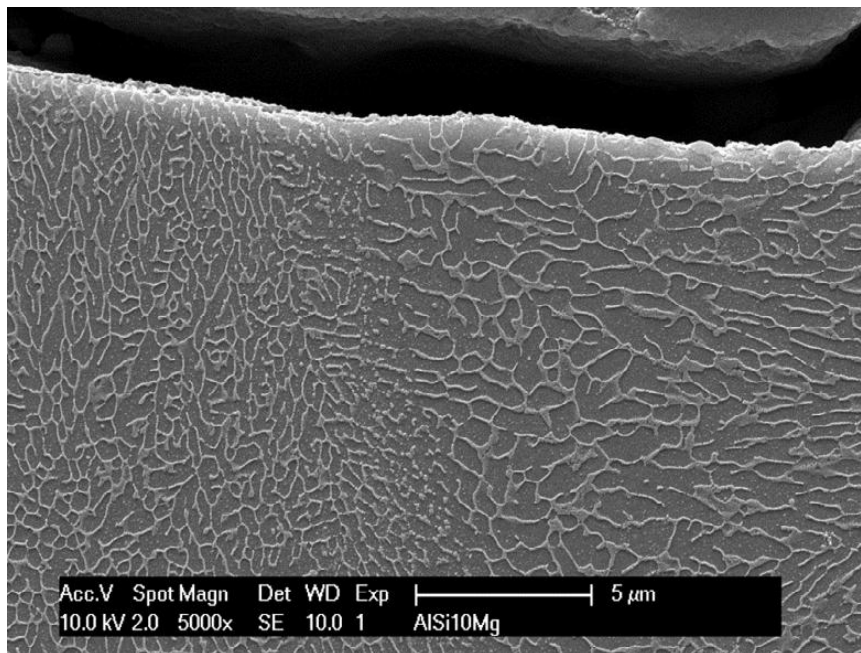
Fig 1.37: SEM micrograph of a AlSi10Mg SLM part showing the Al-matrix cells decorated with Si phase. A cross section perpendicular to the layers and the scanning direction is shown here, (K. Kempena, 2012).

As we can see in Fig.1.38(A), in which it was been analyzed the relationship between the hardness and the scanning velocity of laser melting processed aluminum part, there is not a direct correlation between these two parameters. However, in a second time, it has been demonstrated that the increasing the scanning velocity also the hardness was increased (Buchbinder D, 2008-2012). The Fig.1.38(B) shows variation of the hardness by varying the scan spacing in a SLM processed aluminum part. Also in this case, it is obvious the independency of the hardness with respect the scan spacing, however the optimum value of hardness (148 $HV_{0.1}$) was reached at a scan spacing of 0.15 mm.
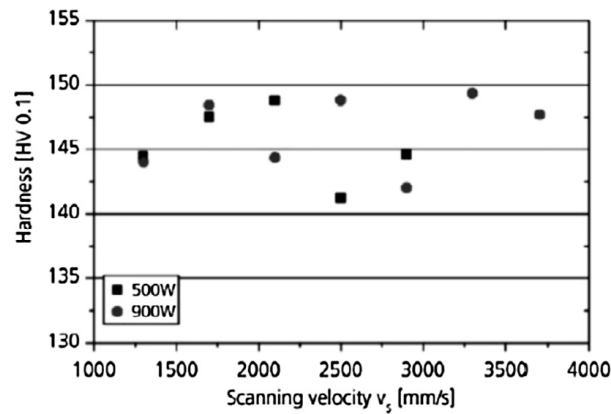
(A)
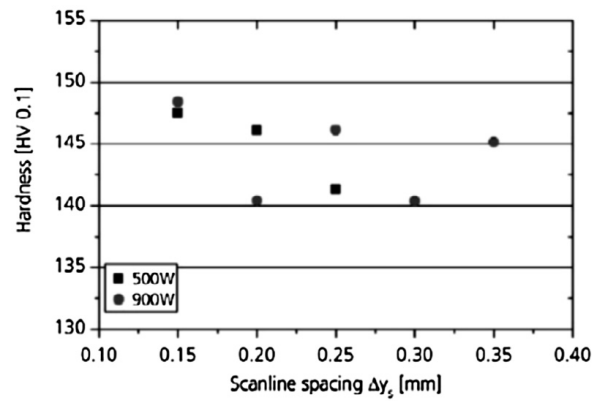
(B)

Fig.1.38: Hardness of SLM processed AlSi10Mg samples depending on (A) scan rate and (B) scan spacing (Buchbinder D, 2012).

Residual stresses are not always disadvantageous in laser melting fabricated parts because they provide a high sufficiently high densification without the formation of cracks of pores enhancing the part's hardness (E.O. Olakanmi, 2015). Moreover, the rapid solidification imposed by the powder bed laser melting process results in a grain refinement of the microstructure that could be attributed to the increased hardness of the laser melting fabricated part. Consequently, this lower the parts co-efficient of friction (COF), thereby improving the wear resistance of the parts.

1.6) Critical issues of the laser melting process

Considering that the component is made by an ensemble of layers, each of which is overlapped and melted to the previous one, and scanning tracks, the final properties of the part will depend on the quality of the single layer and of the single scanning track. As concern the studies about the melting of the single scanning track of powder conduced by Yadroitsev (2010), they have shown that, altough in general the reduction of the scanning velocity causes an increasing of the transferred energy to the powder bed ensuring the complete melting and better densification results; an excessive exposition time may result in a reduction of the process quality through the phenomenon of the denudation of the substrate. Imposing low scanning velocity and high exposition time progressively lead to transfer of thenergy from the current scanning track to the adjacent one, which partially melt and will tend to growth (coalescence phenomenon) and solidify in the form of small drops (Fig.1.39).
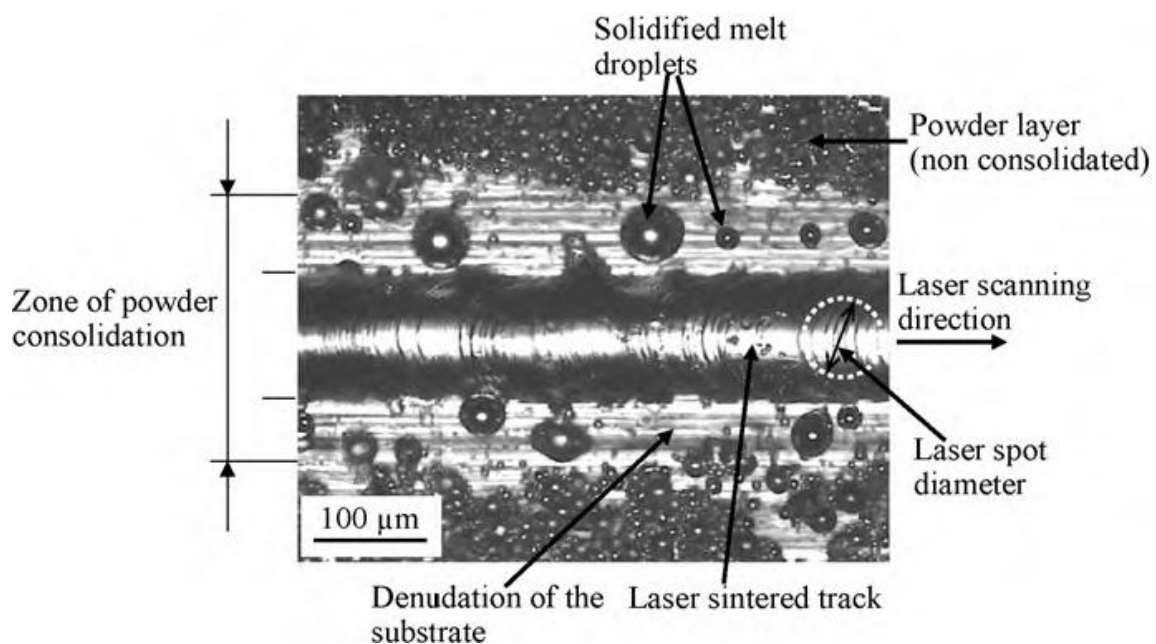
Fig.1.39: Top view of a laser sintered track from stainless steel grade 316L (−25 µm) powder on steel substrate. Laser power is 50 W,scanning speed is 0.10 m/s, thickness of the deposited powder layer is 40 µm.

In this way, when the laser will scan the adjacent track, it will not meet a uniform powder bed, but the bare substrate, partially covered by a series of metal drops already melted and solidified. This phenomenon can cause residual porosity in the products components, and its amount may vary with the type of processed metal. When working with metal alloys characterized by a higher thermal conductivity, the heat supplied by the laser will tend to be removed more rapidly, from the molten pool to the surrounding powder, making most marked phenomenon of denudation. Especially in these cases, the use of excessive laser exposure times can result counterproductive and not useful, and may result to be a more effective approach to employ a higher laser power for the lower exposure times.

1.6.1) Mechanisms of thermal stresses

Thermal stresses are stresses induced in a body when some or all of its volume is not free to expand or contract in response to changes in temperature. A material in its liquid phase does not contain thermal stresses. In the SLM process, thermal stresses arise in solidified material, subjected to temperature gradients, or subjected to shrinkage caused by the solidification of adjacent laser melted material. Using short scan vectors and preheating of the base plate can be a solution for this problem that can introduce part deformation, cracks or an undesired reduction of strength (Kruth *et al*., 2012). For cases where no extra material is deposited, residual stresses arise by non-uniform plastic deformations in solid material. In that case, as long as the thermal stresses are elastic, no residual stresses will remain when the temperature comes back to its original value. If the thermal stresses inside a material become higher than the yield stress, residual stresses will remain after cooling.

Mercelis (Mercelis P., 2007) uses two descriptive models to explain the mechanism of the thermal stresses in SLM: the temperature gradient mechanism (TGM) model and the cool-down phase model. The TGM model states that the laser beam heats up solid material being irradiated during the SLM process, which, as a result, tends to expand as shown in Fig1.40(a). The thermal expansion (eth) is partially inhibited by the surrounding colder material, yielding a compressive stress–strain condition in the irradiated zone. If the compressive stress exceeds the compressive yield stress (syield) of the material, the compressive strain will be partially elastic and partially plastic as illustrated in Fig.1.40(b). After the laser beam leaves that area, the irradiated zone will cool and tends to shrink. The shrinkage is partially inhibited as a consequence of the plastic deformation developed during heating, yielding a residual tensile stress condition at the irradiated zone. According to the equilibriums of force and momentum of the part, the irradiated zone will become surrounded by a zone of compressive stress. The cool-down phase

model describes the formation of residual stress as it arises in previously melted material when it re-solidifies and shrinks in solid state. The shrinkage is partially inhibited by the underlying material, thus introducing tensile stresses in the added top layer.
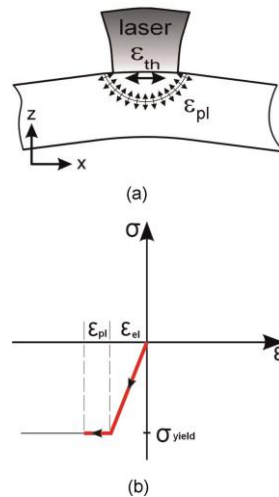
Fig.1.40: (a) Induced stresses and deformation (strain) during laser beam heating. (b) Simplified representation of the formation of thermal stress and strains in the irradiated zone.
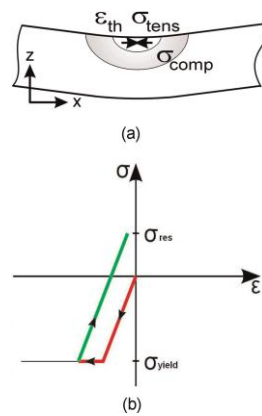
Fig.1.41: (a) Occurring stresses and deformation (strain) when the part cools down.(b) Simplified representation of the formation of residual stresses and strain in the irradiated zone.

The problem of the thermal stresses can be overcome by optimal choice of the orientation of scan vectors and hence choosing the most appropriate scanning strategy. If the area to be scanned is small (Kruth J-P, 2004), a short scan length occurs and the surface has little time to cool before the next track is scanned, thus resulting in high temperature. For larger areas, the scanned tracks have more time to cool down resulting in a lower temperature over the scanned area. The lower temperature results in poor wetting conditions in the scanned material hence its density is reduced because of larger heat dissipation between loose powder and the solidified material.

1.6.2) Influence of the scanning strategy

The scanning strategy is the order with which the laser proceeds when melting the tracks that constitute each single layer of the component. One of the standard strategies for the production of components for the SLM is shown in Fig.1.42, and it is composed by the following steps:

1. It is drawn the outline of the layer;

2. Redraws the outline and the inside area is covered with parallel scan traces the x axis;

3. It is drawn the outline of the new layer;

4. Redraws the outline and the inside area is covered with parallel scan traces y axis.
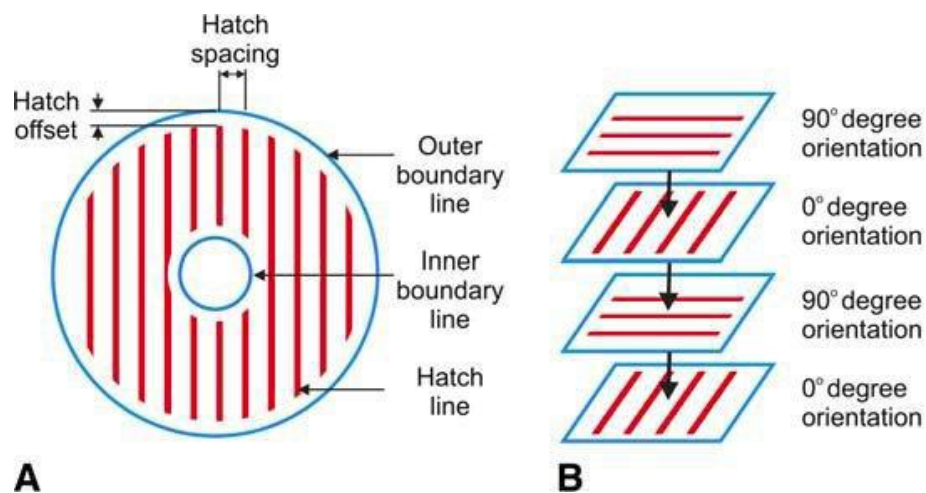
Fig.1.42: Graphic representation of the most simple scanning strategy used in the laser melting process; (A) the section on *x-y* plane and (B) scanning rotation along *z* direction (Stamp *et al.*, 2009).

The scans of the contours are separated by a certain distance (offset hatch) from the central scan lines, to compensate the fact that the energy in the peripheral areas supplied by the laser, being unable to spread at 360 ° in the surrounding material, spreads with a greater depth to the inner areas. The double contour fusion is performed because it allows to obtain a better surface finish. The alternation of the scanning direction of 90 ° at each layer is one of the simplest expedients adopted to reduce the residual stresses and distortions of the components.

In the standard mode of the process, the layers of the components are realized by performing parallel scanning lines between them and of length equal to the entire extension of the section of the piece in that direction. When the area to be covered is small, the scan traces will tend to be short; therefore adjacent tracks will be melted rapidly one after the other, leaving elapse short intervals of time for the cooling of the material and resulting in a total process temperature quite high. For larger areas, the path followed by the laser beam for each scanning track will be longer, and the previously melted areas will have a larger time interval to cool before the melting of the next track undergoes them to a further heating again. This results in a lower average temperature of the surrounding area to the laser beam spot diameter, which will cause higher thermal gradients.

Since the scanning strategy can strongly affect the dynamics with which the different areas of a layer are subjected to different thermal gradients, and therefore on the presence of deformations and cracks in the products components, various studies have been devoted to develop scan strategies able to minimize the defects in the material during the laser melting process.

In order to test the effects of the phenomena described above, different laser scanning patterns to minimize the porosity inside AlSi10Mg parts via laser melting were considered by Aboulkhair (Aboulkhair NT, 2014). X (a unidirectional scan with a single scan per layer), 2X(this is also unidirectional but each layer is scanned twice), alternating (in which each layer is scanned with a direction rotated by 90° with respect its precursor), X&Y2HS (each layer is scanned twice having each scan perpendicular to the one before and with different hatch spacing for each scan), pre-sinter (the first layer is scanned with half the powder while the second one with the full power), and the overlap (each layer was scanned twice with the second scan that causes the overlap between the two adjacent molten pools). Considering the AlSi10Mg alloy and using a scanning speed of 500 mm/s, scanning each layer twice it is possible to reduce the keyhole pores, which still exist when the layer is scanned once or in alternating scan. In the double scan per layer techniques (2X, X&Y2HS, pre-sinter, or overlap), the keyhole pores were reduced but not completely eliminated at all scanning speed.

In the work of Kruth et al. (2004) were melted monolayers thick dust 150 μm using different scanning strategies. The residual stress generated in the obtained metal sheets were evaluated by measuring their curvature in the x and y directions. The different strategies are shown in Fig.1.43. The first two, (1) and (2), characterized by parallel tracks and long as the whole of the layer extension respectively in the directions *x* and *y*, are the simplest employable in laser melting processes. In the other four strategies, the component of the surface has been divided into sectors square of 5 mm x 5 mm, respectively for strategies (3) and (4) and a 2.5 mm x 2.5 mm for the strategies (5) and (6). The order in which these areas have been processed was for consecutive sectors in the components (3) and (5), while in the components (4) and (6) was randomized in order to be processed every time the sector that had suffered the lower heat influence (Least heat influence or LHI) from the melting of the previous sector. For all four strategies for which the scanning division in sectors has been occurred, the direction of the scan lines was alternating 90 ° between successive sectors.

The scanning with continuous tracks along the *x* direction (1) has given rise to the greater degree of curvature of the component in the same direction, but the lesser curvature in the *y* direction; it was found the opposite condition for scanning in the *y* direction (2). The division into sectors of the area to be processed in the operated from (3) strategies to (6) has been shown to cause less deformation in the monolayer, where they are observed very small curvatures in both the *x* and *y* direction. However, it was not found a noticeable difference by varying the size of the sector. Among the four strategies in sectors, the (3) and (5) have proven to cause minor deformations, probably due to the onset of thermal gradients minor compared to strategies dictated by the LHI. In fact, proceeding with the fusion to the adjacent sectors, the temperature difference between the melting zone and the surrounding area tends to be lower on average due to the preheating caused by the scanning of the previous sectors.
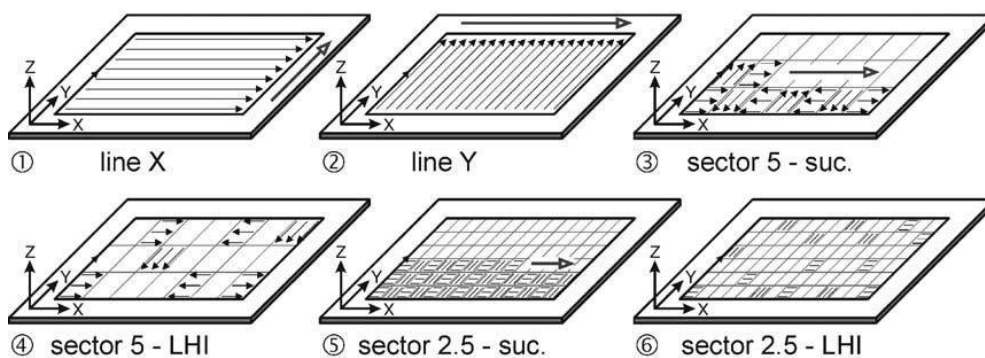
Fig.1.43: Six different scanning strategies to assess how to minimize the tensions and residual deformations on a single-layer component made by SLM (Kruth et al., 2004).

Kruth *et al.* at first have demonstrated that by reducing drastically the length of the scanning vectors, it is possible to reduce thermal distortion.
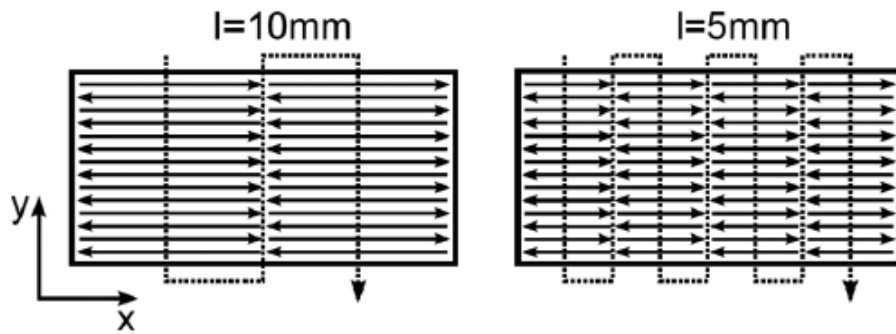
Fig.1.44: Scanning strategies adopted to assess the influence of the length of the scanning vectors on residual stresses in manufactured components for SLM (Kruth et al., 2012).

Secondly, they have evaluated the influence of the scanning track orientation by varying the angle β between them and the *x* axis in the range of 0° and 90°. As found in other publications, the direction along which the scanning traces are realized is that subject to greater thermal tensions and to further deformations. Increasing the angle β leads to a reduction of the thermal distortion inside the component, reducing the deflection of the part along the *x* direction (maximum reduction of the deflection of 59% for an orientation of the scanning trace of 90° with respect to the *x* axis).
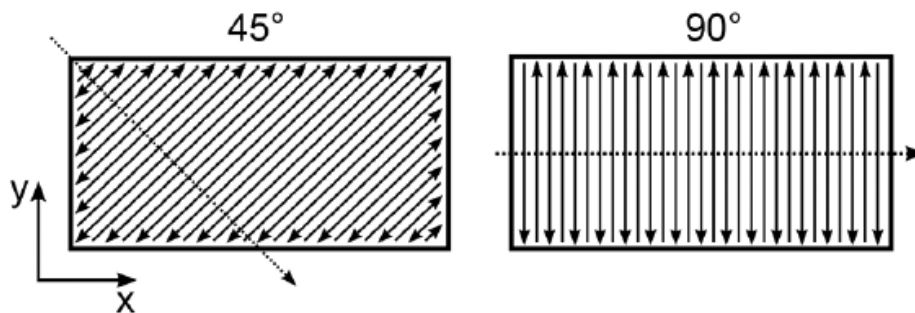
Fig.1.45: Scanning strategies adopted to assess the influence of the orientation of scanning vectors on residual stresses in manufactured components for SLM (Kruth et al., 2012).

In the work of Jhabvala et al. (2010), four different strategies have been tried to scan, to evaluate their influence on the temperature gradient and the quality of components products by using the laser melting technology. The first strategy of parallel scans (Fig.1.46a), the second of the spiral scans (Fig.1.46b), the third (Fig.1.46c) is the so-called paintbrush scanning and the fourth is the chessboard scanning (Fig.1.46d). The scanning parallel tracks is the simplest strategy, but has confirmed to cause large temperature gradients and large residual stresses along the entire the square surface to melt. The spiral scan, to scan speed sufficiently high, it has been shown to lead to very strong bonds between the different layers; However, for powders with a low thermal conductivity, this strategy does not allow to heat to be dissipated fast enough leading to the balling and cracks formation in the component. The scan paintbrush is similar to that in parallel scans, but is characterized by shorter scan tracks; it has shown that it is possible to generate lower thermal gradients obtaining components with high density and accuracy (also by using powder with low or high thermal conductivity). However, it was found that the links between two subsequent layers are not always perfect, and that this strategy can cause problems of delamination. The chessboard strategy expects the subdivision of the area to be consolidated in small square areas, which they are scanned with parallel lines oriented alternately, from one sector to the subsequent one, in two orthogonal directions; by this technique it is possible to reduce thermal inhomogeneities ensuring good product quality of the components.
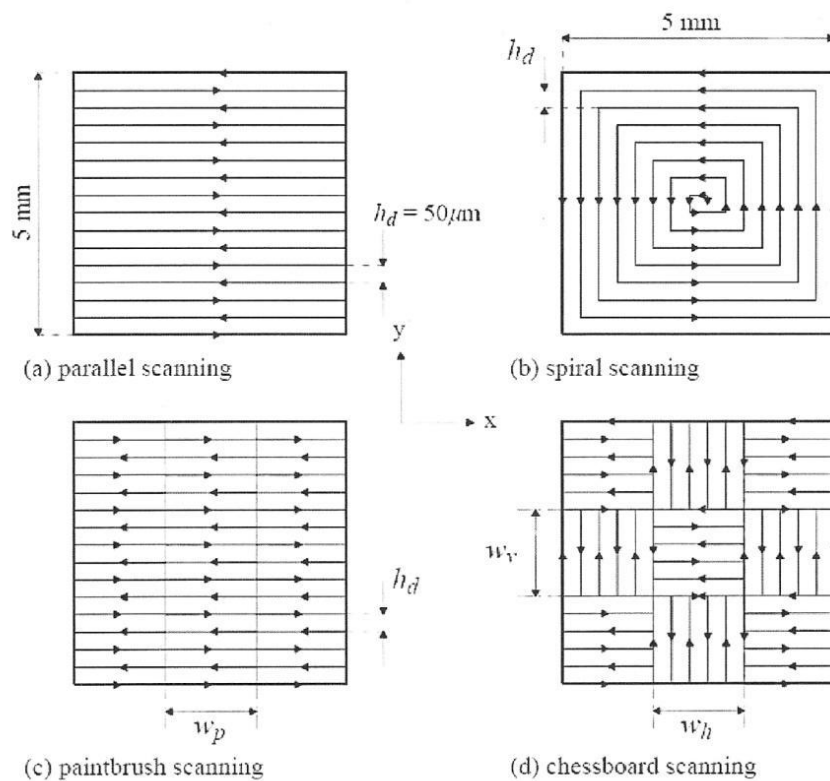
Fig.1.46: Four different scanning strategies to test their influence on the quality of the components produced by laser melting (Jhabvala et al., 2010).

Recently, strategies have also been developed, which provide the rotation of the direction of the scan lines other than 90 °, for example the variation at each layer of 60 ° or 45 ° . Such solutions allow to obtain components with more isotropic properties having lower states of tension due to the partial mutual compensation of the tensions of the individual layers oriented layer by layer in directions always different (Thijs et al., 2013).

1.7) The supports design and support structure

The laser melting process can be used to produce fully dense parts with mechanical properties equivalent or even superior to those of parts produced by the conventional manufacturing. However this process requires the presence of external support structures during the construction of the part (F. Calignano, 2014). These structures are necessary to fix the part to the building platform, conduct heat away from the part and to prevent the distortion and/or the collapse. This can happen when the amount of overhang exceeds a certain threshold value. The presence of support structure increases both the production time and the post-processing time due to its complexity which is increased. Minimizing the amount of supported surface can improve the process efficiency. This is the reason why the geometrical design and optimization of the support structures play an important role in the production efficiency of the metallic parts produced by laser melting. In order to reduce the amount supports the more effective way is to determine the optimal building position. Changing the built orientation it changes the support structures and the build time, which is estimated by roughly slicing the part. In order to chose the best orientation, the designer has to determine the overhanging structures, which are a part of the component that is not supported during the building, by the solidified material or a substrate on the bottom side (see Fig.1.47). The molten pool created by the heat input from the laser is supported by the powder material. In any building orientation, the part is defined with its base on the x-y plane and the building direction is along the z axis.

A support structure may be decomposed into two functional areas: teeth, connections between the main support structure and part thus minimizing the contact area, and the main support structure. The main function of the teeth is make easier the part removal when the process is completed. The teeth distance need to be choose considering the part removal and the heat distribution in order to prevent the part deformation in particular, teeth too close imply greater difficulty in removal of the part while teeth too close can lead to a greater deformation of the part.
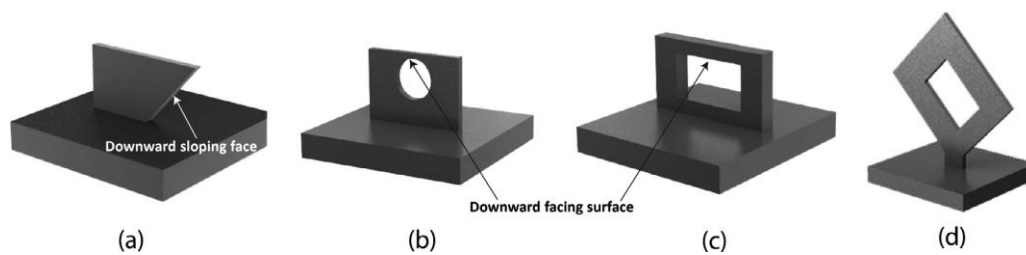
Fig.1.47: Example of overhanging structures: (a) downward sloping face, (b) and (c) downward facing surfaces and (d) downward sloping faces obtained by orientation in the building platform. (www.renishaw.com/additive).

In the support design phase, the walls angle evaluation is fundamental to guarantee a proper heat distribution inside the part. There exist a self-supporting angle used to control the creation of supports on angled walls and surfaces. The results of some experiments have shown that the downward sloping face oriented at 45° leads to a curl formation which is not significant enough to obstruct the build efficiency. Part can be built without supports at angles up to 30° in AlSi10Mg part but the samples have high surface roughness. Regarding to the concave radii, in the top of the radius, the tangent decreases to 0° as the part grows in the z-axis. It was identified that as the tangent angle α increases, the warping distortion decreases and the accuracy of the curve was improved.
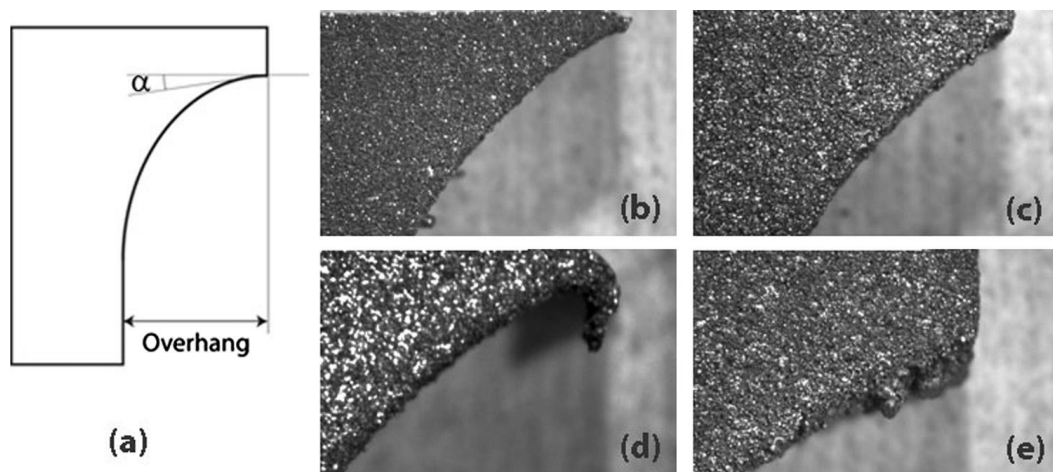
Fig.1.48: (a) Concave radii. Titanium: (b) overhang of 9 mm, (d) overhang of 15 mm. Aluminum: (c) overhang of 9 mm, (e) overhang of 15 mm.

As regard the convex radius, it is vulnerable to warp. Outcomes of (F. Calignano, 2014) have shown that the accuracy of the radii in the aluminum part is poor and the radius did not respect the original CAD data for tangent angle β lower than 40°. In following pictures, it is possible to observe some parts produced by the Renishaw S.p.a. (www.resources.renishaw.com), in which it is possible to distinguish the support from the rest of the part, in particular in Fig.1.49 it is shown a group of exhaust manifolds supported on the build plate and the exhaust manifold after the removal.
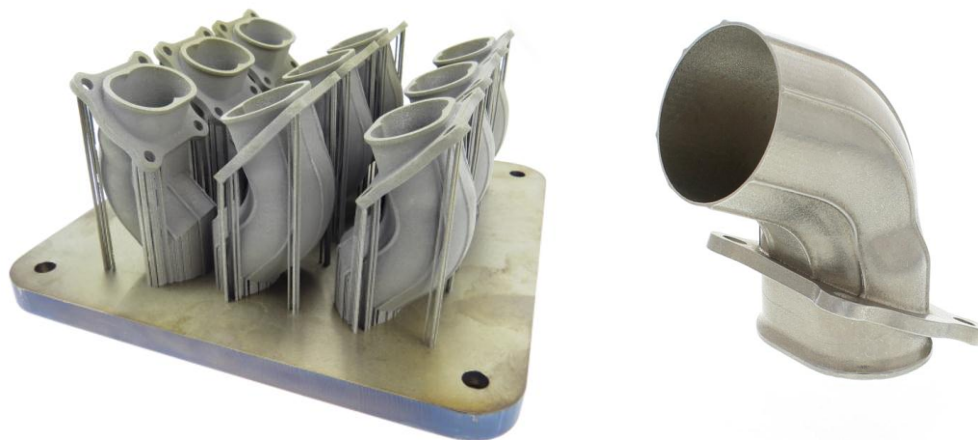
Fig.1.49: On the left exhaust manifolds on build plate with supports in nickel alloy, on the right exhaust manifold without supports in nickel alloy.

The main drawback in the production of parts with overhanging zones is shown in Fig.1.50 and Fig.1.51. When the laser irradiates solid-supported zones (region a), the heat conduction rate is high, instead when the laser irradiates the powder-supported zones (region b) the heat conduction rate is much lower than the solid-supported zone. This situation is typical of the overhanging surface fabrication where the absorbed energy input will be much higher when the laser irradiates the powder-supported zones, causing the enlargement of the molten pool and the lowering of the part accuracy. Another effect caused by the thermal stresses is the warping defect in which the rapid solidification during the laser melting process leads to a plastic deformation, in particular when the thermal stresses exceeds the strength of the material. The lacking of supports of an overhanging surface enhance this effect.
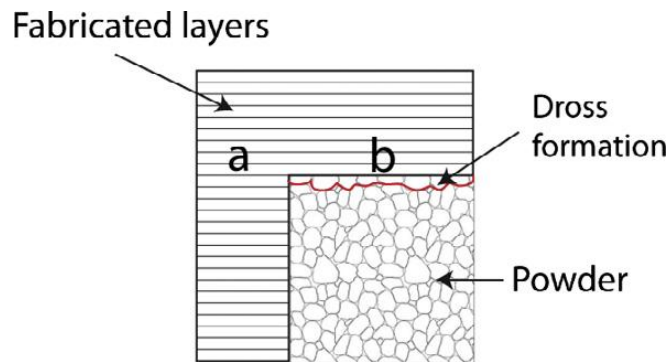
Fig.1.50: Dross formation on overhanging surface.
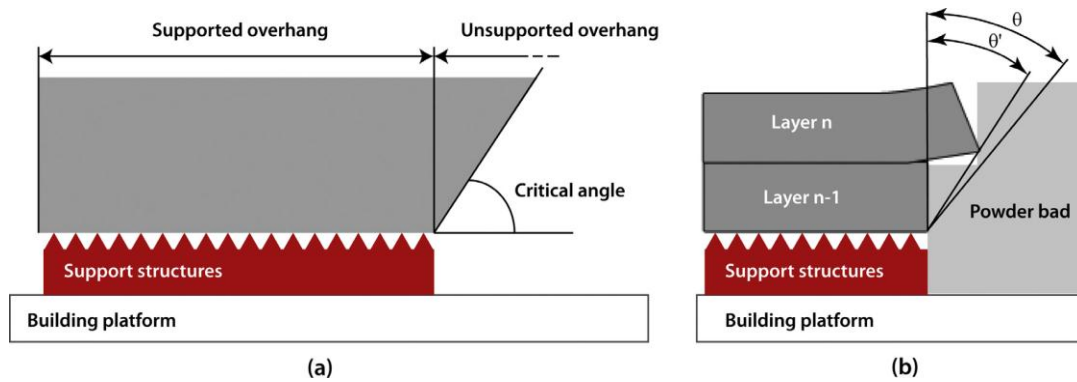
Fig 1.51:a) example of supported and unsupported overhang structures and (b) warping principle in the unsupported structure: the effective inclined angle *θ'* between the overhanging part of the layer under consideration and the previous layer was smaller than the designed inclined angle *θ*.

Chapter 2

Goals Of The Work

The selective laser beam melting process is a technology in expansion, in which the final product requirements are changing. This type of technology is passing from the prototype production, production in medical and dental fields, to a production including sectors such as the specialized automotive, aviation and the powder generation ones. The main difference is that, while in the past the technology had to meet a certain type of requirements concerning just the components compliance in terms of geometry and surface finish quality, nowadays it has to be able to satisfy a larger number of requirements such as the metallurgical and mechanical ones, that are more difficult to reach. For this reason, a deeper known of the materials application in the power bed laser melting is fundamental for the continuous improvement and expansion of the technology itself, and this is the starting point of my thesis.

The AlSi10Mg alloy, under the form of powder, is a commercially available material that suffers some difficulties in its laser processing because of the high reflectivity coefficient. However, this is an alloy widely spread in several industrial applications, so its use is relevant for producing components.

In this contest the main purpose of the thesis concerns the experimental characterization of samples produced via powder bed laser beam melting process, on commercially available Aluminum-Silicon-Magnesium alloy.

The investigated process parameters, such as laser power, interaction time and build plate temperature, on the AlSi10Mg powder on density, microstructure, calorimetric and mechanical properties were investigated.

The fabricated samples were characterized through density measurements, thermal and SEM analysis and hardness tests. Also XRD analysis were performed.

Chapter 3

Experimental

In this chapter the materials, the equipment used for the sample fabrication and material characterization and the methodology adopted for the analysis of the results are reported.

3.1) The AlSi10Mg powder characteristics

The aluminum powder uses in this work is the AlSi10Mg-0403 alloy, in which the aluminum alloyed with silicon of mass fraction up to 10% and small quantities of magnesium and iron, along with other minor elements, are present. The presence of silicon makes the alloy both harder and stronger than pure aluminum due to the formation of Mg_2Si precipitate. Due to the natural formation of an oxide layer on the surface of the aluminum alloy, the material has high corrosion resistance which can be further improved by chemically anodizing.

The following properties characterize the material:

- Low density (good for light weight components);

- High specific strength (strength to mass ratio);

- High thermal conductivity;

- Very high electrical conductivity;

- Responds well to post process finishing;

The fields of application of this type of material vary from the automotive to the aerospace and defense, to the production of electronics cooling and consumer goods. The Tab.3.1 represents the generic data of the AlSi10Mg (wrought material) while in Tab.3.2 the mechanical properties of additively manufacturing components are presented (www.renishaw.com/additive).

Tab.3.1: Generic data of AlSi10Mg – wrought material.

Density	2.68 g/cm^3
Thermal conductivity	130 W/mK to 190 W/mK
Melting range	570 °C to 590 °C
Coefficient of thermal expansion	20 μm/mK to 21 μm/mK

Tab.3.2: Mechanical properties of additively manufactured components.

	As Built	Stress relieved (see note 2)
Tensile strength (see note 3)		
Horizontal direction (XY)	442 MPa ± 6 MPa	334 MPa ± 1 MPa
Vertical direction (Z)	417 MPa ± 27 Mpa	339 MPa ± 6 MPa
Yield strength (see note 3)		
Horizontal direction (XY)	264 MPa ± 2 MPa	211 MPa ± 2 MPa
Vertical direction (Z)	206 MPa ± 6MPa	174 MPa ± 4 MPa
Elongation at break (see note 3)		
Horizontal direction (XY)	9% ± 1%	9% ± 2%
Vertical direction (Z)	6% ± 2%	4% ± 1%
Modulus of elestacity (see note 3)		
Horizontal direction (XY)	71 GPa ±5 GPa	71 GPa ± 2 GPa
Vertical direction (Z)	68 GPa ±2 GPa	66 GPa ± 3 GPa
Hardness (Vickers)(see note 3)		
Horizontal direction (XY)	119 HV0.5 ± 5 HV0.5	103 HV0.5 ± 5 HV0.5
Vertical direction (Z)	123 HV0.5 ± 2 HV0.5	98 HV0.5 ± 5 HV0.5
Surface roughness (R_a) (see note 3)		
Horizontal direction (XY)	5 μm to 9 μm	
Vertical direction (Z)	7 μm to 9 μm	

Note.1 In the range of 20 °C to 100 °C.

Note.2 Stress relieved at 300 °C ±10 °C for 2 hr, air cooled.

Note.3 Tested at ambient temperature by Nadcap and UKAS accredited independent laboratory.
    Test ASTM E8.Machined before testing.

Note.4 Tested to ASTM E384-11, after polishing.

Note.5 Tested to JIS B 0601-2001 (ISO 97). As built after bead blasting.

The AlSi10Mg powder used is a gas atomized powder and the particles are nominally spherical in shape and their diameter ranges from 20 µm to 63 µm (see Fig.3.1). Particular care should be taken with fine aluminum alloy powder due to the potential itself combustion combined with the risk of explosive hydrogen gas being liberated on contact with water, acid or alkalis. The following table is provided by Renishaw S.p.A. and it represents the powder composition followed by the Gaussian distribution of the powder size.

Tab.3.3: Powder composition.

Powder composition / percent by mass												
Al	**Si**	**Mg**	**Fe**	**N**	**O**	**Ti**	**Zn**	**Mn**	**Ni**	**Cu**	**Pb**	**Sn**
Balance	9.0 to 11.0	0.25 to 0.45	<0.25	<0.2	<0.2	<0.15	<0.1	<0.1	<0.05	<0.05	<0.02	<0.02
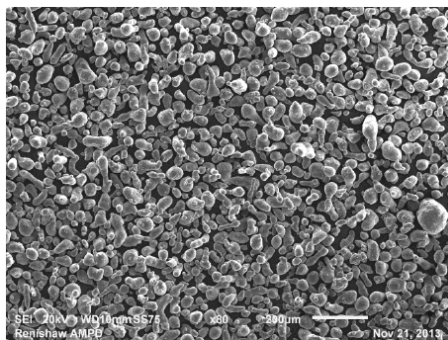
D10	26 µm to 30 µm
D50	40 µm to 50 µm
D90	68 µm to 72 µm
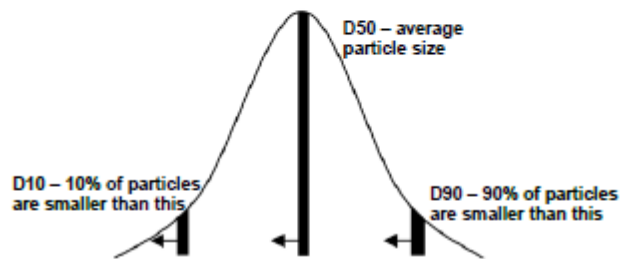
Fig.3.1: SEM image of the powder at 80x magnification with the particle size distribution analyzed by laser diffraction.

3.2) The selective laser beam melting system

The system used in this work is *AM250* from Renishw (see Fig.3.1) which is technology based on the laser melting of the metallic powder. It gives the possibility to develop 3D component having any type of geometry by reducing the weight and, at the same time, keeping high the mechanical and functional properties.

Fig.3.2: Renishaw *AM250* used to fabricate the samples.

The laser melting process of the metallic powder takes place inside the process chamber, which is the core of the machine. In the center of the process chamber there is the build plate, which moves along the *z* axis thanks to an elevator, placed below. On the build plate, it is possible to assemble the metallic plates which is the growing substrate of the fabricated components. The working field of the machine is 25x25 cm on *x-y* plane and of about 36 cm along the *z* axis.

The metallic powder is charged in a tank placed in the rear of the machine and it is added to the process chamber (see Fig.3.3) thanks to a feeding system which provides the required amount. After the adduction of the powder inside the chamber, a wiper distributes in a uniform manner the powder on the build plate.
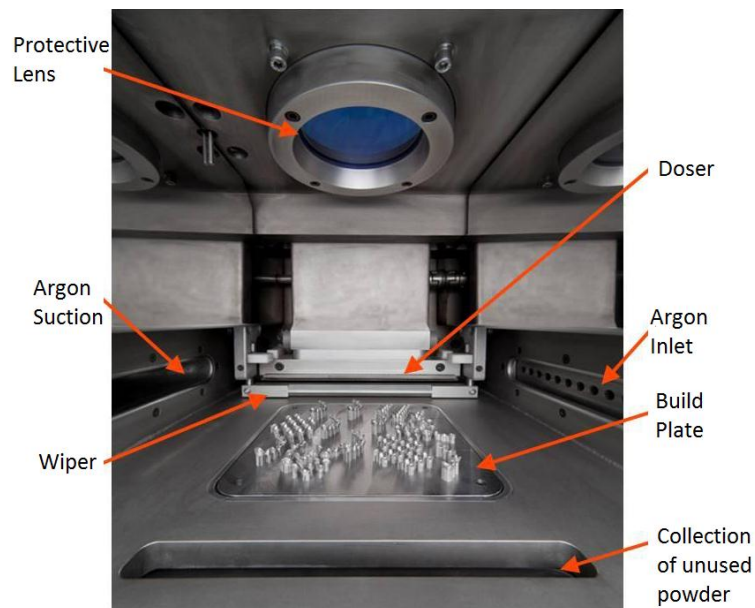
Fig.3.3: Process chamber of the AM250.

The laser used by the machine is a pulsed wave laser of ytterbium fiber with a maximum power of 400 W. The laser beam is directed by a mirror system able to position it with an error lower than 25 µm. It reaches the powder bed passing through a protective lens mounted with a sealing system capable of resisting the vacuum produced within the chamber during the initial phase of the process and to ensure that no contamination of the powder might be introduced in the area of the optical system.

The melting process occurs in presence of an inert atmosphere, constitute by Argon and inside a sealed chamber. This allows to create vacuum into the process chamber before starting the process. Once inside the chamber the relative pressure has reached the value of -964 mbar, with respect the atmospheric pressure, and the oxygen content is about 1300 ppm (0.13%), the vacuum pump stops and the chamber is subjected to a short washing with Argon until the required oxygen content is reached for the particular process, in any case lower then 1000 ppm (0,1%). After that the chamber is filled with Argon until the relative overpressure is 9-10 mbar respect to the atmospheric one, and only now the process can start.

Thanks to the sealed chamber it is possible to maintain the desired amount of oxygen inside the chamber during the entire process by adding Argon when it is required. It is also possible to guarantee contents of oxygen of about 200-300 ppm (0,02-0,03%) during the process, in the superior part of the chamber, and contents lower than 10 ppm (<0,001%) in the lower part, where the laser melting process of the powder bed takes place. These are the main differences of the AM250 from the other machines used for the laser melting, into which the oxygen is extract from the chamber through repeated washing operation with Argon fluxes and, in order to guarantee the lower oxygen content, the inert gas need to be added during the process. The reduction of the Argon consumption is one of the main advantages of the AM250 together with the lack of oxygen in the chamber, that is a significant characteristic when we are working with metal alloys that easily oxidize (for example Aluminum and Titanium).

During the melting process, the Argon atmosphere is made constantly recirculated through a pump located externally respect the process chamber. The gas enters the chamber through the intake pipes on the right wall and is sucked by a suction nozzle placed on the left wall (see Fig.3.4). The location and geometry of these openings has been conceived as a result of various fluid dynamic studies aimed at optimizing the gas flow ability to quickly remove the particulate particles that may arise during the melting process of the powders. Once extracted from the chamber and before being reintroduced by the thrust of the pump, the gas passes through a filter that retains the particulate removed by the gas stream.
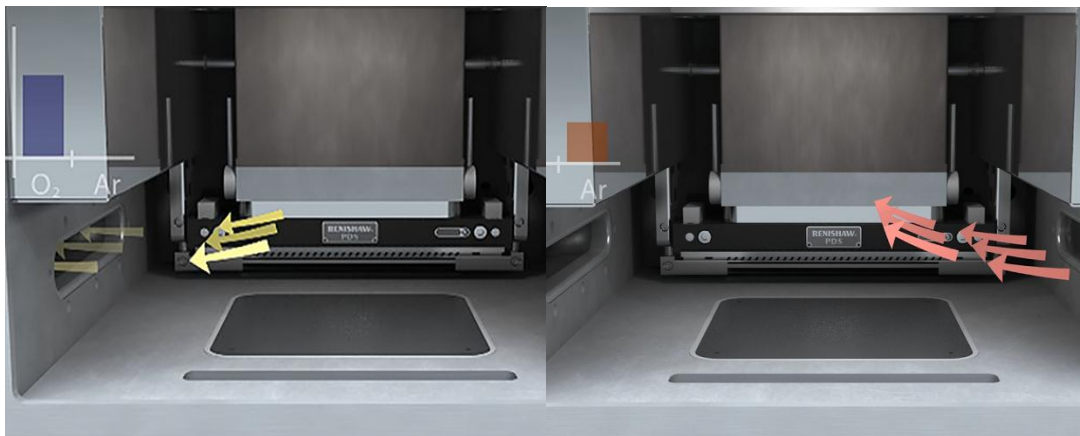
Fig.3.4: Argon recirculation. The Oxygen amount inside the chamber is reduced while the Argon amount is increased.

The powder alloy is charged in a tank (placed in the back of the machine) through some steel bottles having suitable safety valves in order to avoid possible loss of powder during the filling operation. Similar bottles are used to collect the powder that is not melted by the laser beam during the process, allowing the reuse of the powder after filtering in special sieving machine. Through this way it is possible to remove the inclusion produced during the melting process.
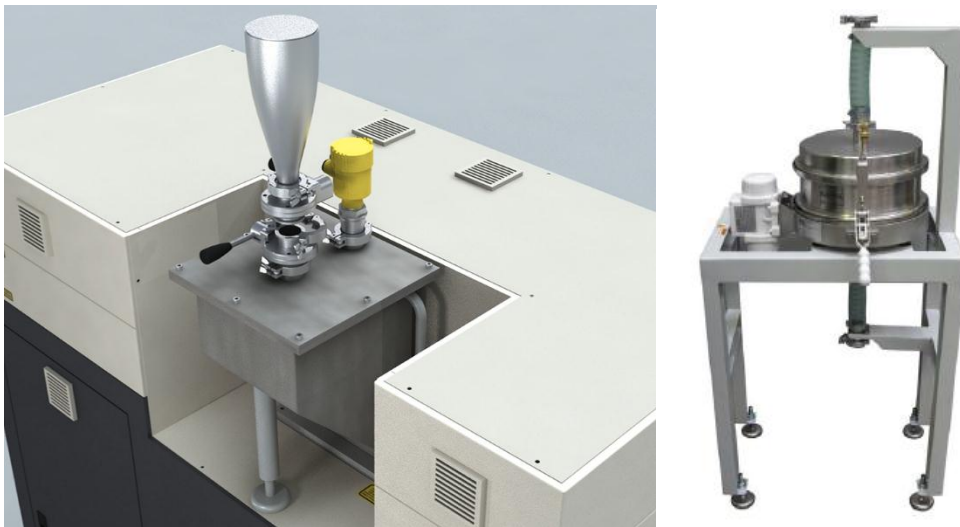
Fig.3.5: On the left, the reloading operation of the powder by using the steel bottle to stock the powder inside the tank placed in the back of the machine; on the right, the powder recovery system with mechanical action that allows the reuse of the powder.

Before the starting of the process, it is necessary to set all the process parameters and prepare the .MTT file to import in the machine. Renishaw performs the design phase using the Magics software developed by Materialise. This phase is divided into different parts:

1. Conversion of the CAD to .STL format;
2. Once the part is imported into Magics, the .STL File can be fixed to ensure there are no errors that would make the file an unsupportable file for the Build Processor (BP);
3. Part orientation considering different factor such as a good heat distribution and well supported zones;
4. Support generation in order to hold the part down to the substrate and also provide support to the part during build and transfer excess heat away from the build area;
5. After the support generation, the file is sent to the BP where the part is sliced and both process parameters and scanning strategy are chosen;
6. Then, the Build Processor generates the .MTT File that is the file format supported by the AM250 Software.

During the design of the process parameters, it is possible to interfere on different properties of the final component changing its final microstructural and mechanical characteristics. According to the final component requirement, it is possible to distinguish the zone where the laser operates the scan (see Fig.3.6), in particular there are:

- the filling parameters *(Fill Hatch)* related to the inner part of the piece, mainly responsible of the final component mechanical properties;
- the border parameters which are divided into: those referred to the outer edge (*Borders*) that help to improve the surface structure and the surface finish of the final component and those used to allow the Fill Hatch to be offset further from the edge of the part (*Additional Border*);

Fig.3.6: Definition of the three different scanning zones (*Borders, Additional Border* and *Fill Hatch*) of a square section on x-y plane.

Together with the choice of the optimal set of parameters, the scanning strategy have to be selected before the beginning of the process, remembering that the scanning strategy interferes on the length of the scan vector and hence on the heat distribution during the process. The *AM250* software gives the possibility to select different scanning strategies during the design phase, which are that represented in Fig.3.7.
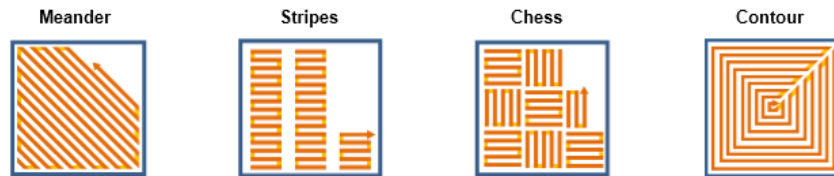
Fig.3.7: The different types of scanning strategies provided by Renishaw.

During the laser scanning, the laser operates by using point exposure instead of running continuously and each exposure creates a melt pool of metal which takes the form of a 3D Gaussian Curve. Each point is given a *x-y* co-ordinate position and have four pre-set parameters:

- Point Distance (mm), which is the distance between the centers of each successive melt pool (as a general rule the melt pools should be overlap by 1/3 to prevent the porosity);
- Exposure Time (µs), which is the length of time the laser will be on for each point;
- Power (W), that is the intensity of the laser beam;
- Focus (µm), that is where the parallel rays of light converge. The focal point is around 2mm long which gives a ±1 mm tolerance in which a focused spot can be achieved (for example setting this parameter to Z=0 will place the place the focal point on the datum line, that is the line corresponding to the top of the powder bed). This parameter gives the possibility to adjust the spot diameter by moving the beam by mm in Z direction (see Fig.3.8).
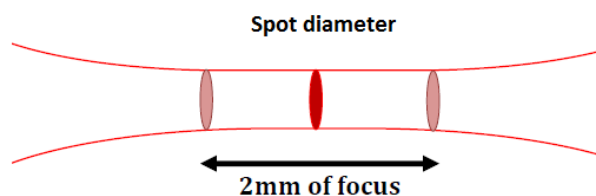
Fig.3.8: Caustic of the laser beam along the Z-axis.

- Hatch Distance (μm), that is the distance between each line vector of point exposures. The importance of this parameters is that it is directly correlated to the porosity, in fact by marking the hatch distance too large the porosity can occur between the hatch lines. As general rule the hatch distance need to be long enough to overlap the spots by about 1/3 (see Fig.3.9).
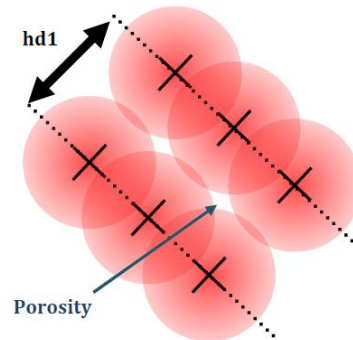
Fig.3.9: Schematic showing the interaction among the hatch distance and the porosity.

The *Renishaw AM250* gives also the possibility to heat the build plate before the starting of the process keeping constant its temperature during the whole process. The maximum build plate temperature achievable with this machine is 170°C. The preheating is performed through a soak cycle during which the machine heats the build plate, step by step at different heights along the *z* axis. By this way the chamber, into which the built plate runs, has the time to warm up and expand, preventing the locking of the dilated plate in the lower areas of the room.

3.2.1) Sample Fabrication

In my work, two types of samples were fabricated (see Fig.3.10): the first one, having cubic shape and the second one having a cylindrical shape. The dimension of the cubic sample is 7x7 mm having a pyramidal shape in the lower part to facilitate the removal process. The cylinder has a height of 15 mm and a diameter of 5 mm. For each plate 50 density blocks (two replies for each Power/Exposure time combination) and 25 cylinders have been fabricated.

Fig.3.10: Examples of blocks and cylinders produced.

It is also possible to see in Fig.3.11 how the process parameters have been varied on the build plate and how it was possible to pass from the design phase (.STL file Fig.3.11.a) to the sample fabrication (Fig.3.11.b).
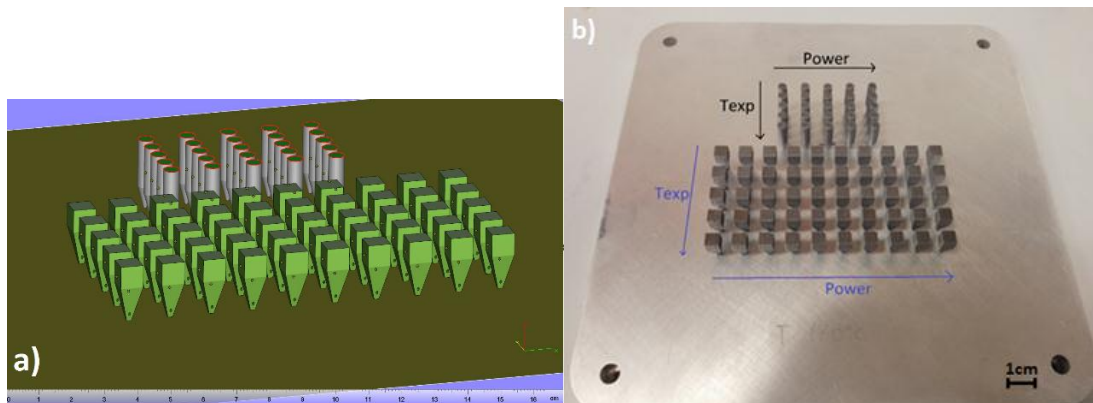
Fig.3.11: a).STL file of the build plate during the design phase; b) build plate after laser melting process and the directions along which the laser HATCHING parameters were varied: the Exposure Time was varied between different lines, and the Power among the columns.

3.2.2) Design of the experiments of the selective laser beam melting process

In order to investigate the feasibility areas of the selective laser beam melting process, it was decided to fabricate samples by varying different process parameters. Among the three different zones of the same scanning area (*Border*, *Additional Border* and *Fill Hatch*), it has been decided to focalize my study only on the effect of the variation of the *Fill Hatch* parameters, which are responsible of the resulting mechanical properties (being the scanning in the core region of the fabricated part). In addition to variation of the *Fill Hatch* parameters, also the Build Plate Temperature was changed.

By following the standard about the scanning strategy provided by Renishaw on this type of alloy, the adopted strategy was the MEANDER one. Each scanning section is rotated of 67° with respect the previous one and the scheme is repeated every 180 layers.

For all processes object of this study, the thickness of the layer of 25 μm, and the spot diameter of 130 μm were kept constant; also the *Border*, *Additional Border* together with the Point Distance and the Hatch distance of Fill Hatch parameters were not changed. All this parameters were provided by Renishaw for this specific alloy. In Tab.3.4, Tab.3.5 and Tab.3.6 the values of the *Border*, *Additional Border* and *Fill Hatch* parameters are resumed:

Tab.3.4: Constant set of *BORDER* parameters.

POWER	EXPOSURE TIME	POINT DISTANCE
400 W	130 μs	100 μm

Tab.3.5: Constant set of *ADDITIONAL BORDER* parameters.

POWER	EXPOSURE TIME	POINT DISTANCE
400 W	150 μs	70 μm

Tab.3.6: Constant set of *FILL HATCH* parameters.

POINT DISTANCE	HATCH DISTANCE
130 μm	140 μm

It was decide to change Power, Exposure Time and Build Plate Temperature (related to *Fill Hatch* parameters) according with a full factorial design whose levels are listed in Tab. 3.7.

Tab.3.7: Levels of the investigated process parameters.

Build plate temperature[°C]	25-100-170
Laser power [W]	300-325-350-375-400
Exposure time [μs]	120-130-140-150-160

3.3) Heat treatments

Different isothermal heat treatments have been performed in order to understand the effects of each specific thermal cycle on the microstructure of the sample fabricated via selective laser beam melting. For the heat treatment it has been used an electrical muffle furnace. It was decided to follow the procedure provided by Renishaw, in which the sample need to remain under protective gas shielding at all times, avoiding oxidation phenomenon. For this reason, the samples have been incorporated in a vial containing Argon and then placed inside a preheated furnace. The heat treatments performed were the one provided by Renishaw and the others selected after an accurate calculation that will be better explained in the chapter of "Analysis of Results And Discussion".

The imposed thermal cycles can be resumed as follows:

- Heat to between 300°C and 320°C, holding for 2h and slow cool (Renishaw condition);
- Heat to between 300°C and 320°C, holding for 30 min and slow cool;
- Heat to 263°C, holding for 2h and slow cool;
- Heat to 263°C, holding for 30 min and slow cool;
- Heat to 294°C, holding for 2h and slow cool;
- Heat to 294°C, holding for 30 min and slow cool.

3.4) Sample preparation for metallurgical analysis

Before the microstructural observation, the samples were cut along the *z* axis (build direction) and after mounted in a cold EpoFix resin; then the surface preparation were carried out by using an automatic polisher. The polisher in question is the model Metkon 300-1V. During the polishing process the samples were polished by using first of all abrasive coarse papers followed by those used for finishing and finally a finer diamond is sprayed on cloths polishing is performed. The sequence of the abrasive papers and cloths used during rough grinding and fine polishing of aluminum is indicated below:

- Rough grinding with silicon carbide abrasive papers of 800, 1200 and 2500 grit in sequence for the initial material removal;
- Fine polishing using polishing cloths to produce a mirror finish. It was used diamond as abrasive particles sprayed on cloths before the beginning of the process. The three cloths used in this phase had an abrasive of 6, 3 and 1 μm.

After every step, the samples were subjected to the ultrasonic cleaning in distilled water to remove the extraneous particles remain entrapped on the top surface. In Fig.3.12 an example of sample after polishing process.
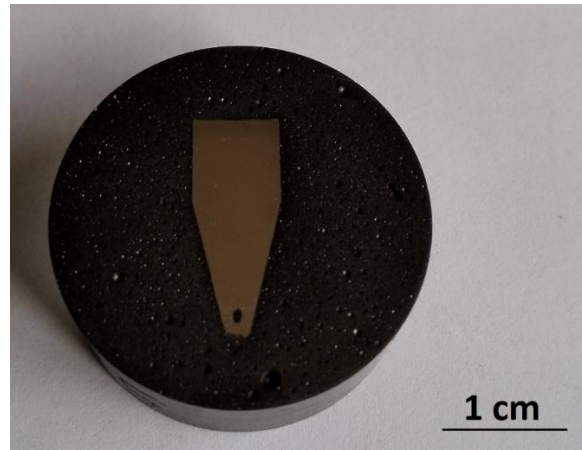
Fig.3.12: Polished sample in EpoFix resin.

After the sample placement inside the SEM chamber, a series of EDS measurements were performed to evaluate the elemental composition (≈1% std. dev.), estimating the level of the elements present in the sample. The samples were observed with SE signal to verify if any difference was present in the morphologies of the alloy.

3.5) Density measurement

The densities of the samples were measured by an electronic balance MOD.E50S/2 (see Fig.3.13), with the addition of a device for determining the solid density, which exploits the principle of Archimedes to obtain the density value of an object. A solid immersed in a liquid is exposed to the action of a force, which is equal to that of weight of the liquid displaced by the volume of the solid. The liquid used in this case is distilled water. Weighing the sample once in the air (P) and once in water (P'), its specific weight can be determine if the density of the liquid in which it is immersed is known . Due to the principle of Archimedes, P' is lower than P hence it is possible to state that:

$$S_A = P - P'$$

Where S_A is the Archimede push, P the sample weight in air and P' the sample weight in water. The volume of the object completely immersed in water is correlated to the Archimede push with the following relation:

$$S_A = \rho_{water} * g * V$$

Where ρ_{water} is the water density, g is the gravity acceleration and V is the volume of the object, hence the volume is equal to:

$$V = S_A / (\rho_{water} * g)$$

The weight P allows to determine the mass (m) as: $m = P/g$, and hence the object density (ρ_{object}) can be calculate in this way:

$$\rho_{object} = \frac{m}{V} = \frac{\frac{P}{g}}{\frac{S_A}{\rho_{water} * g}} = \rho_{water} * \frac{P}{S_A}$$
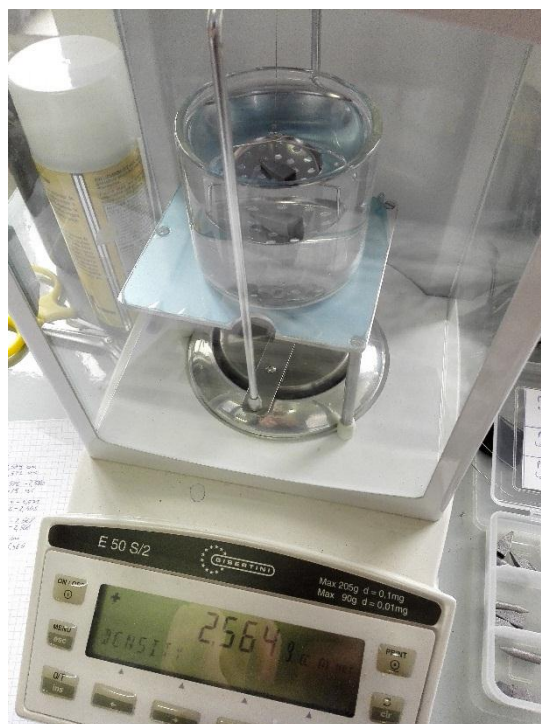
Fig.3.13: Electronic balance MOD.E50S/2; in device an example of density measurement after the sinking of the sample in distilled water.

Knowing the density of the material of reference is possible also estimate the relative porosity of the fabricated sample.

3.6) Scanning Electron Microscopy

The scanning electron microscope (SEM) is a type of microscope which uses, as a radiation source, the electrons. The interaction between the electrons and the sample generates a signal that reveals information about the specimen including the external morphology, chemical composition, crystalline structure and orientation of the materials of the sample. The signal produced by the electron-material interactions include secondary electrons (SE) and backscattered electrons (BSE). Secondary electrons are most valuable for showing morphology and topography on samples while backscattered electrons highlight contrasts in composition in elements samples based on mean atomic number.

The SEM observations are widely used to perform analysis of a specific area on the sample surface in order to acquire element maps, determining for example the chemical compositions. EDS (energy dispersive spectrometry) is an analytical technique used for chemical characterization or elemental analysis of a sample and its functional principle is that each element has a unique atomic structure allows a unique set of peaks on its X-ray emission patterns. In order to stimulate the emission of characteristic X-rays from a specimen, a high-energy beam of X-rays is focused into the sample. At rest, an atom within the sample contains a ground state (or unexcited) electrons in discrete energy levels or electron shells bound to the nucleus. The incident beam excites an electron in an inner shell, ejecting it from the shell while creating an electron hole where electro was localized. An electron from an outer, higher-energy shell then fills the hole, and the difference in energy between the higher-energy shell and the lower one may be released in the form of an X-ray. The number and energy of X-rays emitted from a specimen can be measured by an energy-dispersive spectrometer. As the energies of the X-rays are characteristic of the difference in energy between the two shells and of the atomic structure of the emitting element, EDS allows the elemental composition of the specimen to be measured. An example of EDS measurement is represented in Fig.3.14, representative the EDS spectrum of an AlSi10Mg alloy.
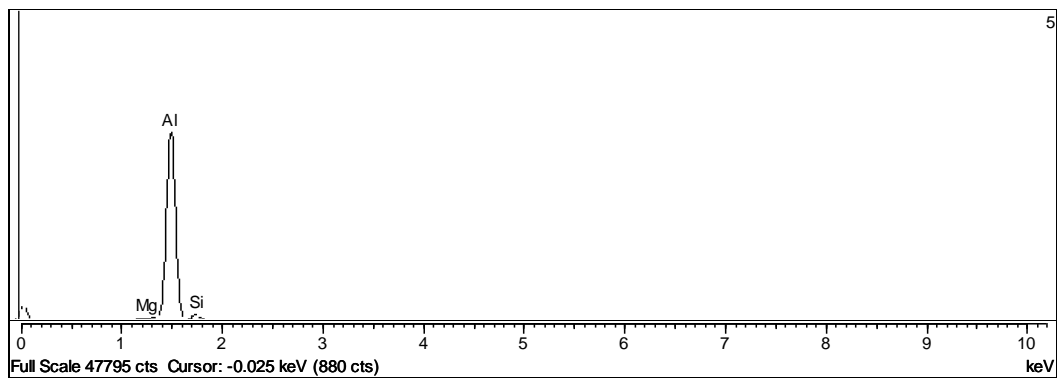
Fig.3.14: Example of EDS spectrum x-ray counts vs.energy (in keV). EDS spectrum of AlSi10Mg, containing detectable Al, Si and Mg.

SEM analysis were performed using a SEM model LEO 1430, represented in Fig.3.15.

Fig.3.15.SEM model LEO 1430 used to perform SEM analysis.

95

3.7) Optical Microscopy

Optical microscopy was used for low magnification analysis of the results. For the analysis of the sample surface (pore size and distribution) and the microstructural characterization, the light microscope provided by Leica (see Fig3.16), model Aristomet, with the support of a dedicated software (Leica Application Suite), was used; its maximum magnification is 1000x.
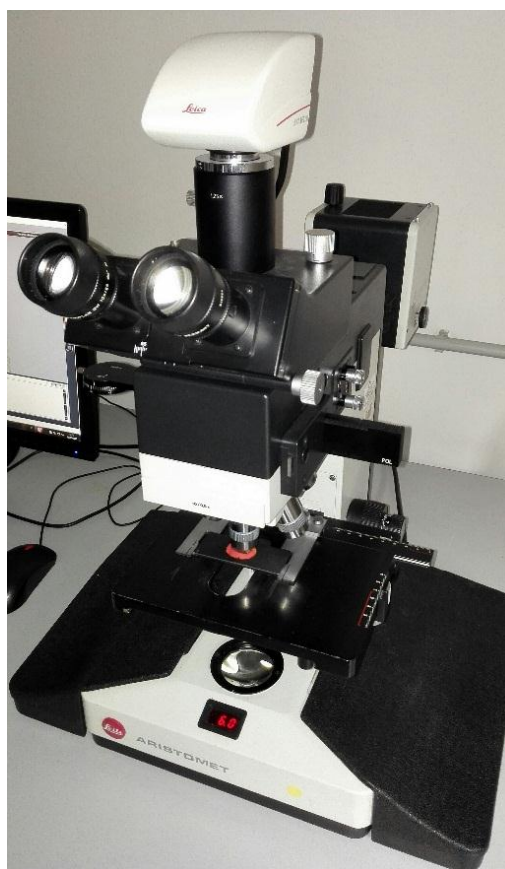
Fig.3.16: Leica microscope model Aristomet used for the optical analysis.

The same samples considered for the SEM analyses were also used for the analysis by using the microscope. However, for the microstructural characterization, the chemical attack with Keller reactant was necessary in order to point out the crystalline structure. After the immersion in the reactant for five seconds, the sample is immersed in water.

3.8) Thermal Analysis

The thermal analysis were used for the characterization of the metallurgical transformation and hence to determine the material properties at varying of the temperature. Through the thermal analysis it is possible to determine different material properties such as enthalpy, thermal capacity, mass changes and the coefficient of heath expansion. According to the aim of analysis it is possible to select the best method with which thermal analysis has to be carried out.

In this thesis, the Differential Thermal Analysis (DTA) and the Differential Scanning Calorimetry (DSC) have been carried out for the thermal characterization of the aluminum alloy. During the DTA the material under study and an inert reference are subjected to a thermal cycle: the heat flow to the sample and reference are measured. Physical and chemical phenomena can cause changes in heat/temperature. Exothermic phenomena like crystallization, oxidation, etc. and endothermic phenomena like melting, vaporization, reduction, etc. are seen with peaks (changes in heat/temperature). During the peak evaluation TA data, onset and integral of peaks have been analyzed together with the height and width of the peak.

By using the DSC technique, it is possible to measure melting temperature, heat of fusion, latent heat of melting, the reaction energy and temperature, the glass transition temperature, crystalline phase transition temperature and energy, precipitation energy and temperature, oxidation induction times, and specific heat or heat capacity. The DSC measures the amount of energy absorbed or released by a sample when it is heated or cooled, providing quantitative and qualitative data on endothermic (heat absorption) and exothermic (heat evolution) processes.

A representative example of these measures is depicted in Fig.3.17.
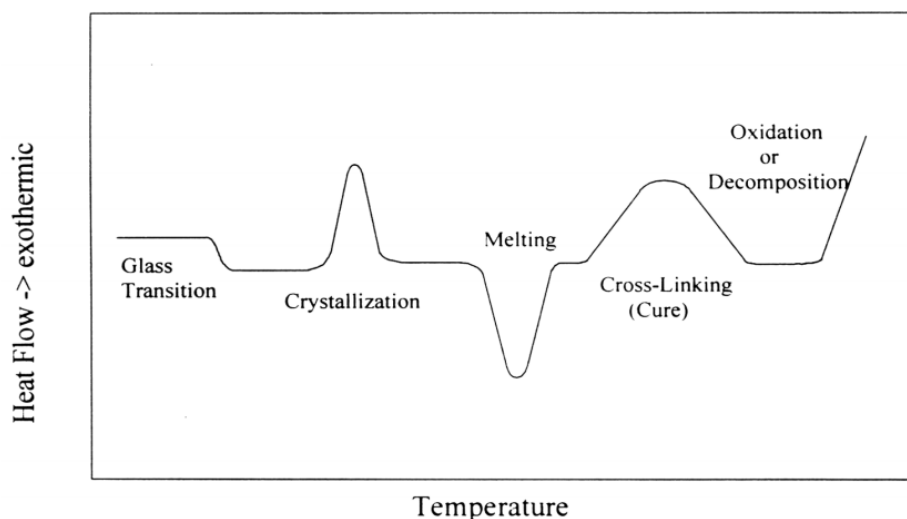
Fig.3.17: Example of DTA-DSC curve and the respective transformations.

The DTA analysis has been performed on a Q600 machine provided by TA Instruments. The Q600 provides simultaneously measurement of weight change (TGA) and true differential heat flow (DSC) on the same sample from ambient to 1500°C. It features a field-proven horizontal dual beam design with automatic beam growth compensation, and the ability to analyze two TGA samples simultaneously. DSC heat flow data is dynamically normalized using instantaneous sample weight at any given temperature (http://www.tainstruments.com). In Tab.3.8 the main specific data about the Q600 machine are listed.

Tab.3.8: Main data of DTA machine model Q600.

Sample Capacity	200 mg (350 mg including the sample holder)
Balance Sensitivity	0.1 μg
Temperature Range	Ambient to 1500°C
Heating Rate – Ambient to 1000 °C	0.1 to 100°C/min
Heating Rate – Ambient to 1500°C	0.1 to 25 °C/min
Furnace Cooling	Forced Air (1500 to 50°C in < 30 min 1000°C to 50°C in < 20 min)
DTA sensitivity	0,001 °C
Calorimetric Accuracy	±2%

The Q600 features a highly reliable horizontal dual-balance mechanism that supports precise TGA and DSC measurements (see Fig.18). It delivers superiority in weight signal measurements (sensitivity, accuracy and precision) over what is available from single beam devices, since the dual beam design virtually eliminates beam growth and buoyancy contributions to the underlying signal. It also uniquely permits independent TGA measurements on two samples simultaneously.

Fig.3.18: On the left, the Q600 used for the DTA analysis, on the right the two pans (one empty and one in which the analyzed sample is placed).

The samples used for the DTA analysis were cut so that the sample weight was about 10 mg in order to allow the machine to perform the most appropriate measurement. Then the sample was put into alumina pans. The system heated the sample up to 200 °C, and it performed an isothermal for 1 minute in order to be sure that the sample has reached that temperature. Then a temperature cycle was imposed to the sample increasing temperature from 200°C up to 700°C imposing a temperature rate of 30°C/min then the machine performed the cooling from 700°C to 200°C with the same temperature rate of the heating one.

The model of DSC used in my work is a Seiko SSC/5200 quipped with a nitrogen liquid for the cooling system, as shown in Fig.19.
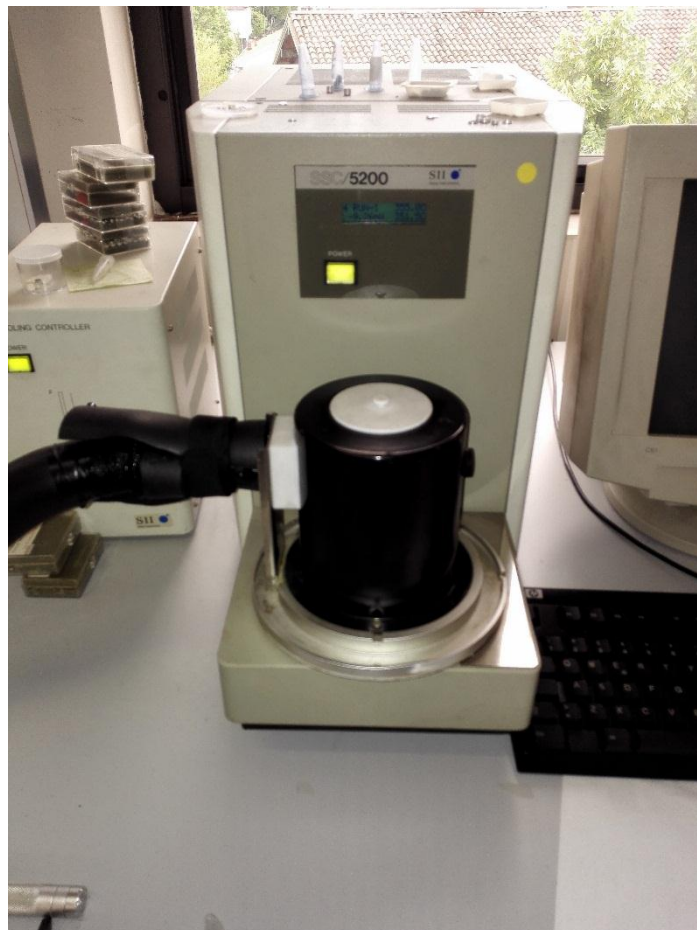
Fig.3.19 DSC Seiko SSC/5200 used for calorimetric analysis

This is a very sensitive instrument, within which only non-corrosive samples can be analyzed. The analysis is performed by placing in a special housing, inside the measuring chamber, two pans are placed, one containing the sample under analysis and one used as a reference sample for the test. The two pans are made by the same material and they can resist to the high temperatures without reacting with the sample. The machine is provided with a scale that measure the sample weight after the tare considering just the two pans. The chamber is then hermetically closed to insulate the working environment from the outside. The presence of the reference pan is of fundamental importance to obtain an output signal that is independent on the thermic effects external to the system and it allows to detect as output the own temperature of the material itself, regardless the conditions of

the experiments. The temperature if the two samples is monitored through a thermocouples, placed in the platform below the aluminum pans and that send temperature data to the computer processing them an generating the output for the user. Once the test starts, the heat provided by the furnace heats the sample and the reference pan, in the same way. Each variation of temperature between two is due to the induced phenomenon, for example an exothermal reaction will increase the sample temperature while an endothermic will reduce the sample temperature. Once the test is concluded the machine cools down making possible the sample removal.

In order to make the DSC analysis of the material, the selected sample were cut considering that the sample length had to be sufficiently high to guarantee an adequate contact surface between the material and the thermocouple (about 5 mm). The prepared sample was put into aluminum. The temperature cycle imposed to the sample starts from 0°C up to 500°C (and from 500°C down to 0°C) imposing a temperature rate equal to 20°C/min.

The effect of the thermal cycle on different samples was investigated. These characterization were done to find some correlation between the samples, fabricated imposing different process parameters, and the results of the thermal analysis.

3.9) Micro-Hardness Tests

In order to get an approximate measure of the mechanical resistance of the fabricated samples, Vickers micro-hardness tests were performed. This test method consists on indenting the test material with a diamond indenter, in the form of a right pyramid with a square base and an angle of 136 degrees between opposite faces (see Fig.20). By measuring the two diagonals of the indentation left in the surface of the material after removal of the load, it is possible to calculate the hardness of the material, which is proportional to the applied load (P) and to the diagonal (d), which is the arithmetic mean of two diagonal d_1 and d_2 in mm:

$$HV = 1,854 \frac{P}{d^2}$$

The samples were analyzed by using a durometer, set to a 300 g load and an indentation time of 15 s. Before testing, all samples were carefully polished in order to avoid large measurement oscillations.
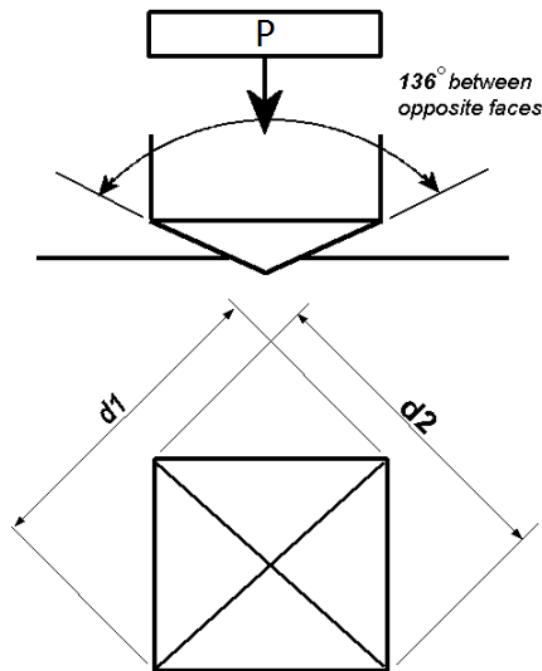

Fig.3.20: Schematic of the Vickers hardness test. P is the applied load, d_1 and d_2 the two diagonals of indentation.

3.10) X-ray Diffraction

The X-ray diffraction is a non- destructive analytical technique used for the identification and the quantitative determination of the crystalline phases present in a polycrystalline material. The technique also allows, by means of dedicated software, the structural study-crystallographic (symmetry, dimensions and characteristics of the unit cell), as well as the microstructural analysis of the crystalline phases. The X-rays employed are in fact electromagnetic radiation characterized by a wavelength comparable with the interatomic distance, and, penetrating (≈10μ) into the material by effect of their low absorption coefficient, generate diffraction phenomena which allow to obtain information on the positions atomic and their nature. When X-ray hits an atom, in fact, the inner electrons go into oscillation: each atom can be considered a source of spherical wave with intensity proportional to the number of its electrons. The waves spread give constructive interference depending on the symmetry properties of the system. The principle of operation of most of laboratory X-ray diffractometer is based on the reflection or Bragg diffraction (see Fig.21), for which the phenomenon of diffraction from a crystal can be described as a selective reflection of monochromatic radiation by the atomic planes: a collimated monochromatic X-ray beam is reflected from a set of crystal planes, generating a structure of interferential intensity peaks, called diffraction pattern, in the surrounding space. Each crystalline phase is associated with a specific set of diffraction peaks (Bragg peaks), which allows the recognition by comparison with standard reference cards.

The Bragg's law says that:

$$n\lambda = 2d_{hkl}sin\vartheta$$

Where:

d_{hkl} = interplanar distance of the family of reticular planes defined by indices (h,k,l)
λ = wavelength of the incident radiation
ϑ = angle of reflection (which is equal to the angle of incidence)
n = positive integer

Fig.3.21 represents the schematic of the XRD measurement.
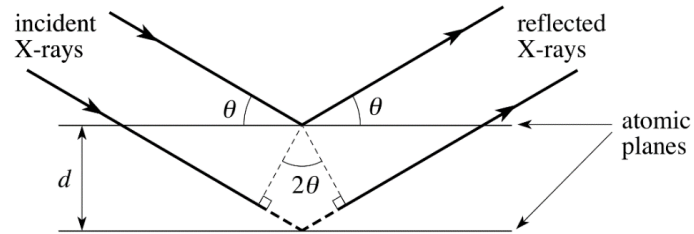
Fig.3.21: Schematic representation of the Bragg's law.

The diffraction pattern or diffractogram is constituted by a series of peaks or reflections having different intensity and angular positions relative to the various phases present in the investigated sample, as it is possible to observe in Fig.3.22 (L.P. Lam, 2015).
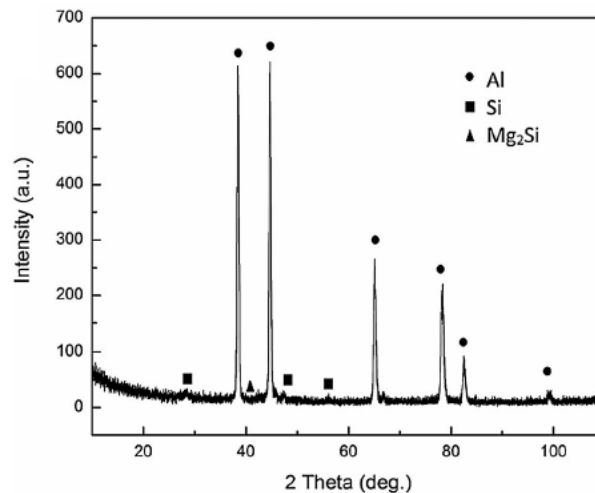
Fig.3.22: Example of XRD of AlSi10Mg sample fabricated via laser melting.

In a mixture in which there are several phases, the diffractogram results by the sum of the individual patterns associated with each crystalline phase. The diffraction pattern of a crystal is useful not only for its rapid identification but also for a complete interpretation of its structure. This shows the phases present (peaks position), the concentration of the phases (relative peaks intensity), the content of amorphous (broad features between the background) and size / deformation of the crystallites (width and peak shape).

X-Ray Diffraction patterns were collected by a diffractometer Bragg-Brentano (Panalytical X'Pert Pro) using Cu Kα radiation operating at 40 kV and 30 mA in the 5-120° 2θ range for 90 minutes.

Chapter 4

Analysis of Results and Discussion

In this chapter the main results achieved in the characterization of the starting powder and of the laser melted samples, fabricated by varying the process parameters, are reported and discussed.

4.1) AlSi10Mg Powder Characterization

The initial powder has been subjected to different types of analyses allowing the determination of different reference conditions related to the unprocessed material, that can be used as comparison pattern for the samples fabricated by laser melting technology.

First of all, powder was observed by SEM: secondary electrons made possible to verify the shape and size of the powder. In Fig.4.1, it can be seen that the expected spherical configuration typical of the AlSi10Mg powder is seldom visible. Powders mainly exhibit a globular shape with many irregularities. This feature is expected to be avoided by using the gas atomization process which is preferred to the water-atomization one. The water-atomized powders are more irregular and this characteristic causes the different orientations of the particles along preferential directions during the powder spreading, increasing the risk of porosity and residual tensions inside laser melted part (Yadroitsev, 2012). This is the reason why the gas-atomized powder is preferred to the water-atomized one.

Fig.4.1: SEM image of the gas-atomized powder.

The second step was to observe the polished powder by using the microscope. This analysis made possible to see the microstructure typical of AlSi10Mg powder. In Fig.4.2 the α-Al matrix (bright phase) and the eutectic Si-particles (dark phase) are visible. The solidification structure is characterized by dendrites mainly oriented along radial directions. Being the microstructure strongly dependent on the process conditions, it will be object of interest to see the effects induced by the laser melting in the material, as far as the process generates in the material high temperature gradients together with high cooling rates.
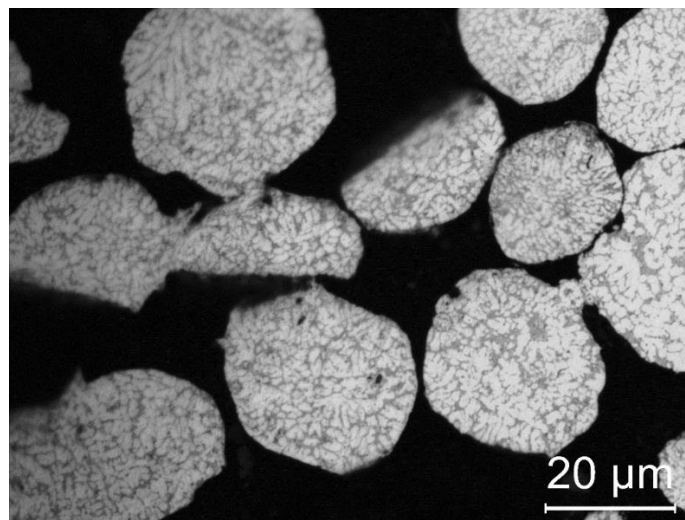
Fig.4.2: Microscope image of the microstructure (magnification 1000x) of fresh powder distinguishing α-Al matrix (bright phase) and eutectic Si-particles (dark phase).

After the optical observation, the thermal characterization of the AlSi10Mg powder were performed. For this purpose, both DTA and DSC systems were used in different ranges of temperature. Through this analysis it has been possible to determine the melting temperature of the aluminum powder which corresponds to 598°C (Fig.4.3). Also the enthalpy of fusion and the onset temperature (which is the temperature at which the reaction, in this case fusion, starts) has been calculated and they are respectively: 419,1 J/g and 574,64°C. It is reasonable to think that if no variation of the material's chemical composition during the laser melting will occur, the melting temperature of the obtained sample will be the same of the initial powder.
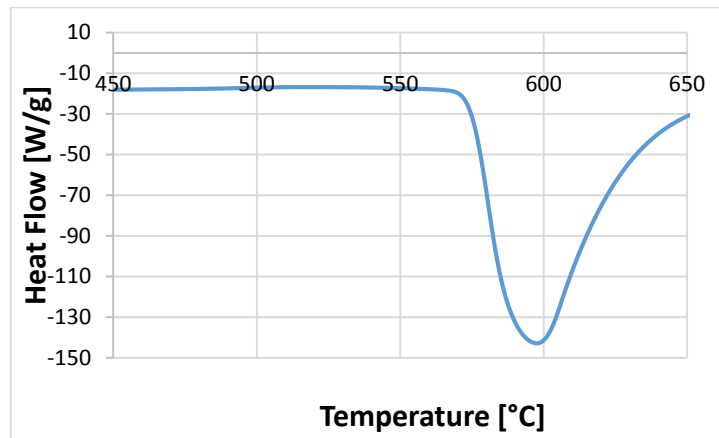
Fig.4.3: DTA of AlSi10Mg initial powder.

Also in DSC analysis both heating and cooling cycles were considered reaching a maximum temperature of 500°C, that is lower then the maximum one used for the DTA. The main purpose of this analysis was to evaluate if any exothermic/endothermic reactions occurred during the heating/cooling cycles. Fig.4.4 represents a complete DSC scan of the AlSi10Mg powder.
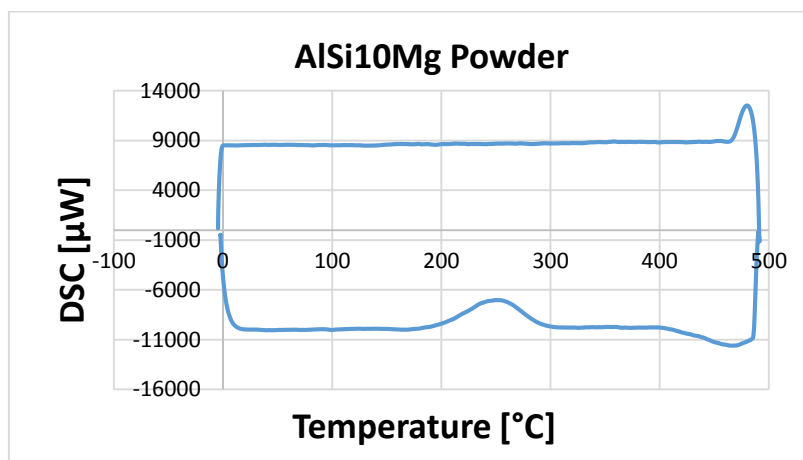
Fig.4.4: DSC measurement of AlSi10Mg powder.

The result shows an exothermic transformation in the range of temperature included between 175°C and 320°C. Further analyses will demonstrate that this peak is associated to the precipitation of the Mg_2Si phase, which is very fine.

The powder characterization results will be useful to better understand the effects of laser melting process on the material properties, as it will be illustrated in the next chapters.

4.2) Characterization of Laser Melted Samples

In this chapter the characterization of the laser melted samples is performed and the effect of varying laser power, exposure time and build plate temperature is studied. In Fig.4.5, the as-built samples, after the laser melting and subsequent extraction from the process chamber, are illustrated.
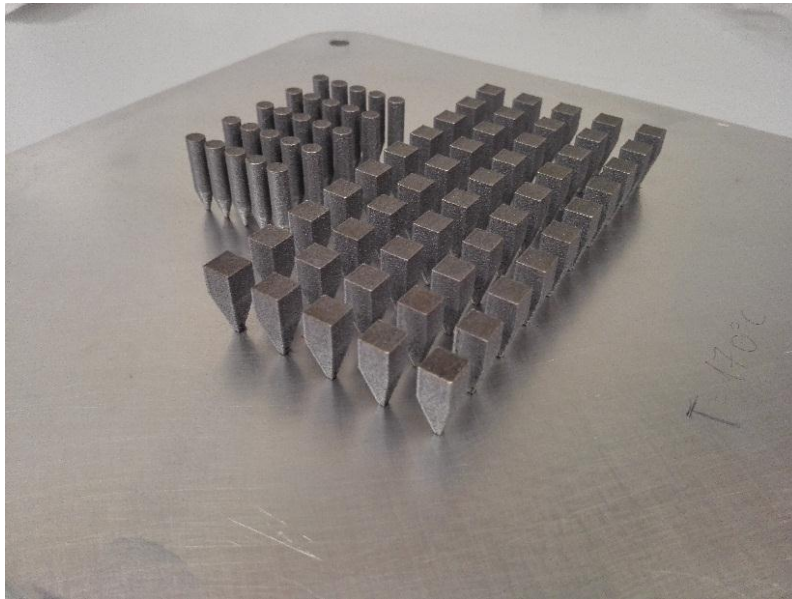
Fig.4.5: As-built samples.

Different analyses have been performed on these samples with the aim of understanding the main effects of process parameters variation on the material microstructure and mechanical properties.

Initially the external surface of as-built samples has been observed by using optical and scanning electron microscopy. It is important to remember that the process parameters in Border and Additional Border zones are different from those selected for the core region of the samples. As illustrated in Fig.4.6, the external surface presents many irregularities, which have been investigated more in detail in the SEM images (see Fig.4.7 and Fig.4.8). However, the roughness can be improved selecting more appropriate process conditions, referred to those particular zones. Usually the laser melted parts are subjected to a sandblasting process which further improves the surface quality. In this case the postprocessing was not taken into account.
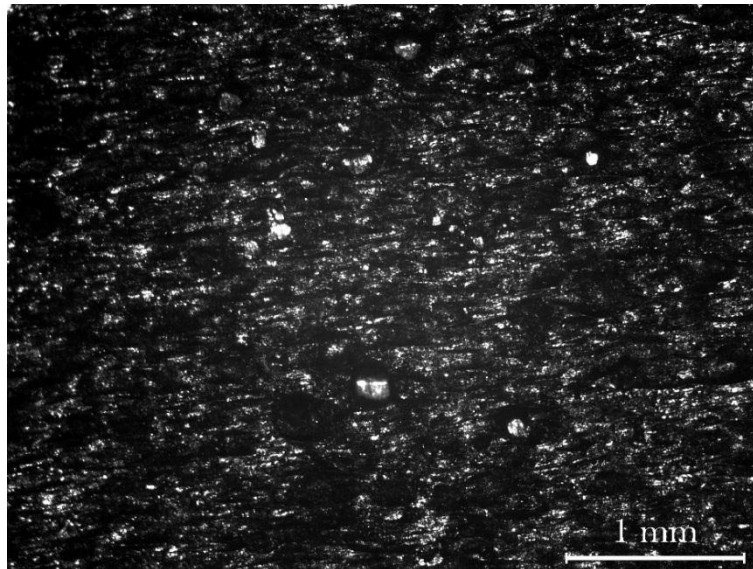
Fig.4.6: External surface of the laser melted sample.
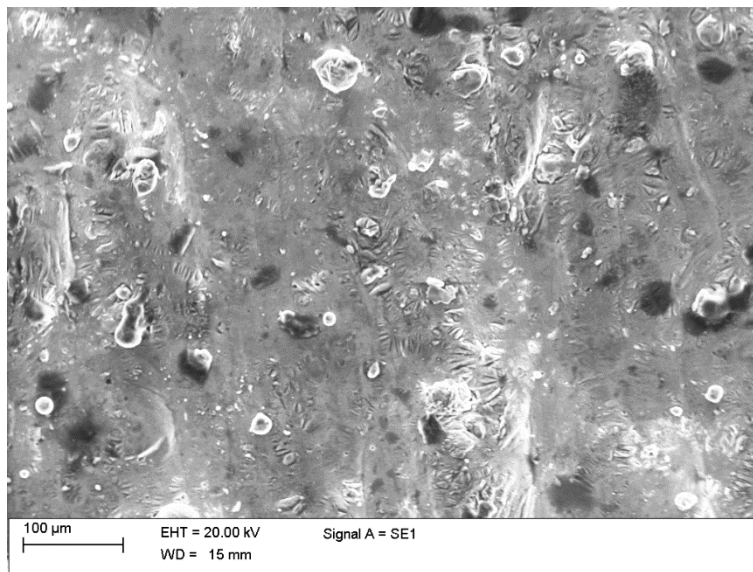
Fig.4.7: SEM image of the external surface (500x).
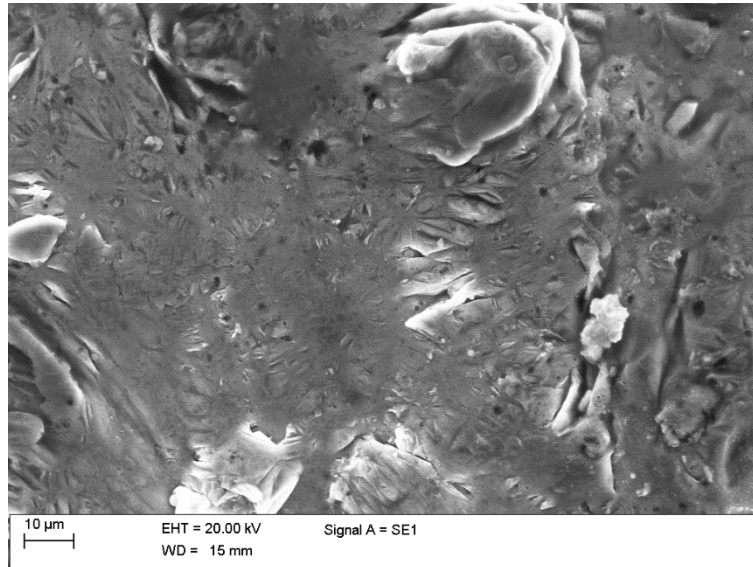
Fig.4.8: SEM image of the external surface (2500x).

4.2.1) Density Analysis

The density measurements have been the initial step for the characterization of the as-built samples. It has been object of interest evaluating the changes in samples density due to the variation of the investigated process parameters. A statistical analysis has been performed, using Minitab software, in order to determine the correlation between power, exposure time, build plate temperature and the samples density.

In Fig.4.9 the Interval Plot of the density, which indicates the mean values of the density measurements according to each process condition and its confidence interval (calculated at 99%), is reported. Additionally, the density of AlSi10Mg alloy (wrought material), which is 2,68 g/cm^3, is indicated as reference by a dashed line.

All results show a density lower than the one achievable in the wrought material. Increasing the build plate temperature, it is possible to see a reduction of the samples density; furthermore, an increase of the laser power and interaction time can reduce the sample density. However, these indications are going to be verified applying a statistical method of data analysis.
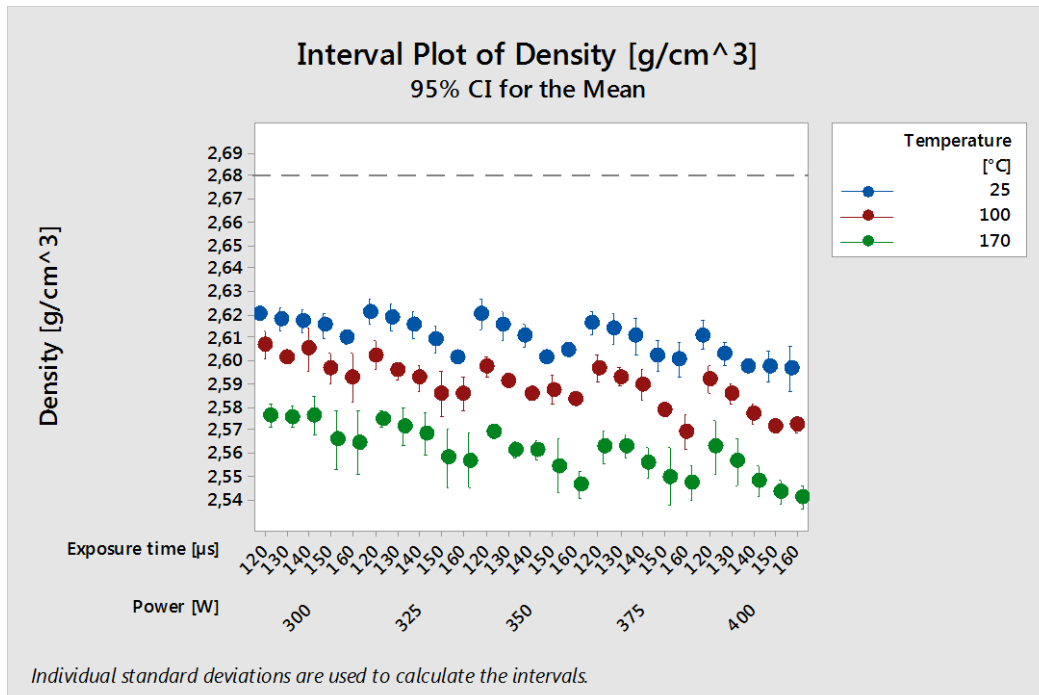
Fig.4.9: Interval Plot of the Density for each process parameter combination (Power, Exposure Time and build plate Temperature) is represented. The point indicates the mean while the line indicates the confidence interval.

The Main Effects Plot was performed comparing the process parameters magnitude and to determine the main effects of these factors on the obtained densities, as shown in Fig.4.10. The points in the plot are the data means of the response variable at various levels of each factor, with a reference line drawn at the grand mean of the response data.

In Fig.4.10 it is possible to observe the horizontal line (grand mean) and how the density varies by varying the process parameters, considered as distinct. Considering that the effects are evaluated as the difference between the means and the reference line (the entire average value), the largest effect on the sample density appears given by the build plate temperature, while the power and the exposure time seem to give the same effects on the response variable but lower than the build plate temperature.
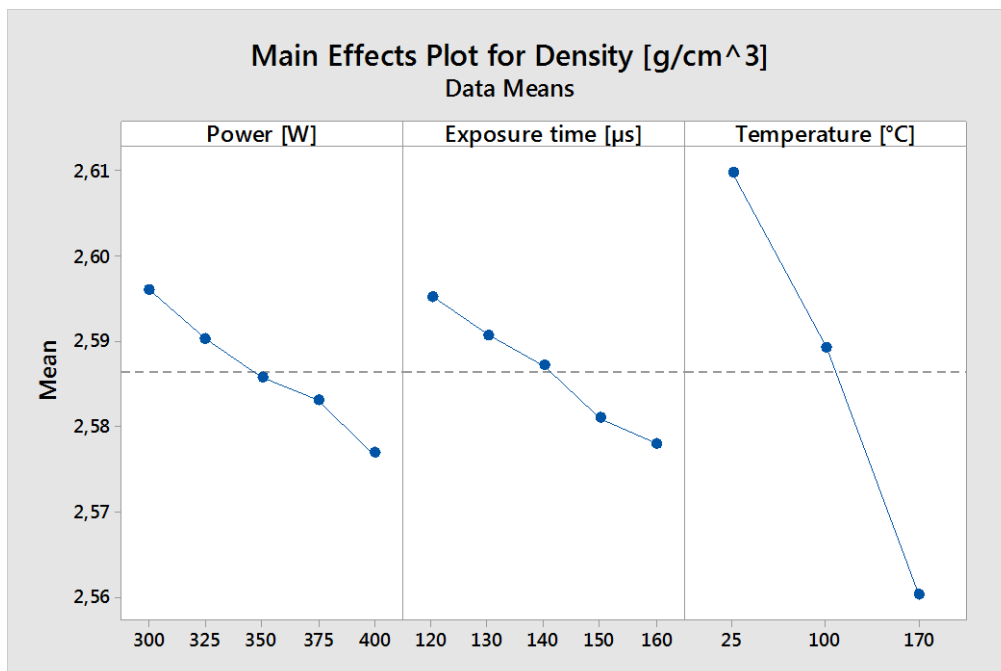
Fig.4.10: Main Effects Plot for Density of the Power, Exposure Time and Build Plate Temperature.

The result is in accordance with the results of the interval plot analysis, in which a high reduction of the sample density occurs mainly increasing the build plate temperature.

Due to the potential effect of variation of couples of process parameters, Interaction Plots were performed to evaluate how different combinations of factors interfere on the response obtained densities, as shown in Fig.4.11. This analysis is useful to judge the presence of interaction between the process parameters. Parallel lines in an interaction plot indicate no interaction.

The results of the interaction between the three process parameters combined in different ways show different types of interactions. Analogous plots are present for Power by Temperature interaction (third raw and first column & first raw and third column) and Exposure Time by Temperature interaction (second raw and third column & third raw and second column). In these plots the lines are almost parallel and this means that no interaction between these combination of factors and the density occurs. In the Exposure Time by Power interaction (second raw and first column & first raw and second column) it is possible to observe that the lines are not parallel and hence interaction occurs between these two factors and the response variable (the density), and this makes sense, since in the energy density expression these two parameters are directly correlated.
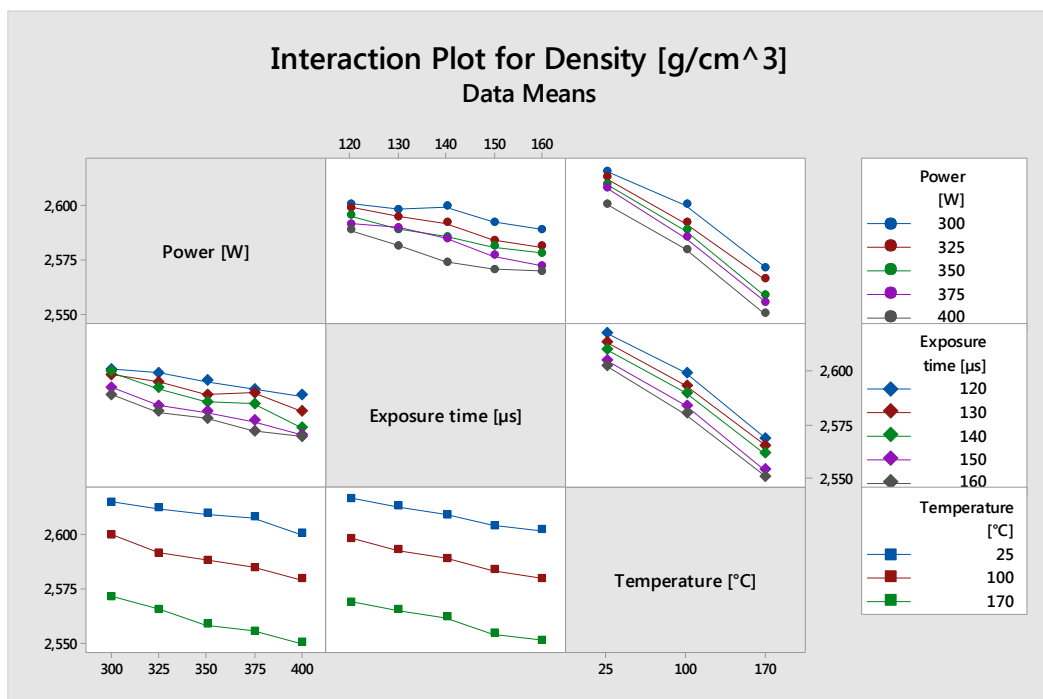
Fig.4.11: Interaction Plot of the Density. The parallel lines indicate that no interaction between the two considered variables is present. If the lines are not parallel it means that between the two considered variables, an interaction is present.

At the end of the statistical analysis the relationship between density and process parameters was further investigated, looking at the analysis of variance (ANOVA), where it has been possible to verify which process condition is influential on the dependent variable (the density) evaluating the p-value. If it is significantly different from zero, it means that the considered process parameter has no effect on the sample density. More

precisely, the p-value needs to be compared with the <u>α-level</u> (0.05): if p-value ≤ α, the effect is significant, while if p-value > α, the effect is not significant.

In addition, the interaction between process conditions have been evaluated too. In ANOVA table (Tab.4.1), the p-values of power, exposure time and build plate temperature are equal to zero and this means that they are all significant factors. Looking at the interaction (multiplied factors) between them, just the one composed by the power and the temperature is influential on the density. To check the reliability of the entire statistical analysis, it is necessary to evaluate the R^2 value which can be included between 0 (no reliability) and 1 (maximum reliability). In our case it is equal to 93,53% and this means that the reliability of the analysis is high.

Tab.4.1: ANOVA for Density.

Source	DF	SS	MS	F-value	P-value
Power [W]	4	0,0189752	0,0047438	112,94	0,000
Exposure time [µs]	4	0,0178187	0,0044547	106,06	0,000
Temperature [°C]	2	0,1868813	0,0934406	2224,68	0,000
Power [W]*Exposure time [µs]	16	0,0013793	0,0000862	2,05	0,010
Power [W]*Temperature [°C]	8	0,0009670	0,0001209	2,88	0,004
Exposure time [µs]*Temperature [°C]	8	0,0001998	0,0000250	0,59	0,782
Power [W]*Exposure time [µs]* Temperature [°C]	32	0,0013441	0,0000420	1,00	0,471
Error	375	0,0157507	0,0000420		
Total	449	0,2433160			

S = 0,00648088   **R-Sq** = 93,53%   **R-Sq(adj)** = 92,25%

After these considerations, the regression analysis was performed including all conditions having an acceptable p-value. This analysis allows to fit an equation of the density, investigating and modelling its relationship with considered variables and returning the ANOVA, the coefficients table, the R-sq value and the regression equation. To evaluate if equation coefficients can be considered "insignificant" (equal to zero), we have to check the p-values that are all acceptable (Tab.4.2). Once the model is estimated it is also possible to calculate the goodness of the fit through the R^2 index between 0 and 1, represented in Tab.4.2. In our case the R^2 is equal to 90,91%, which means that the fit is very good.

Tab.4.2: ANOVA table density and the influential variables.

```
Source               DF  Adj SS    Adj MS    F-Value    P-Value
Regression            4  0,221200  0,055300  1112,72    0,000
  Temperature [°C]    1  0,000391  0,000391     7,88    0,005
  Exposure time [µs]  1  0,017662  0,017662   355,39    0,000
  Power [W]           1  0,002549  0,002549    51,29    0,000

  Power*Temperature   1  0,000551  0,000551    11,09    0,001

Error               445  0,022116  0,000050
  Lack-of-Fit        70  0,006365  0,000091     2,16    0,000
  Pure Error        375  0,015751  0,000042
Total               449  0,243316

S=0,0070497  R-sq=90,91%   R-sq(adj)=90,83%   R-sq(pred)=90,69%
```

In the coefficient table (Tab.4.3), the Variance of inflation factors (VIF) used to describe how much the considered variables are linearly dependent among them, is also indicated. The linear dependence is a problem because it can increase the variance of the regression coefficients making them unstable and difficult to interpret. If VIF=1, the variables are not correlated, if 1<VIF<5 they are moderately correlated and if VIF > 5 they are highly correlated. Looking at the VIF, excluding the one of the exposure time, the others are highly correlated, hence the variance of the regression equation is rather high.

Tab.4.3: Coefficients table.

Term	Coef	SE Coef	T-Value	P-Value	VIF
Constant	2,72777	0,00721	378,58	0,000	
Temperature [°C]	-0,000157	0,000056	-2,81	0,005	99,00
Exposure time [µs]	-0,000443	0,000023	-18,85	0,000	1,00
Power [W]	-0,000131	0,000018	-7,16	0,000	3,76
Power [W]* Temperature [°C]	-0,000001	0,000000	-3,33	0,001	101,76

The determined regression equation was:

$$Density = 2{,}72777 - 0{,}000157 * T - 0{,}000443 * Et - 0{,}000131 * P - 0{,}000001 * P * T$$

In Fig.4.12, Fig.4.13 and Fig.4.14 it is possible to see how the density varies considering just the variation of two process parameters per time.
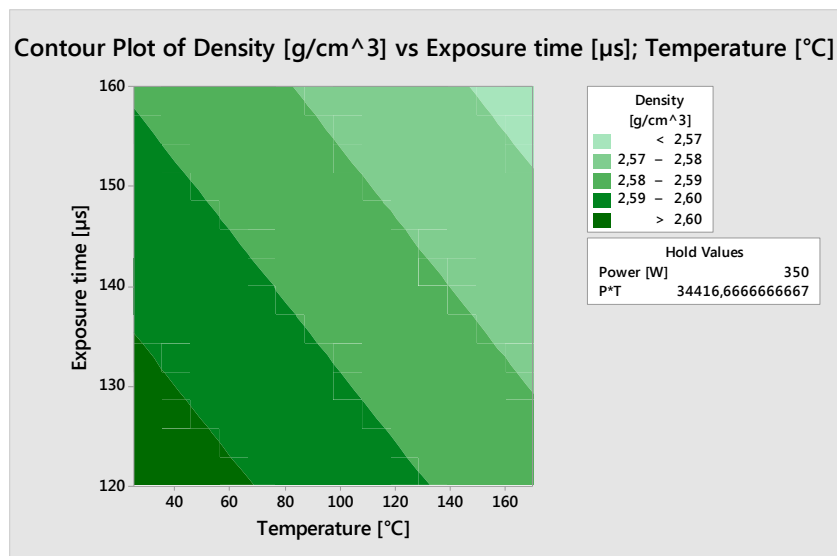

Fig.4.12: Contour Plot of Density in function of exposure time and temperature.
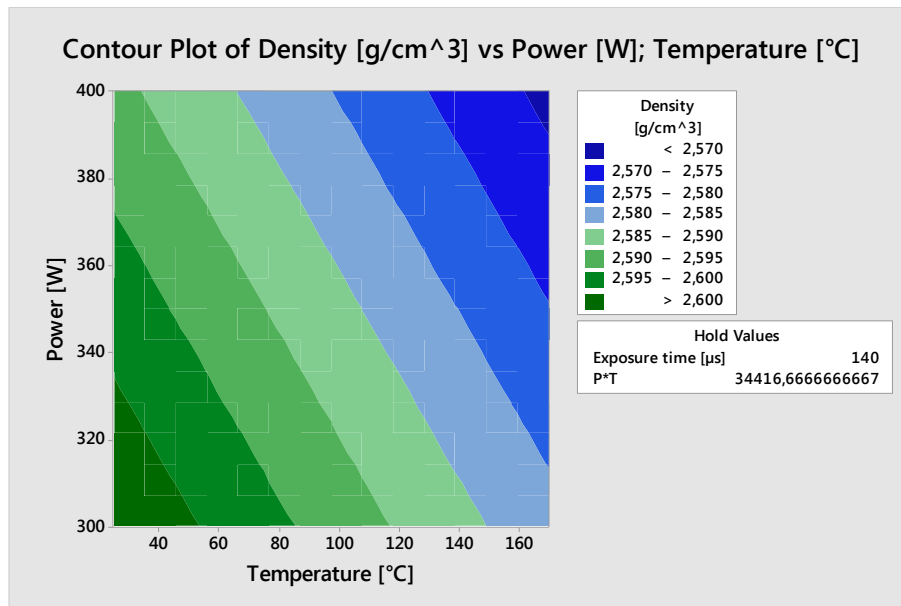
Fig.4.13: Contour Plot of Density in function of power and temperature.
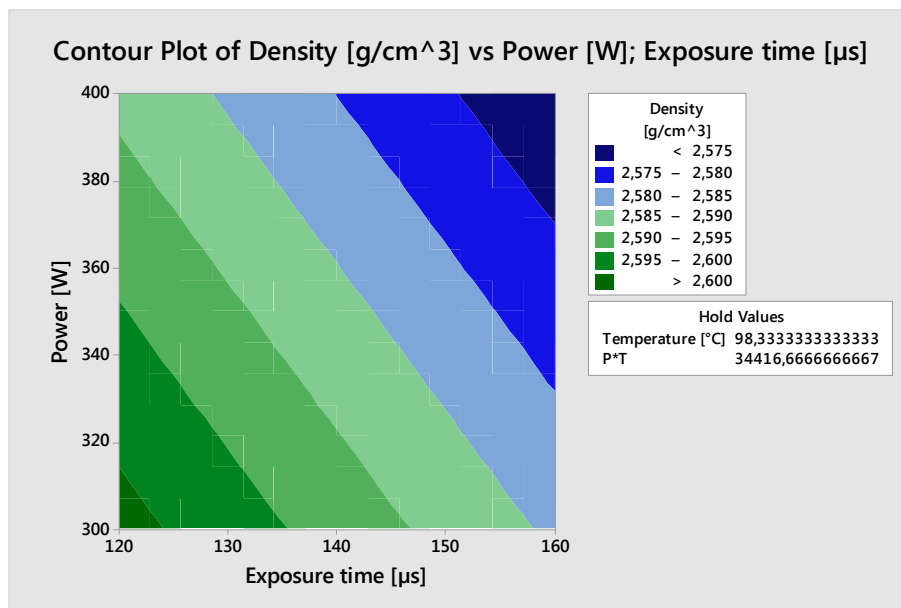
Fig.4.14: Contour Plot of Density in function of power exposure time.

At the end of the statistical analysis, the relative densities have been calculated with respect to the wrought material (considered as fully dense), in order to have a percentage estimation of the relative density and porosity of each sample. The results have shown that the relative density range is included between 94,90% and 97,80%. The maximum density has been found imposing 300W (power), 120μs (exposure time) and on the build plate at room temperature, while for the minimal density the process parameters were: 400W, 150μs and the build plate temperature equal to 170°C.

In Fig.4.15, Fig.4.16 and Fig.4.17 the trends of the samples relative density considering different combinations of Power, Exposure Time and Build Plate Temperature, are illustrated.

Fig.4.15: Relative density of fabricated samples, considering the build plate temperature equal to 25°C.

Fig.4.16: Relative density of fabricated samples, considering the build plate temperature equal to 100°C.
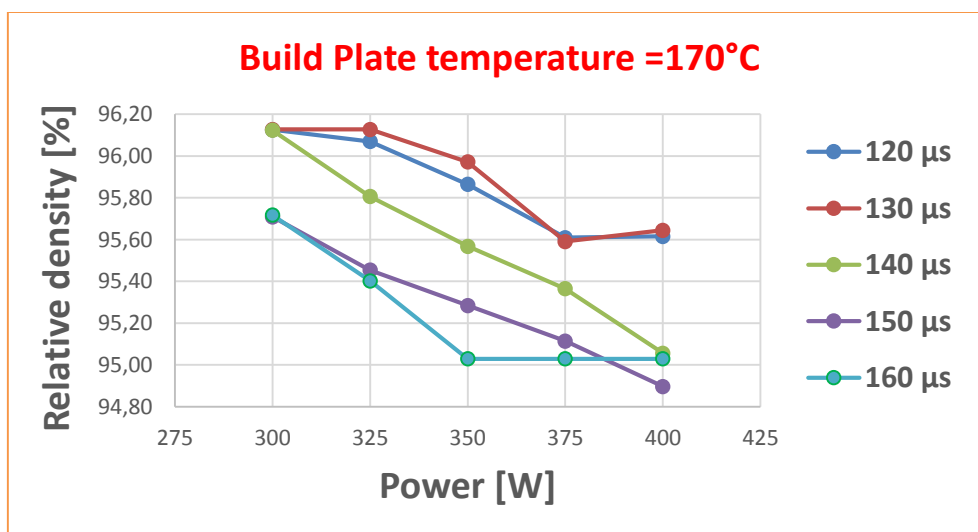
Fig.4.17: Relative density of fabricated samples, considering the build plate temperature equal to 170°C.

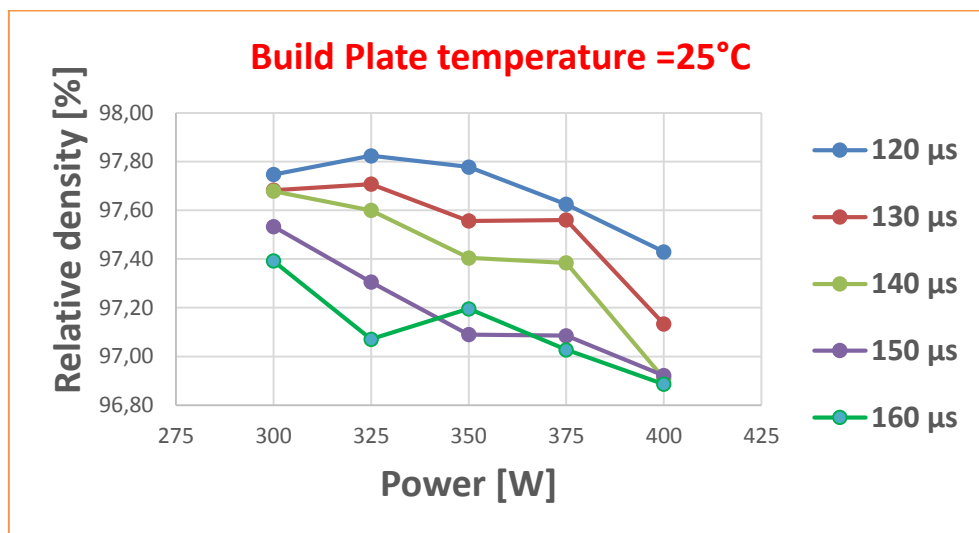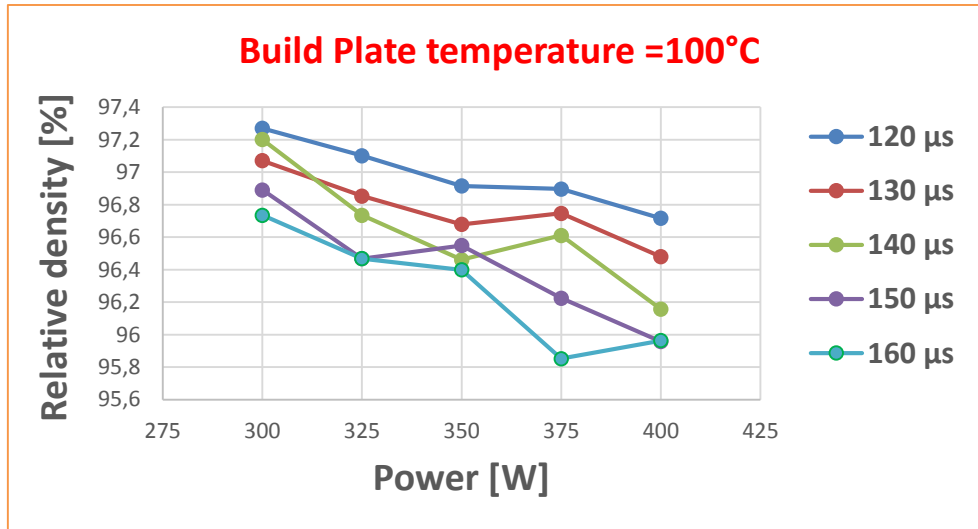The results of the density analyses have been implemented with that of the optical analysis where it was possible to observe the pores conformation and compare the relative density previously calculated with that of the longitudinal section of some polished samples by using a software. The selected samples for this analysis are indicated in Tab.4.4.

Tab.4.4: Process parameters combinations for the optical analysis.

Power	Exposure Time	Build Plate Temperature
300	120	25
300	160	25
400	120	25
400	160	25
300	120	170
300	160	170
400	120	170
400	160	170

The software used to calculate the percentage of the porosity observing the polished surface with the microscope was Image J. The operating principle of this program is the calculation of the percentage of the black surface and of the white one, of the acquired image. First of all the 10 images were acquired of the same sample by using the microscope at 50x of magnitude, possibly avoiding the scratched areas, and then the calculation of the dark background (the black represents the bulk material and the white the pores, see Fig.4.18), was performed, controlling that all pores were present.

The software returns a table containing all measurements of each analyzed sample. The relative density results of the single sample were averaged and compared with those resulting from the Archimede tests.
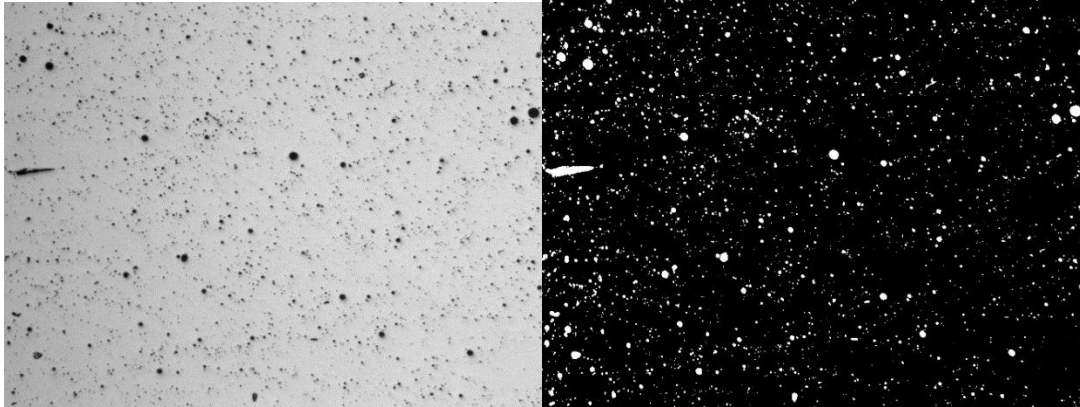
Fig.4.18: Image conversion performed by Image J program. The image is acquired using the microscope (on the left) and converted in a black and white image (on the right) making possible the execution of the relative density analysis.

All relative density results of the two types of analyses have been compared, as illustrated in Fig.4.19 and Fig.4.20. Although they are not perfectly coincident, the interval bars, of the same sample submitted to the two types of measurements, are overlapped. This means that the difference is not significant.
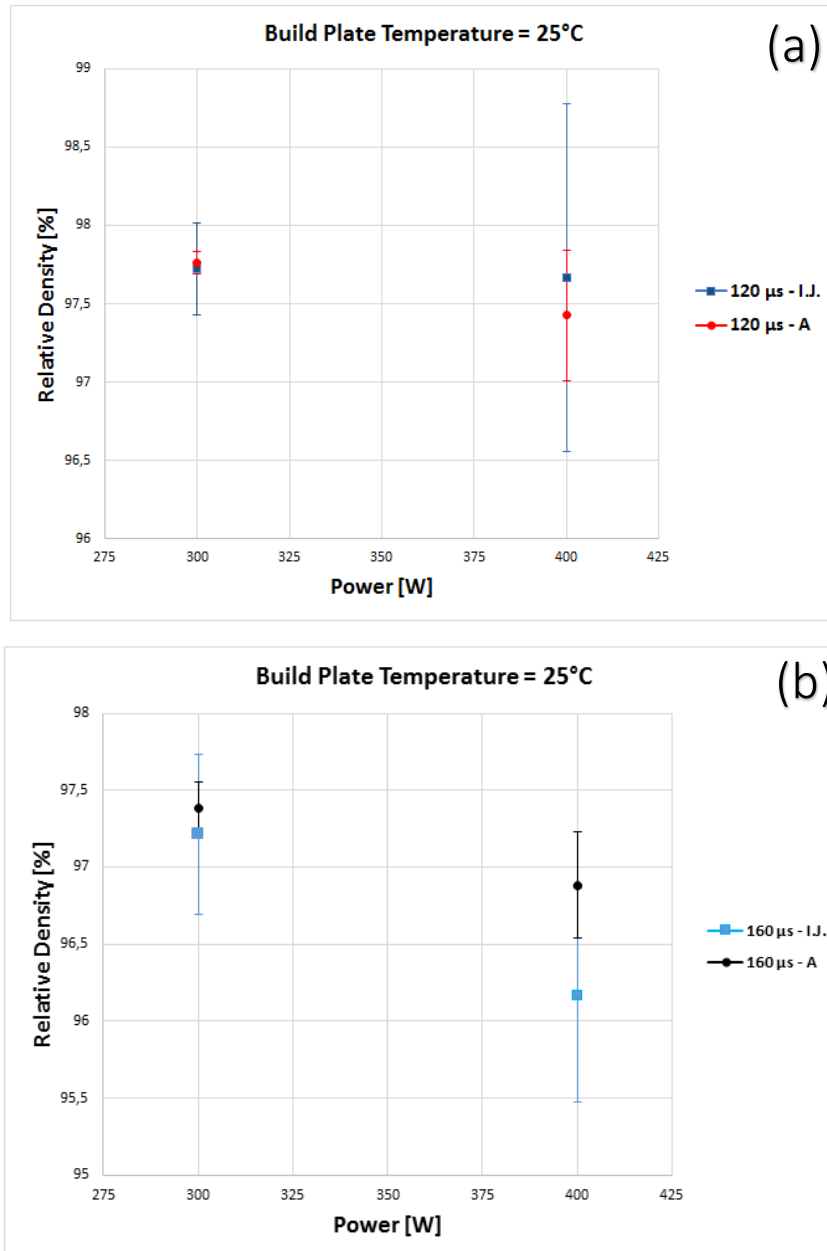
Fig.4.19: Comparison between relative densities resulting from two types of analyses and referred to the build plate temperature equal to 25°C. "I.J." indicates the analysis performed with Image J software while "A." stay for Archimede test. Between figure (a) and figure (b) the exposure times vary.
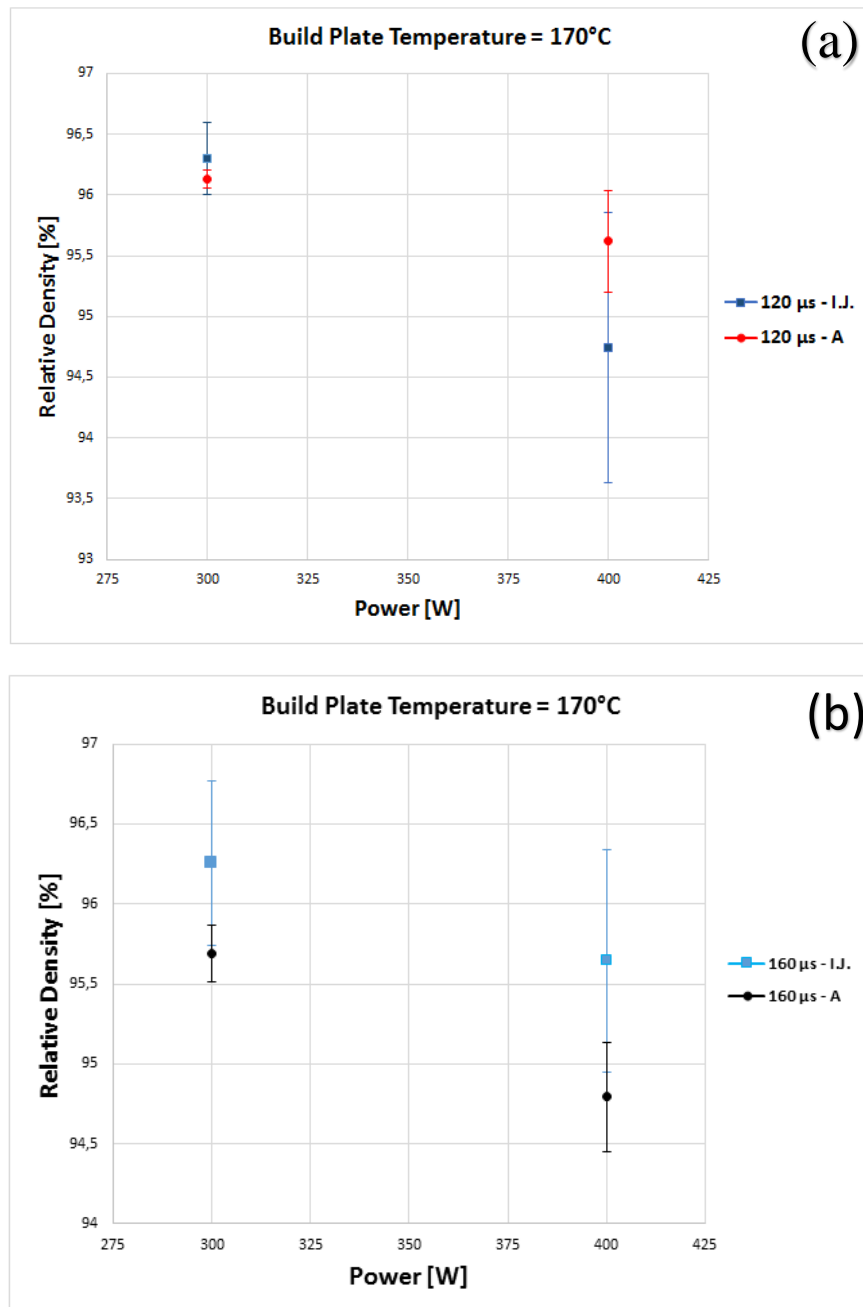
Fig.4.20: Comparison between relative densities resulting from two types of analyses and referred to the build plate temperature equal to 170°C. "I.J." indicates the analysis performed with Image J software while "A." stay for Archimede test. Between figure (a) and figure (b) the exposure times vary.

Observing the samples surfaces by using the microscope it was also possible to see that some gas bubbles, visible as larger pores, were trapped during the solidification process occurring in laser melting of the material (Fig.4.21). The process stability plays a fundamental role in the porosity formation: the entrapment of the gas bubbles could result from an unstable scan track, because the vapor formation process is not uniform in the material (E.O. Olakanmi, 2015). In this cases, the increasing of the energy density induced in the material caused the progressive enhancement of the process instability and the surface turbulence flow. As explained by Olakanmi E.O. *et. al* (2011), the surface turbulent flow of liquid metal in the molten pools can determine the gas entrapment into the liquid metal. The gas species could be vapor, shielding gas, or their combination.
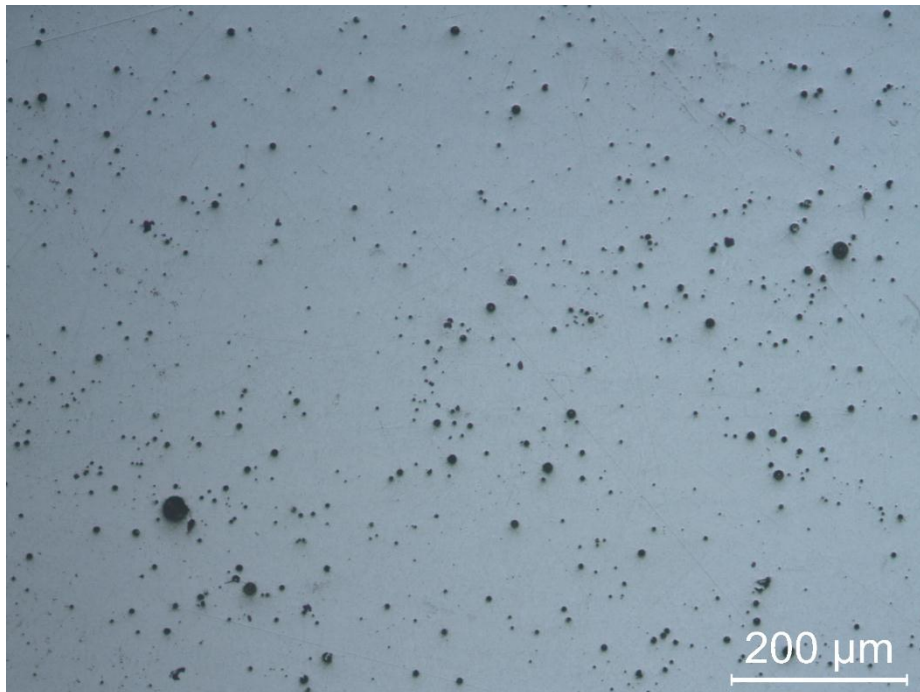
Fig.4.21: Gas bubbles entrapment during laser melting process. (Power300W, Exposure Time=160μs and Build Plate Temperature=25°C)

In Fig.4.22, it is illustrated a particular case, in which the biggest gas bubbles were trapped near the border. Other samples present similar cases. However it is important to remember that the *Border* process parameters are different from the *Fill Hatch* ones.
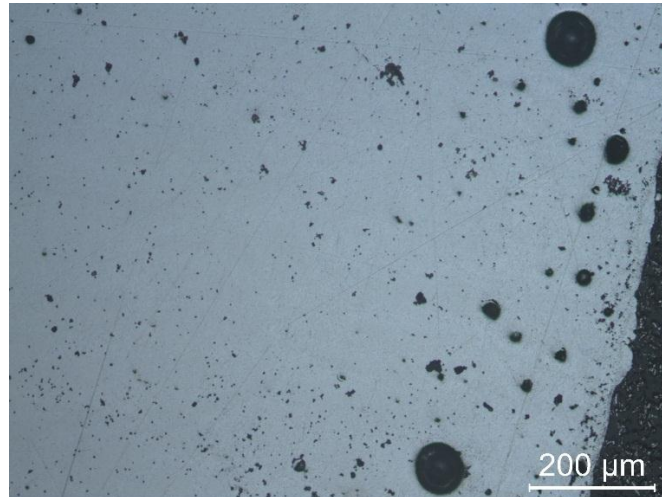
Fig.4.22: Big gas bubbles trapped during the Laser Melting process in the Border zone of the sample. (Power = 400W, Exposure Time = 160µs and Build Plate Temperature 25°C).

During inspection of the samples sections, different geometric shapes of defects typical of the Laser Melting process were found (Fig.4.23). The imperfection can be a type of porosity following shrinkage occurring during the solidification process or a consequence of inadequate metal feeding or rapid solidification (E.O. Olakanmi, 2011).
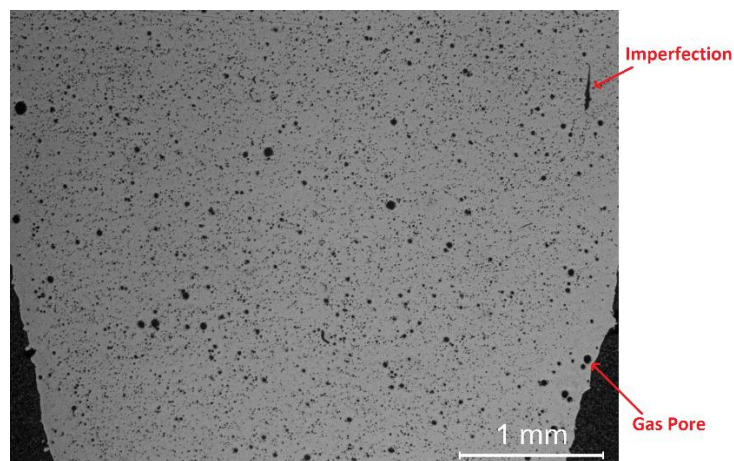
Fig.4.23: Shape of defects produced via Laser Melting. (Power = 400W, Exposure Time = 160µs and Build Plate Temperature = 25°C).

4.2.2) Microstructure Analysis

Laser melting is a process characterized by rapid solidification, due to high thermal gradients, and high cooling rates. These factors can lead to a non-equilibrium solidification and lattice distortion. For these reasons, unexpected microstructure may develop and cause laser melted parts to have different mechanical properties and perform differently from conventionally produced parts. The effects of the laser melting process on the microstructure of the samples have been studied in this section.

The Fig.4.24 represents the typical morphology of Laser Melted parts, along the build direction, with overlapping of the melt pools (region delimited by red line), that is responsible for the partial re-melting of the material (region delimited by yellow line). One of the process parameters that could affect the re-melting phenomenon is the hatch spacing (I. Rosenthal, 2014).
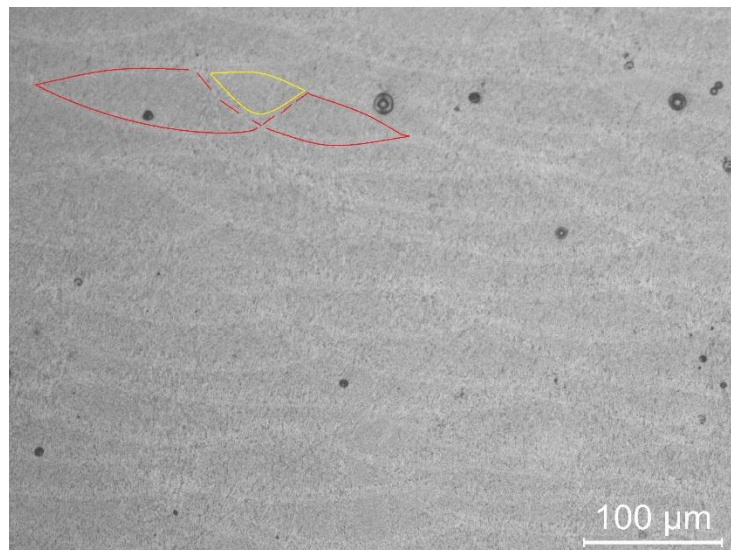
Fig.4.24: Typical microstructure morphology of Laser Melted parts. The red lines define the scan region, while the yellow one the overlapping region (where partial re-melting of the material occurs). Process parameters: 300W, 120µs and 170°C.

During the build process, the combined effects of directional cooling and rapid solidification induced by repeated thermal cycles have a profound influence on the microstructures of the alloy. In Fig.4.25, it is possible to see the microstructure evolution (along the build direction) of the α-Al matrix (bright phase) and eutectic Si-particles (dark phase) after the Laser Melting Process.

Three zones are also indicated: the red arrow indicates the melted zone (MZ), which is the interior part of the melt pool, the white arrow indicates the heat-affected zone (HAZ), which corresponds to the boundary of the melt track and the yellow arrow indicates the re-melted zone (RZ). It is possible to note that in MZ (inside the melt pool) it is present a fine microstructure, which depends on the high cooling rate imposed by the laser melting process (I. Yadroitsev, 2013). In HAZ and RZ grain growth has occurred. The grains orientation among the three zones is similar in the HAZ and MZ (along z-axis) in accordance the principle of epitaxial solidification (E.O. Olakanmi, 2015), while it is different in RZ (where no preferential solidification direction is present).
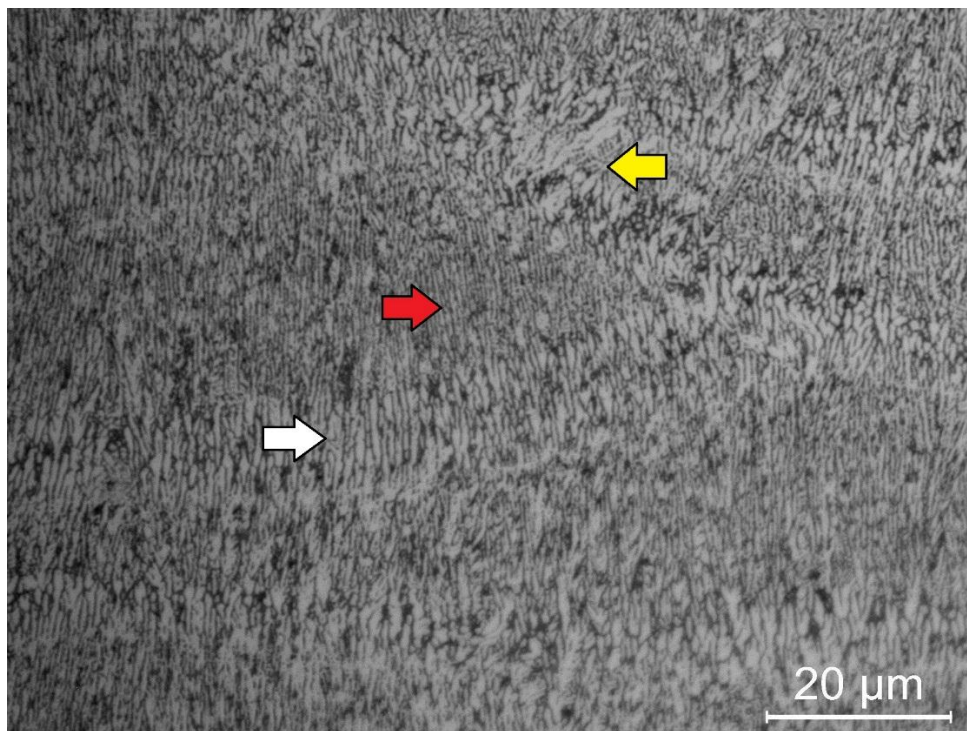
Fig.4.25: Microstructure arrangement of the α-Al matrix (bright phase) and eutectic Si-particles (dark phase). The red arrow indicates the melted zone, the white arrow indicates the heat-affected zone while the yellow arrow indicates the re-melted zone.

Closer investigation of the microstructure of the as-built material, by using the SEM, as shown in Fig.4.26, revealed that it is made up of α-Al columnar grains, with Si segregated at the boundaries. This microstructure is driven by the fast cooling rate that the material experiences during processing (Nesma T., 2016). These type of microstructure is strongly dependent on the processing conditions and it is able to induce in the material an increase of the mechanical properties without performing specific heat treatments.
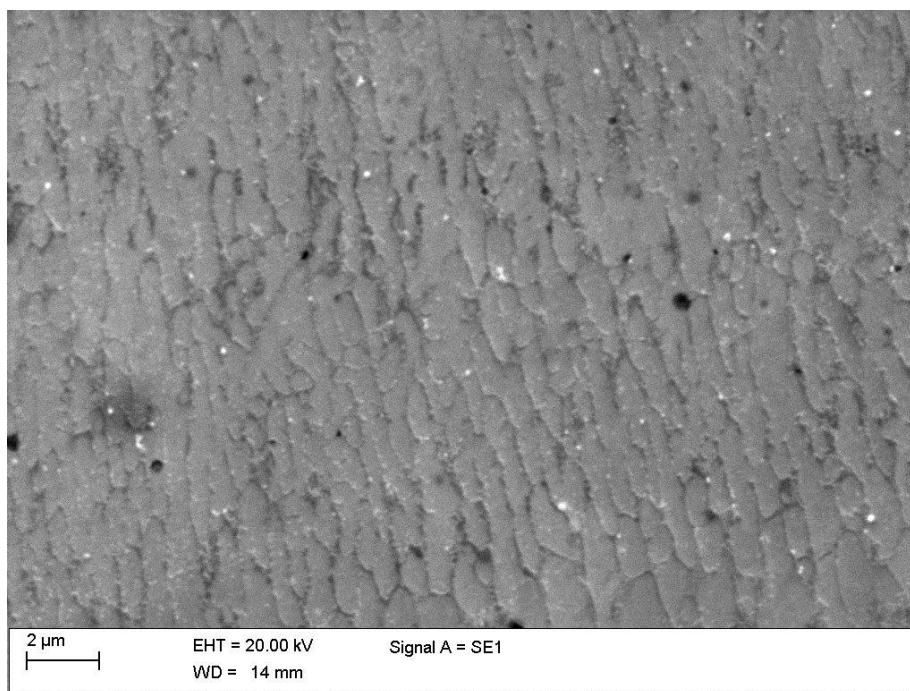
Fig.4.26: SEM image of the microstructure of as-built component showing the α-Al columnar grains, with Si segregated at the boundaries, along the *z*-direction.

Also the plain on which the laser scanning occurred (*x-y* plane), was investigated by SEM analyses. In Fig.4.27 it is possible to observe the microstructure of the as-built sample on *x-y* plane. The melt track is characterized by a cellular microstructure. Also in this case, the α-Al matrix cells decorated with fibrous Si network is visible (Wei L., 2016).
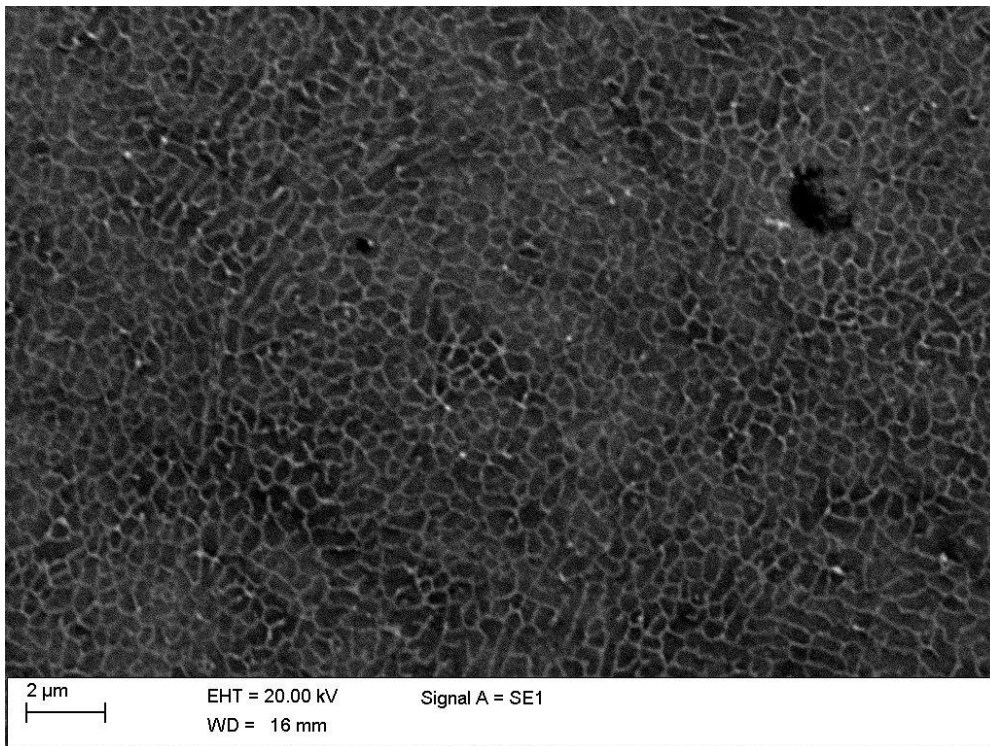
Fig.4.27: SEM image of as-built sample on *x-y* plane.

In Fig.4.28 the HAZ, characterized by the relatively coarser cellular microstructure, and MZ, which exhibits a much finer cellular microstructure, are clearly visible. These zones have experienced different thermal treatments (Li X.P., 2015).
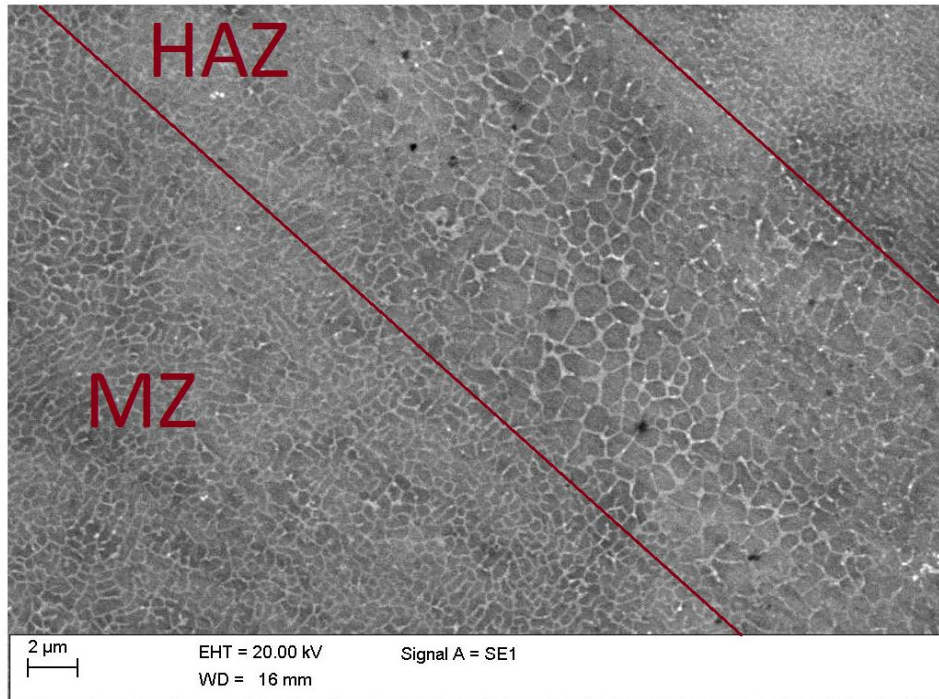
Fig.4.28: SEM image representing the heat-affected zone (HAZ) and the melted zone (MZ).

The fine dispersion of fibrous Si networks in the Al matrix, due to the rapid cooling and solidification induced by the laser melting process, has a positive effect on the mechanical properties of a-built sample conferring to it the high hardness typical of the laser melted parts (K. Kempen, 2012), as it will be investigated in the next chapter.

4.2.3) Micro-Hardness Analysis

The previous study shows that AlSi10Mg samples with an extremely fine microstructure and hence a high hardness can be made via laser melting. The high thermal gradients at which the material is submitted during the process lead to a very fine microstructure making possible to reach high level of hardness (up to 114 HV), without the application of a precipitation hardening treatment. Furthermore, this characteristic could be strongly dependent on solidification conditions and hence on the process parameters.

Being the material hardness a mechanical property strongly dependent on the microstructure, hence on the processing conditions, it becomes object of interest to study how by varying power, exposure time and build plate temperature, this parameter varies. In this chapter, the results related to the micro-hardness analyses are illustrated. The Fig.4.29 and Fig.4.30 show the effects of the process conditions on the hardness of laser melted samples. The results are the average of 5 measurements of each section. High power and short laser-material interaction times determine high temperature gradients together with high cooling rates, resulting in a fine microstructure and high hardness. A strong reduction of this mechanical property occurs between two build plates with the increasing of the pre-heating temperature. A statistical analysis of the results has been performed in order to better understand the influence of each process parameter on this mechanical property.
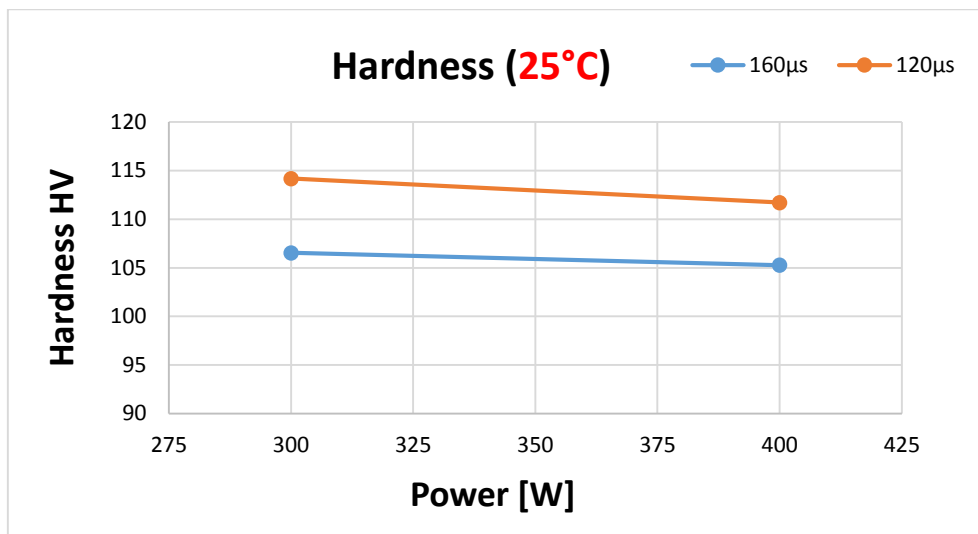
Fig.4.29: Variation of the hardness according to the process conditions without considering the pre-heating (25°C).
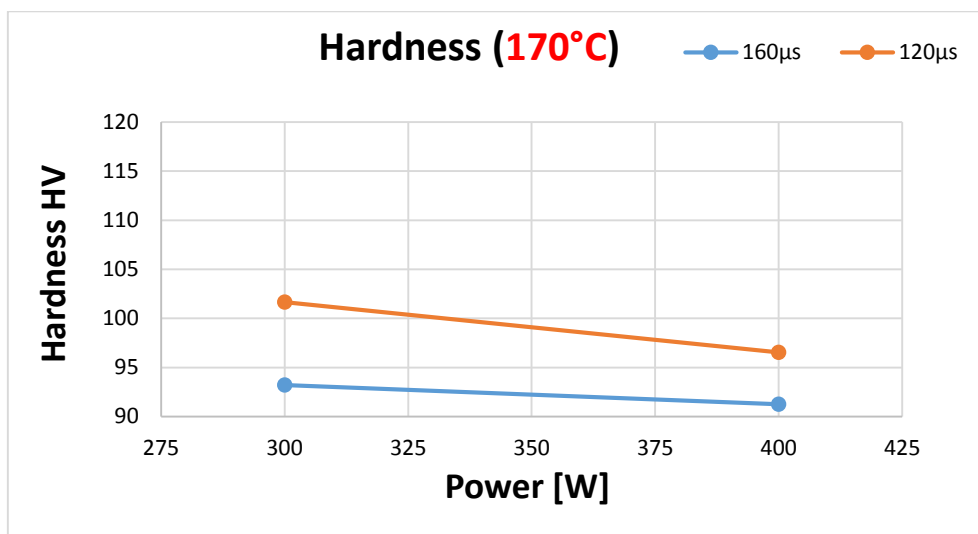
Fig.4.30: Variation of the hardness according to the process conditions considering the pre-heating (170°C).

After that, in order to study the possible correlation between process parameters and the samples hardness a statistical analysis has been performed, using the Minitab software.

In Fig.4.31, the interval plot of the hardness is illustrated. Both the means value of the hardness according to each process parameter combination, and the confidence interval of each measurement are visible. Considering at first the build plate at room temperature (blue squares), although the means appear to be different, the interval bars are overlapped between them, hence the difference is probably not significant. As far as the preheated build plate is concerned, no overlapping between interval bars occurs, in particular increasing the Exposure Time, and hence it means that the difference between the means is significant.
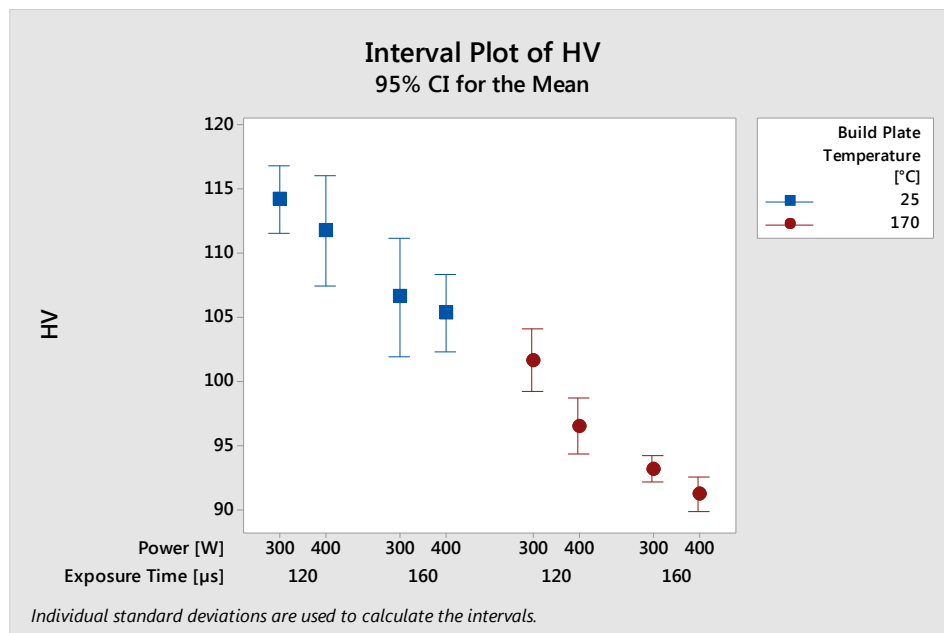
Fig.4.31: Interval Plot of Hardness for each process parameter combination (Power, Exposure Time and build plate Temperature).

It seems that an increasing of the build plate temperature is the main cause of the hardness reduction. For this reason, a further study has been performed with the help of the main effects plot.

In this case, the effects of each process parameter on the resulting hardness is evaluated as distinct. The effect is considered as the difference between the means (dashed line) and the reference line. The Fig.4.32 illustrates that the lower effect on the hardness is given by the Power, while the main effect on it is given by the build plate temperature. This result confirms the hypotheses made after the interval plot, in which the resulting hardness is mainly dependent on in the build plate temperature. Similar outcomes were found by Damien Buchbinder *et.al* (2014), who have studied the effect of the pre-heating on the microstructure of laser melted AlSi10Mg parts. They have found that during preheating significant coarsening of the dendrites occurs, due to slower solidification (smaller cooling rate) and these effect have a strong influence on the hardness, which decreases.
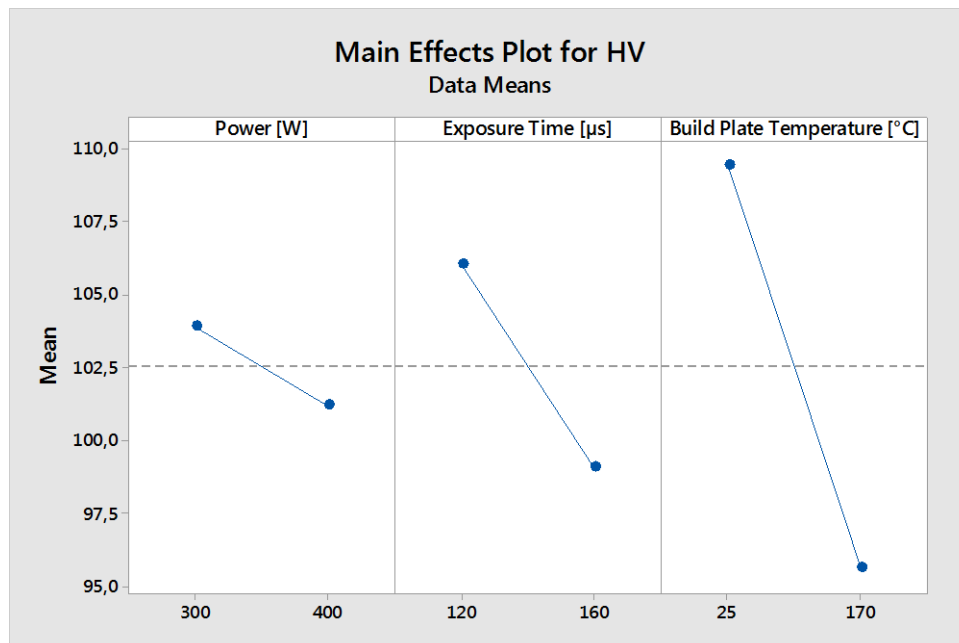
Fig.4.32: Main Effect Plot for HV. The Build Plate Temperature has the main effect on the resulting hardness.

A further analysis (the interaction plot) has been performed to better understand how the process parameters interact between them analyzing also the effects of the interaction on the resulting hardness. The results show different types of interactions (Fig.4.33). It is possible to observe that analogous plots are present for all the conditions. In these plots the lines are almost parallel and this means that no interaction, between these combination of factors and the hardness, occurs.
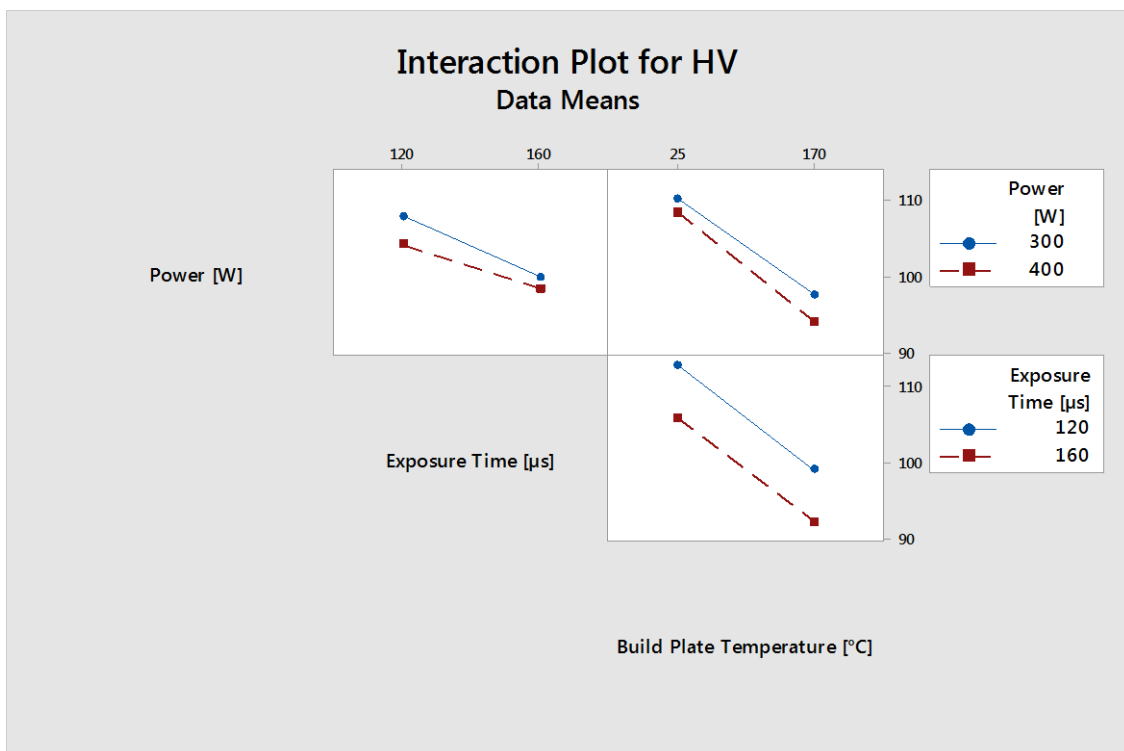
Fig.4.33: Interaction Plot of the Hardness. The parallel lines indicate that no interaction between the considered variables is present.

As done for the statistical analysis of density, also in this case the ANOVA for HV (Tab.4.5) has been evaluated to see the influence of each process parameters on the sample hardness. The interactions between them are not influential (multiplied factors) on the final hardness, while considering the process parameters as distinct they are all significant (look at the p-values).

Tab.4.5: ANOVA for HV.

```
Source                          DF      SS      MS   F-value  P-value
Power [W]                        1   72,90   72,90    12,95    0,001
Exposure Time [µs]               1  483,02  483,02    85,79    0,000
Build Plate Temperature [°C]     1 1893,38 1893,38   336,26    0,000

Power [W]*Exposure Time [µs]     1   11,88   11,88     2,11    0,156
Power [W]*                       1    7,06    7,06     1,25    0,271
  Build Plate Temperature [°C]

Exposure Time [µs]*              1    0,08    0,08     0,01    0,905
  Build Plate Temperature [°C]

Power [W]*Exposure Time [µs]*    1    2,40    2,40     0,43    0,518
  Build Plate Temperature [°C]

Error                           32  180,18    5,63
Total                           39 2650,90

S = 2,37289   R-Sq = 93,20%   R-Sq(adj) = 91,72%
```

As conclusion of the statistical analysis, it is possible to state that the hardness is dependent on the process conditions. The reduction of the hardness is strongly dependent on the increasing of the build plate temperature, which could trigger significant coarsening of the dendrites, due to slower solidification. The maximum micro-hardness founded was 114 $HV_{2,94/15}$ selecting 300W, 120µs and no preheating, while the minimum one was 90 $HV_{2,94/15}$ selecting 400W, 160µs and preheating at 170°C.

4.2.4) Analysis of the Compositional Stability of the Alloy

In this paragraph the chemical composition investigations of AlSi10Mg samples is reported and discussed. The control of the mean chemical composition of the fabricated sample was performed by using the EDS.

For each sample, three sites along the z axis were investigated, each site was divided in four areas calculating the atomic percentage content of Al, Si and Mg together with the mean value and the standard variation. The sample selected for the analysis were those fabricated considering the minimum/maximum fabrication conditions. In particular, they were those fabricated imposing the following parameters:

- Power = 300W, Exposure Time = 120μs and Build Plate Temperature = 25°C;
- Power = 400W, Exposure Time = 160μs and Build Plate Temperature = 25°C;
- Power = 300W, Exposure Time = 120μs and Build Plate Temperature = 170°C;
- Power = 400W, Exposure Time = 160μs and Build Plate Temperature = 170°C;

In Fig.4.34, an example of site investigation is illustrated. The site is divided into four areas and then the chemical composition calculation starts. The three selected sites are respectively located in the upper part, in the middle and in the lower part of the surface, considering the build direction (z axis). The result of EDS analysis is the spectrum x-ray counts vs. energy (in keV). The Fig.4.35 EDS represents an example of AlSi10Mg spectrum, containing detectable Al, Si and Mg.
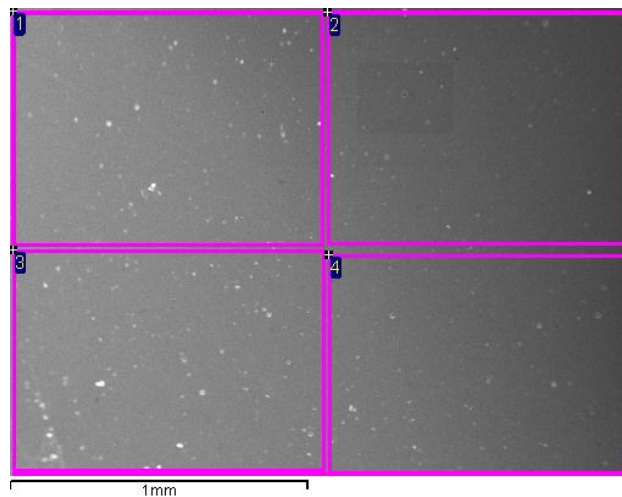

Fig.4.34: Example of chemical composition analysis. The site is divided in four areas and for each area the chemical composition is calculated.
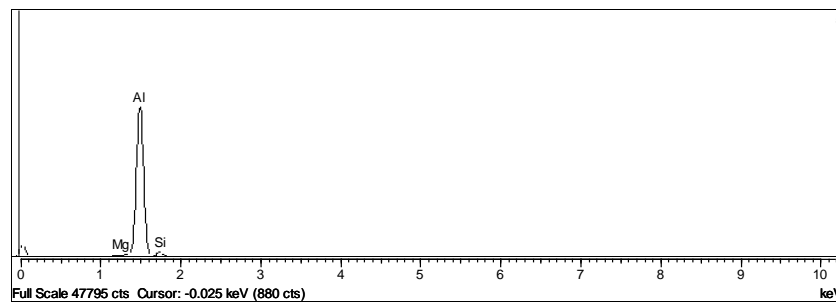
Fig.4.35: Example of EDS spectrum x-ray counts vs. energy (in keV). EDS spectrum of AlSi10Mg, containing detectable Al, Si and Mg.

The Tab.4.6 shows the chemical composition variation for each sample by varying the process parameters.

Tab.4.6: Atomic percentage content of Al, Si, Mg by varying the process parameters.

Process Conditions	Mean Al [at.%]	Mean Si [at.%]	Mean Mg [at.%]
300W-120μs-25°C	90,8	9,0	0,2
400W-160μs-25°C	90,6	9,2	0,2
300W-120μs-170°C	90,8	9,0	0,2
400W-160μs-170°C	90,6	9,2	0,2

The Mg content could be difficult to detect in the SEM–EDS analysis due to its very low initial weight percentage in AlSi10Mg alloy. Although Mg is an element, which does not affect the melting and solidification behavior of the material, the effect of the precipitate formation and consequently mechanical properties will be further investigated.

Observing the results related to the Al, Si and Mg contents, it is reasonable to state that the variation of the process parameters does not determine any variation of the chemical composition of the laser melted sample. This is not a trivial result; in fact, the laser melting is a process that induces very high gradient of temperature in the material during the interaction with the laser beam. The instability of the scan track due to very high energy density, can trigger vaporization phenomena of the lightest elements present in the alloy. Nesma T. *et.al* (2011) during the Energy Dispersive Spectroscopy (EDS) analysis of AlSi10Mg laser melted parts, discovered a significant difference between the chemical composition of the as-built sample and the initial powder, in the amount of Mg. The as-built sample showed a reduction in Mg content to almost the half of its original

value.

They reported that the cause of this reduction could be associated to the evaporation of Mg during the laser melting process, being the lightest element, as a response to the high energy density induced in the sample by using small hatch spacing.

However, further analyses have been performed on the same samples to ascertain that no change in chemical composition of fabricated sample occurred by varying the process parameters. For this purpose, DTA measurements were performed to see if any variation in melting temperature occurred between different samples.

In Fig.4.36, an example of complete DTA measurement is presented considering both the heating and cooling cycles.
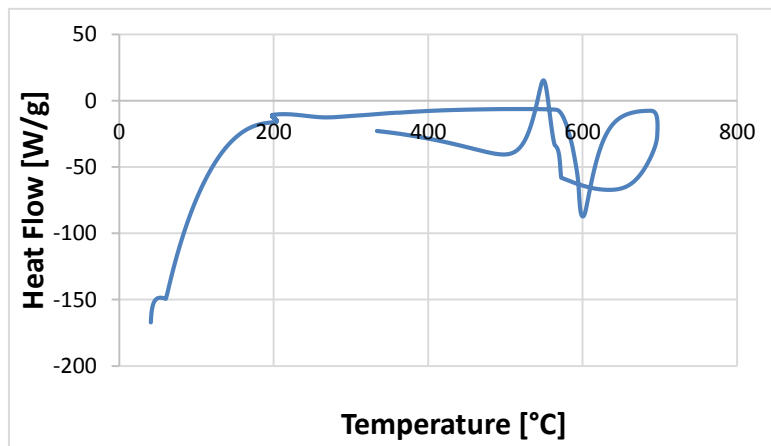
Fig.4.36: DTA of AlSi10Mg sample (300W, 160μs and 25°C).

All DTA patterns present the characteristic peak related to the melting point of AlSi10Mg alloy, as illustrated in Fig.4.37.
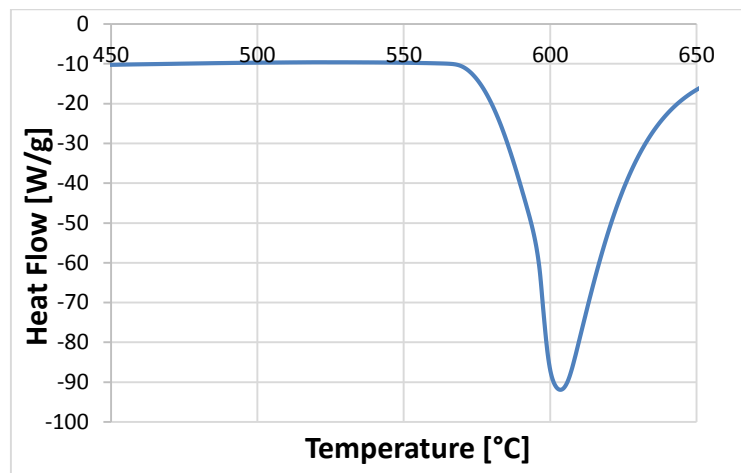
Fig.4.37: DTA measurement representing the characteristic peak related to the melting point of AlSi10Mg (300W, 120μs and 25°C).

For each sample, the onset point and the maximum temperature of the melting peak were calculated. The results are resumed in Fig.4.38, where it is also possible to see that no big differences were found at varying of process parameters. This consideration is in accordance with what found in chemical composition analyses where no variation of Al, Si and Mg contents occurred among different process conditions. As far as the enthalpy of fusion is concerned, it shows a variation among different process parameters, as illustrate in Fig.4.38 (e) and (f), although the DTA curves do not show any difference in shape. It is possible to notice that, in preheated build plate (Fig.4.38 (f)), the enthalpy of fusion increases with increasing the Power. These results were also compared with that of the fresh powder (see the chapter of powder characterization), whose enthalpy is equal to 419,1 J/g and it is included in the range of the as built samples enthalpies (hence no variation occurred).
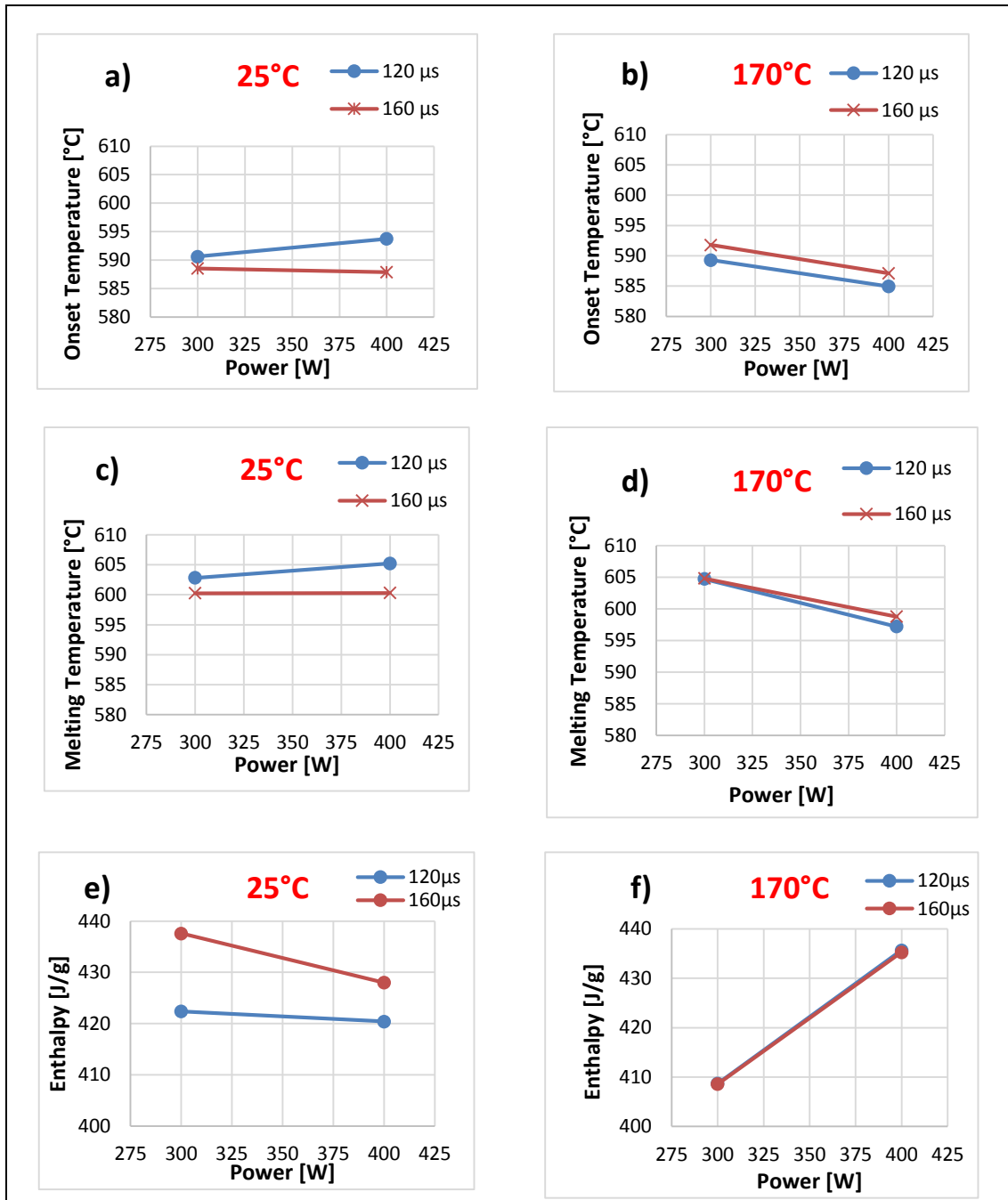
Fig.4.38: Enthalpy, melting, onset temperatures variation considering different process parameter combinations.

The independence of the melting point from the process conditions was also confirmed comparing the DTA measurements of the AlSi10Mg powder with that of as built samples where no difference in melting temperature was found, almost 598°C (Fig.4.39), although the curve of laser melted sample present a hump before the fusion. This hump could be associated to the anticipated melting of an intermediate phase, formed during the process.
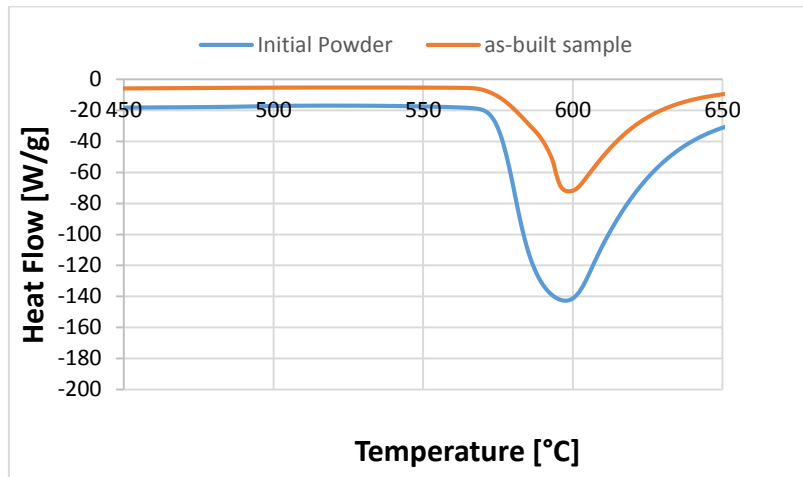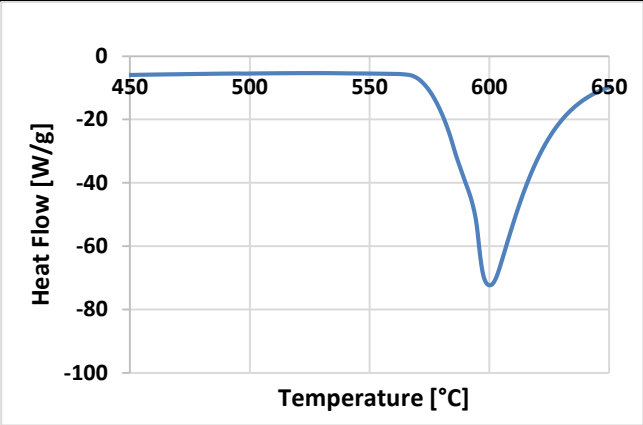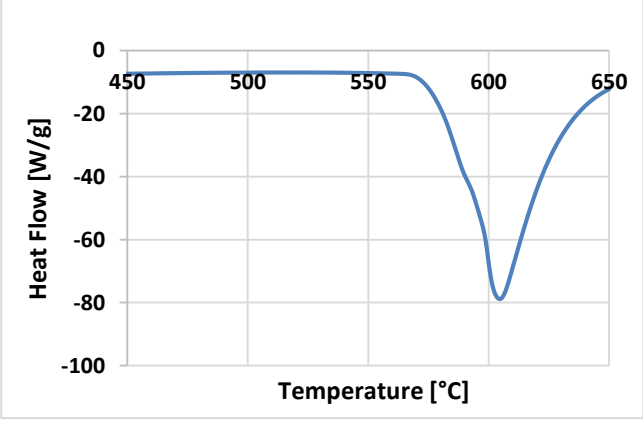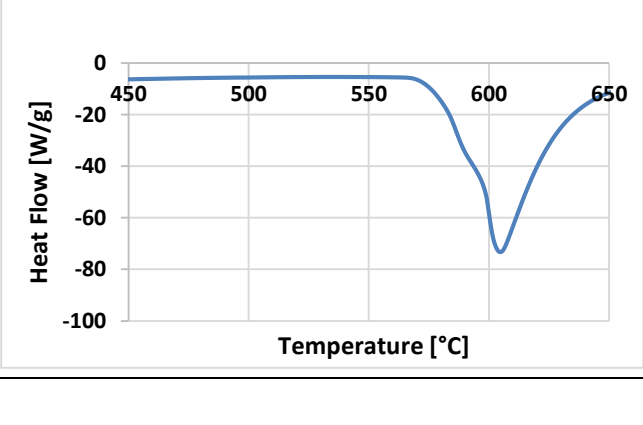
Fig.4.39: DTA comparison between initial powder and as-built sample.

In Tab.4.7, the peaks related to the melting of all analyzed samples are represented. No variation in onset temperature and melting temperature are visible.

Tab.4.7: DTA curves related to the process parameters.

Power [W]	Exposure Time [μs]	Build Plate Temperature [°C]	DTA Curve
300	120	25	
300	160	25	
400	120	25	

400	160	25	
300	120	170	
300	160	170	

400	120	170	
400	160	170	

Resuming, no variations in the melting temperatures of samples, fabricated imposing different process parameters, occurred. This confirms the results related to the EDS analyses in which no variation in chemical composition was observed. However, further thermal analysis by using the DSC have been performed to understand the heat evolution in different samples, as explained in next chapter.

4.2.5) DSC Analysis

The DSC analysis has been performed using Seiko SSC/5200 equipped with a liquid nitrogen cooling system. The main objective of this analysis was to analyze if any phase transformations and/or precipitation phenomena occurred during thermal cycling. The same samples submitted to the DTA analysis were also submitted to the DSC analysis. In Fig.4.40, an example of a typical DSC curve (heating and cooling) of an AlSi10Mg sample is represented (Power = 300W, Exposure Time =160µs and Build Plate Temperature = 25°C).
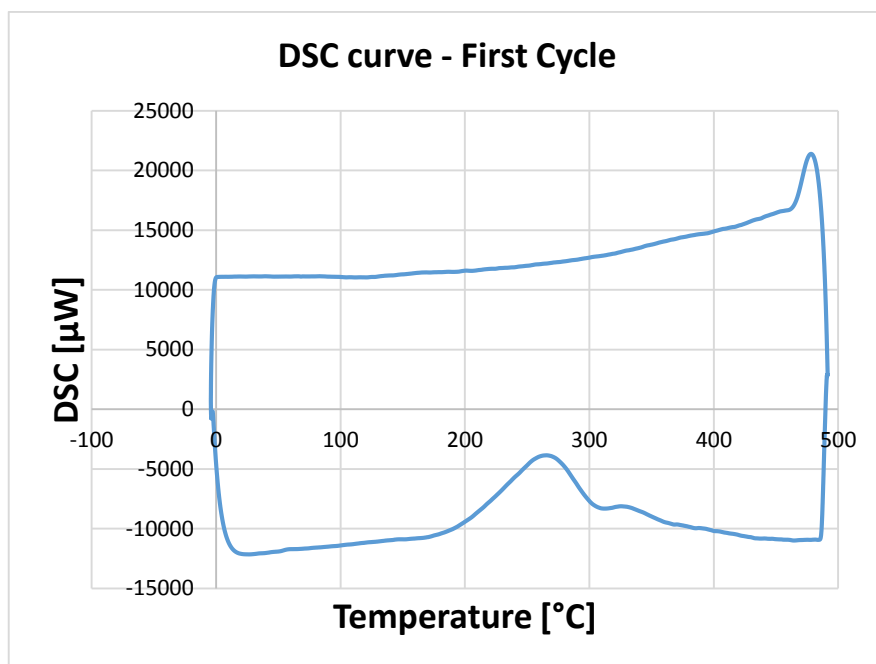
Fig.4.40: DSC curve of AlSi10Mg sample (Power = 300W, Exposure Time = 160µs, Build Plate Temperature = 25°C).

For all samples, a second DSC heating-cooling cycle (Fig.4.41) was performed in order to see if further transformations occurred. The results showed that the reaction peaks disappeared.
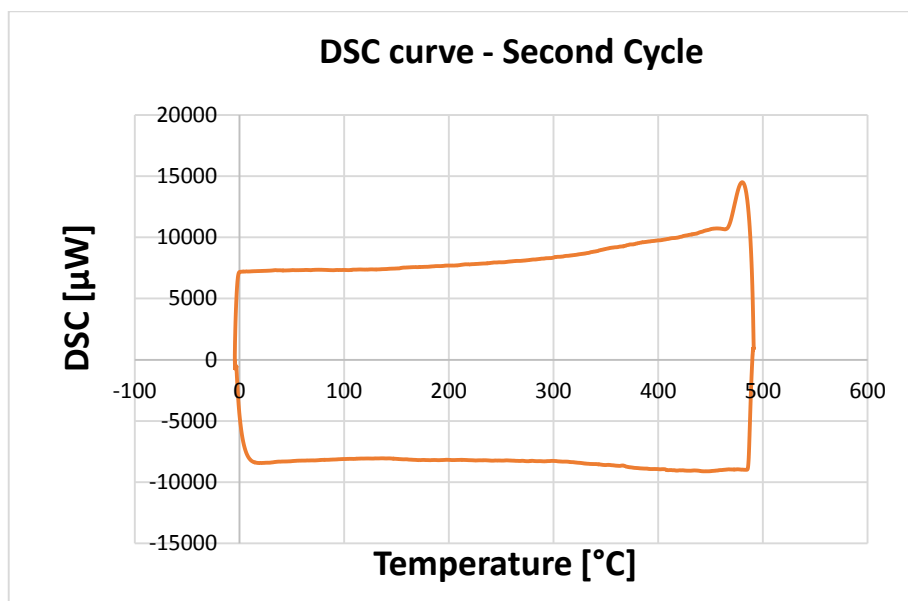
Fig.4.41: DSC curve showing the disappearance of the reaction peaks during the second heating cooling cycle.
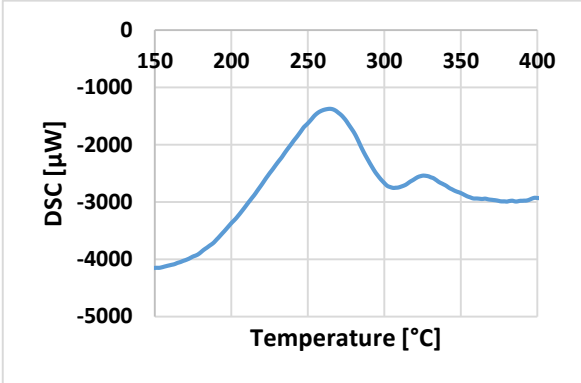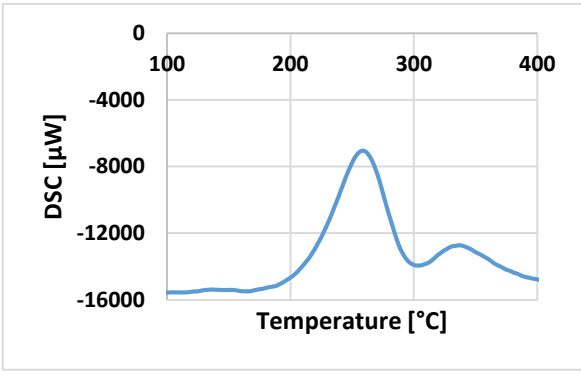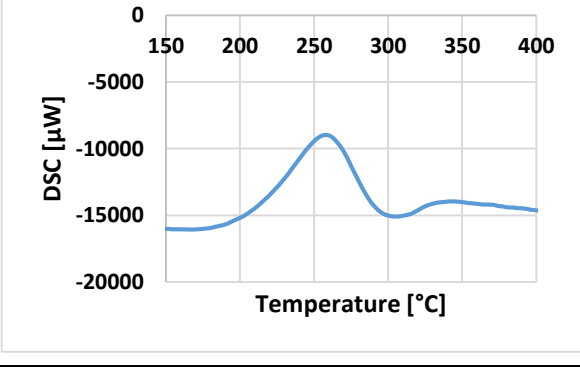
All the DSC curves show two exothermic reactions; the first peak varies between 252,6°C and 265,9°C, while the second one varies among 322,9°C and 389,6°C (as illustrated in Tab.4.8). It has been object of interest to understand the nature of these two exothermic transformations.

In heat treatable Al based alloys, the heat effects due to vacancy annihilation, recovery and recrystallization are generally much smaller than the effects due to precipitation or dissolution of precipitates, and they generally occur in overlapping temperature ranges. Hence, the exothermic heat effects due to vacancy annihilation, recovery and recrystallisation can often not be determined in heat treatble Al based alloys. In deformed alloys for which no precipitation or dissolution reactions occur (pure Al or diluite non-heat-treatable alloys) recovery and recrystallization might be detectable with DSC (M.J. Starink, 2004).

As first analysis, in accordance with the previous consideration, the first transformation, which is the biggest, could be related to the phenomenon of the precipitation while the second transformation, whose range of temperature is overlapped to that of the previous one and which is smaller than the first one, could be related to a recovery phenomenon.

Tab.4.8: DSC curves related to the process parameters.

Power [W]	Exposure Time [μs]	Build Plate Temperature [°C]	DSC Curve
300	120	25	
300	160	25	
400	120	25	

400	160	25	
300	120	170	
300	160	170	

400	120	170	
400	160	170	

Focusing the attention on two exothermic reactions, considering the peaks related to the first transformation, no big differences have been found (in terms of peak temperature and enthalpy) by varying the process conditions, as illustrated in Fig.4.42 (a) and (b). This could mean that it is an exothermic reaction dependent on the material properties, and typical of the Al-Si-Mg alloys, instead of the process conditions. On the contrary, considering the second transformations, it is possible to observe that they tend to shift towards higher ranges of temperature with increasing the energy input and hence the Power and Exposure Time, together with Build Plate Temperature, as illustrated in Fig.4.42 (c) and (d). This result could mean that the second exothermic reaction could be associated to the fabrication process.
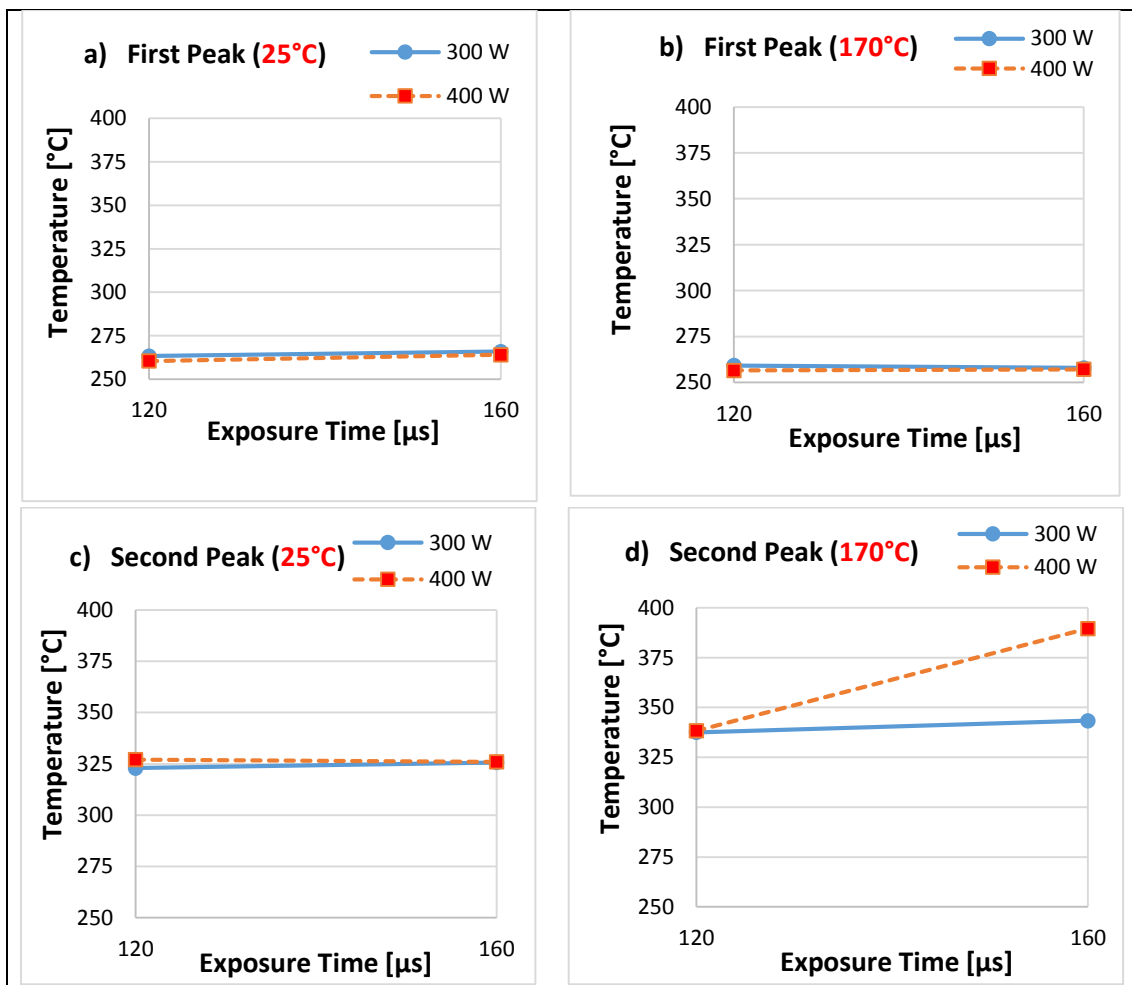
Fig.4.42: Temperatures variation of the two exothermic reactions by varying the process conditions. Figure (a) and figure (b) are associated to the first transformation considering two different build plate temperatures (25°C and 170°C), while figures (c) and (d) to the second transformation.

In order to evaluate the possible nature of the second exothermic reaction, the results have been compared with the one related to the initial AlSi10Mg powder, previously illustrated

in the chapter of powder characterization. Also a further DSC scan has been performed on a different aluminum sample produced by casting process, which is the AlSi7Mg alloy (designation EN-AB 42000) having the chemical composition presented in Tab.4.9. This alloy was chosen because of its composition, which is similar to the one of the alloy studied in the present work: this should allow to compare the two alloys and understand whether the heat effects are associated to the alloy itself or to the processing route.

Tab.4.9: Chemical composition of AlSi7Mg

Si (%)	Fe (%)	Cu (%)	Mn (%)	Mg (%)	Cr (%)	Ni (%)	Zn (%)	Pb (%)	Sn (%)	Ti (%)	Other elements (%)	Al
6,5				0,25						0,05		
7,5	0,45	0,15	0,35	0,65	-	0,15	0,15	0,05	0,05	0,20	0,15	rest

Both DSC analyses were performed following the same conditions of the previous measurements, and the resulting curves are showed in Fig.4.43, referred to initial powder and in Fig.4.44, referred to AlSi7Mg alloy.
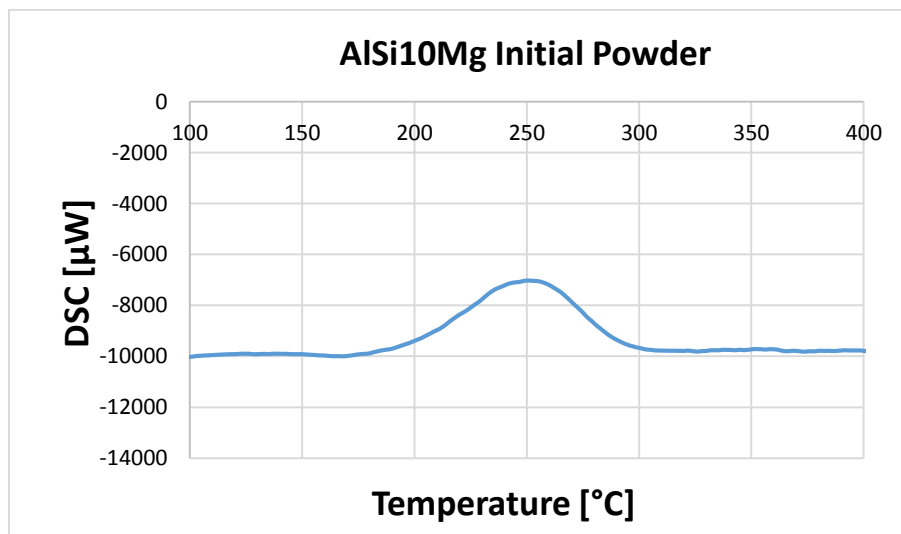
Fig.4.43: DSC measurement of AlSi10Mg initial powder powder.
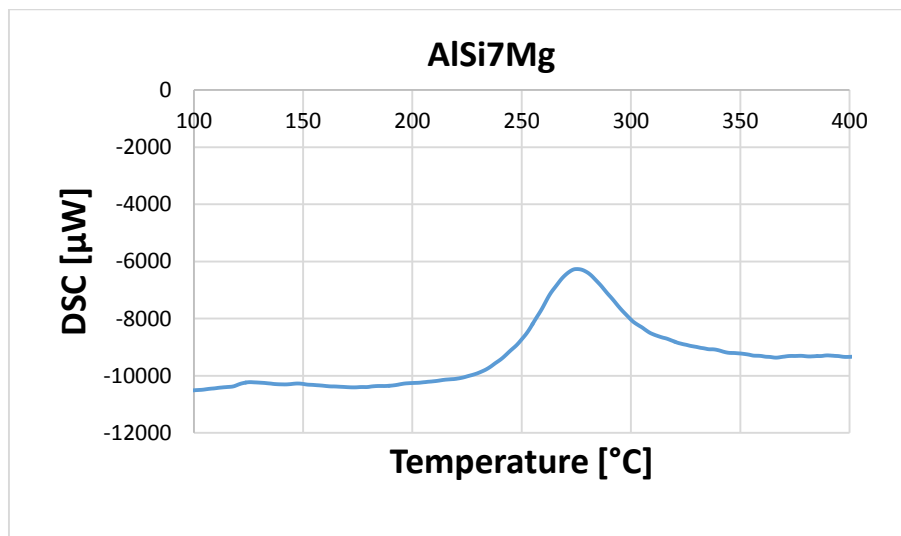
Fig.4.44: DSC measurement of AlSi7Mg alloy subjected to casting process.

The results show that just a single exothermic reaction occurred in both AlSi7Mg sample and AlSi10Mg fresh powder, and they are similar (in terms of onset/offset temperature and shape) to the first peak of DSC of sample fabricated via Laser Melting. In accordance with Maja Vončina *et.al* (2011), this reaction could be associated to the precipitation of Mg_2Si phase that starts at around 210°C. The disappearance of the second exothermic reaction suggests that this latter one is associated to the fabrication process conditions. However further analyses to support these theories were performed.

4.2.6) Isothermal Heat Treatment

In order to better understand the exothermic reactions mechanism and nature of AlSi10Mg alloy, different isothermal heat treatments were performed. The selected sample for these heat treatments is the one having the maximum density, whose fabrication conditions were: Power = 325W, Exposure Time = 120μs and Build Plate Temperature = 25°C. In order to determine the heat treatment temperatures, further DSC analyses imposing different heating rates have been carried out.

Reducing the heating rate the peaks shift towards lower temperatures (as illustrated in Fig.4.45). The different heating rates used were:

- 30°C/min, 20°C/min, 10°C/min, 5°C/min and 2°C/min.
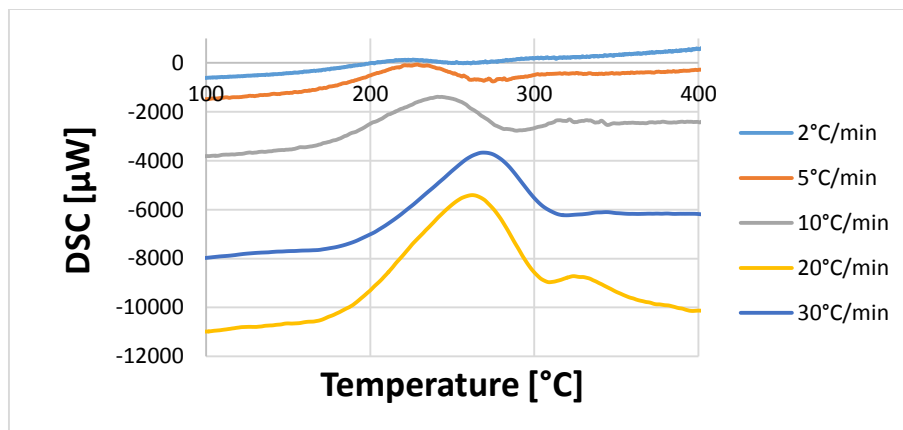
Fig.4.45: Different DSC measurements of AlSi10Mg carried out by varying the heating rates. The peaks translation occurs, making possible to find the two isothermal temperatures to use in heat treatments.

In order to determine the temperature at which the transformations would occur during an isothermal treatment (heating rate: 0°C/min), all DSC curves have been considered and the deconvolution of two peaks was performed by using a statistical software. This operation made possible to better distinguish the two transformations, allowing the calculation of their onset and offset temperatures. Being the offset temperature the condition at which transformation is terminated, this becomes the thermal condition at which the heat treatment is carried out. For this reason, all offset temperatures were plotted and fitted by an exponential regression respectively for each of the two peaks, as illustrated in Fig.4.46 and Fig.4.47.
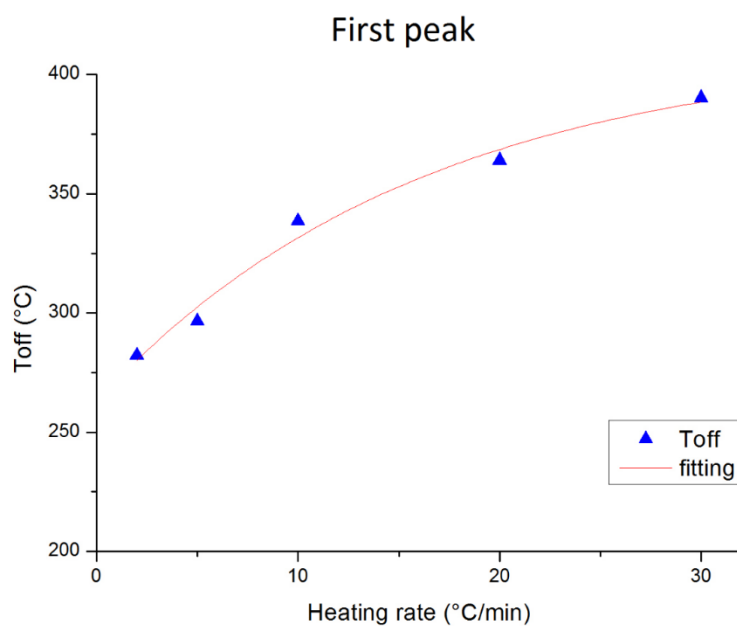
Fig.4.46: Exponential regression of offset temperatures in function of the heating rate considering the Firs Peak.
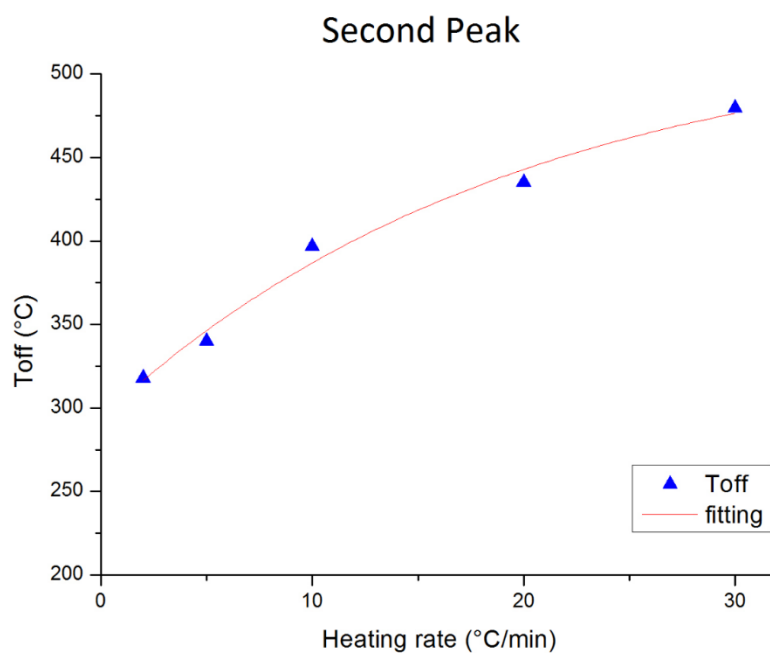
Fig.4.47: Exponential regression of offset temperatures in function of the heating rate considering the Second Peak.

The software uses a statistical parameter (R^2) to indicate the fitting reliability, which can vary between 0 (no reliability) and 1 (highest reliability).

The equation representing the variation of the offset temperature (*y*) as function of the heating rate (*x*), for both exothermic reactions, is:

$$y = A_i * \exp(-x/t_i) + y_i \qquad\qquad i=1,2;$$

where A_i, t_i and y_i are three constant parameters, which vary according to the peak under analysis. The values are represented in Tab.4.10.

Tab.4.10: Constant parameters table of exponential regressions

i=1,2	A_i	t_i	y_i
1	-148,786	16,0812	411,5091
2	-233,313	19,6765	527,332

The degrees of reliability of these equation were estimated to be high: $R^2 = 0,97$ for the first peak, and $R^2 = 0,98$ for the second one. Imposing *x* = 0 (that means heating rate equal to zero), it has been possible to calculate the offset temperatures of two peaks considering an isothermal cycle, and hence the temperatures used for the heat treatments: 263°C for the first peak and 294°C for the second peak.

After offset temperatures determination, isothermal heat treatments were performed in following conditions, on the sample having the maximum density:

- Heat to between 300°C and 320°C, holding for 2h and slow cool (Renishaw condition);
- Heat to between 300°C and 320°C, holding for 30 min and slow cool;
- Heat to 263°C, holding for 2h and slow cool;
- Heat to 263°C, holding for 30 min and slow cool;
- Heat to 294°C, holding for 2h and slow cool;
- Heat to 294°C, holding for 30 min and slow cool.

The treated samples were subjected to hardness tests, SEM and XRD analyses, to see the effect of heat treatments on the microstructure.

In Fig.4.48 the hardness of heat treated samples are represented considering the comparison between different heat treatments and the as-built sample. First of all, it is possible to observe a global reduction of the hardness of heat treated samples with respect the as-built one. Going more in detail, in comparison with the as-built sample, heat treating at 263°C for 30 minutes and 2 hours, results in a decrease of the hardness by almost 11%. However, it is possible to note that the results are similar independently on the two durations. This could mean that no differences in the microstructure occurred among two heat treatments. Increasing the temperature, the hardness further reduces and the effects of the duration on it become more significant. Heat treating at 294°C for 30 minutes and 2 hours, the hardness reductions are respectively by almost 18% and the 27% with respect the as-built sample. Similar results were found by Mertens A. *et.al*, 2015. Further increases of temperature and duration cause a reduction of the hardness by 25% in treated sample at 320°C for 30 minutes, and by 35% in heat treated sample at 320 °C for 2 hours (both compared to the as-built sample).
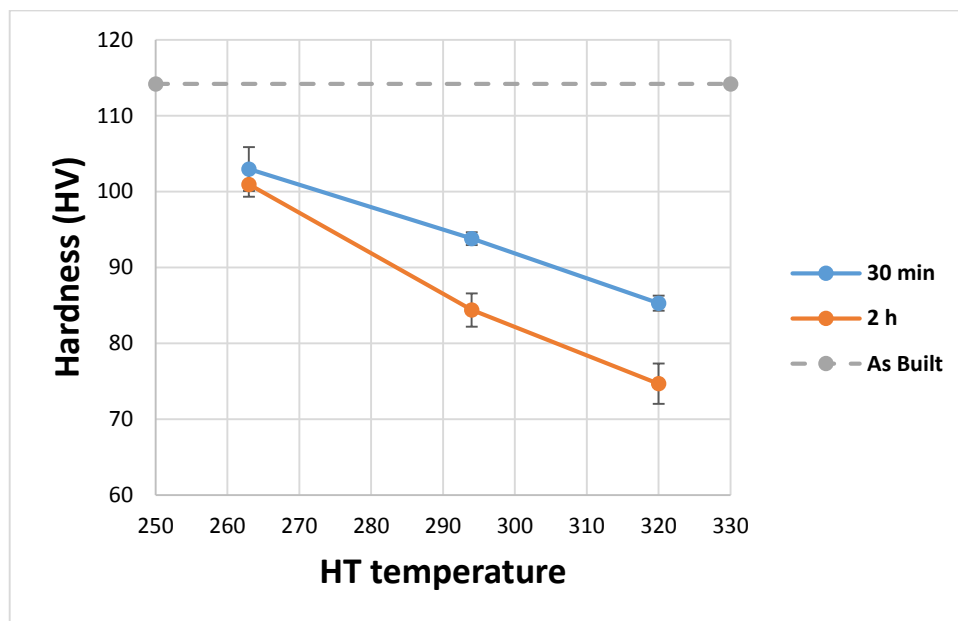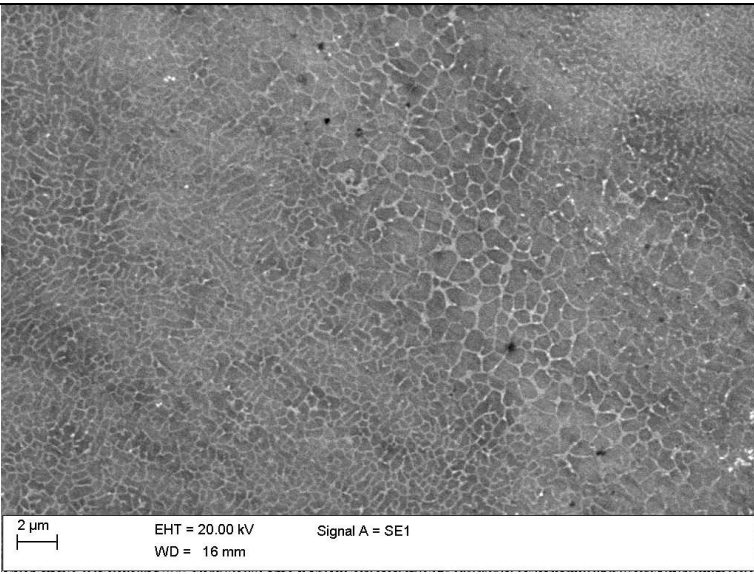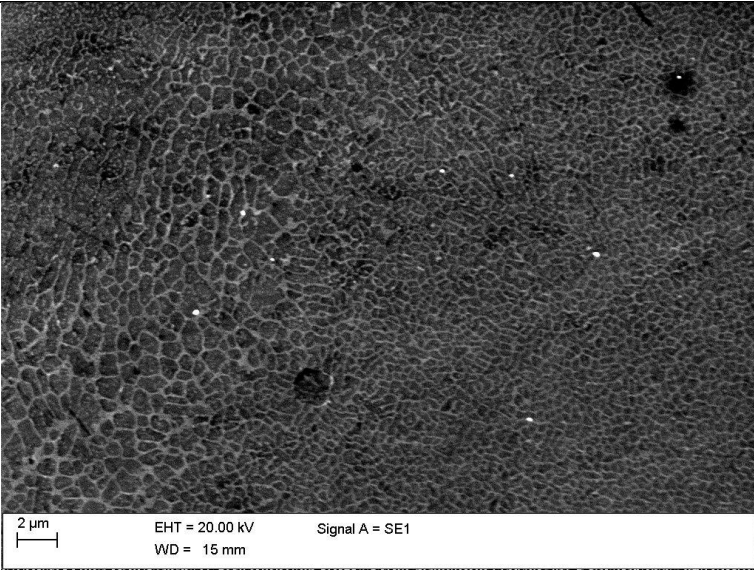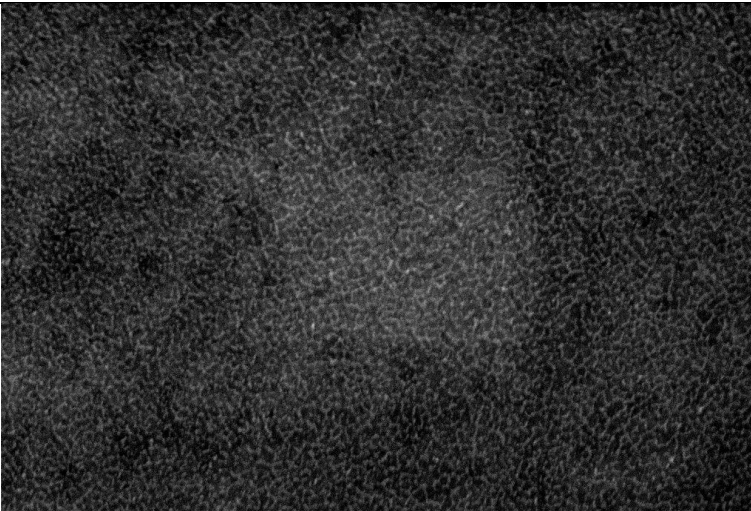
Fig.4.48: Hardness of heat treated samples in different conditions.

Being the hardness a mechanical property dependent on the final microstructure of the material, after the hardness tests, different SEM analyses were performed on the samples subjected to heat treatments with a duration of 2 hours, to see how vary the microstructure among the as-built sample the heat treated ones. All SEM observations have been performed along the scanning plane (*x-y*) and resumed in Tab.4.11.

No big differences in Si particles size and distribution were observed between the as-built sample and the one heat treated at 263°C for 2 hours. The network of Si phase is continuous in both cases. Performing the heat treatment at 294°C for 2 hours the Si phase starts to change morphology and the network becomes discontinuous. At 320°C for 2 hours, the Si particles tend to agglomerate increasing their size.

Tab.4.11: SEM images comparison between untreated and treated samples.

Temperature	Duration	SEM image
As-built		
263 °C	2 h	

294°C	2 h	
320°C	2 h	

The effects of the microstructural change induced by the heat treatment, are in accordance to the resulting hardness of heat treated samples, which shows a reduction with the increasing the temperature and duration of the thermal treatment.

This could be associated to the effect of the network discontinuity combined with the increasing of the Si particles, which are no longer able to limit the dislocation motion as occurred in as-built sample. The SEM images do not exclude the precipitation of Mg_2Si phase during the heat treatments, which is very fine and responsible of the hardness increasing. However, this contribution need to be compared to that of the stress release due to the high temperatures, which can be associated to the reduction of the sample hardness. Being this mechanical property reduced in heat-treated samples with respect the as-built one, it is reasonable to suppose that the effect of the stress release induced thermal treatment is predominant.

Further XRD analyses have been performed to see the effects of the heat treatments on the resulting microstructures, as explained in the next chapter.

4.2.7) XRD Analysis

In this section the diffractograms of AlSi10Mg sample before and after the heat treatment will be analyzed. In general, it is possible to identify different phases in a sample and to give a quantification of them, but also to see effect of different heat treatments on the peaks. The sample used for the XRD analysis is the one having the maximum density, in as-built conditions and after the heat-treatments.

First of all, the XRD analysis was carried out on the as-built sample (Fig.4.49). It mainly consists of α-Al and Si phases and the intensity of Si peaks was relatively lower than that of Al peaks because of the low relative weight percentage. The XRD spectra revealed also the Mg_2Si peak (Fig.4.50).
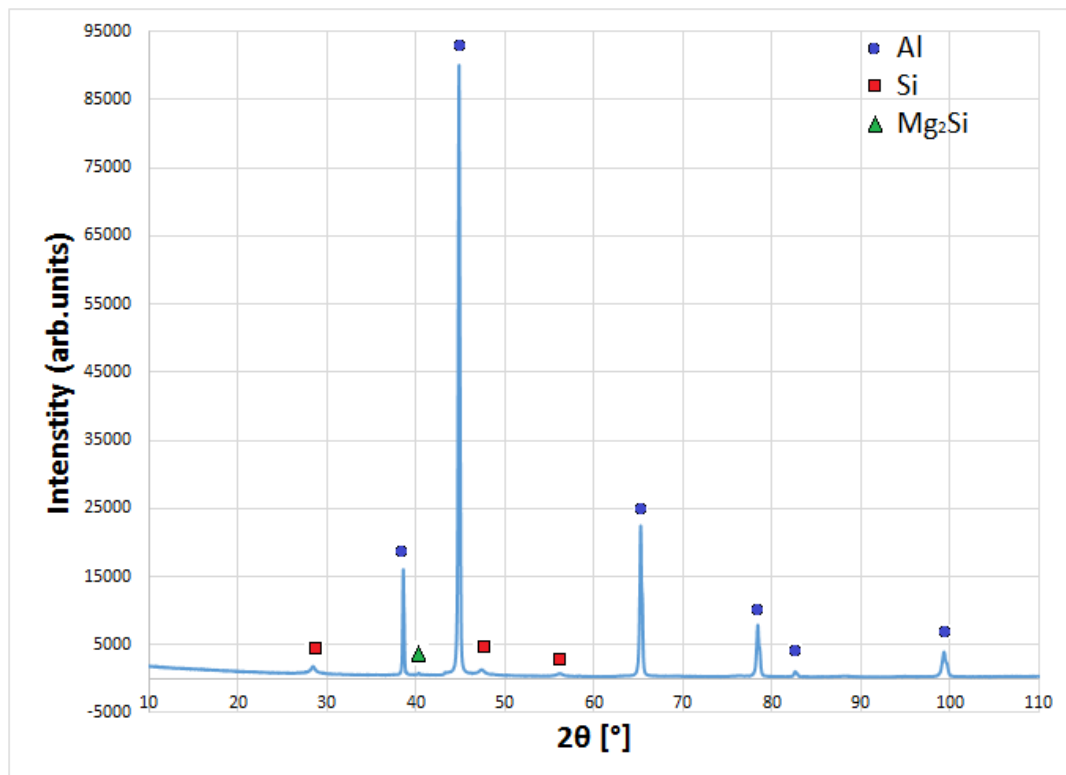
Fig.4.49: XRD peaks of AlSi10Mg as-built samples.
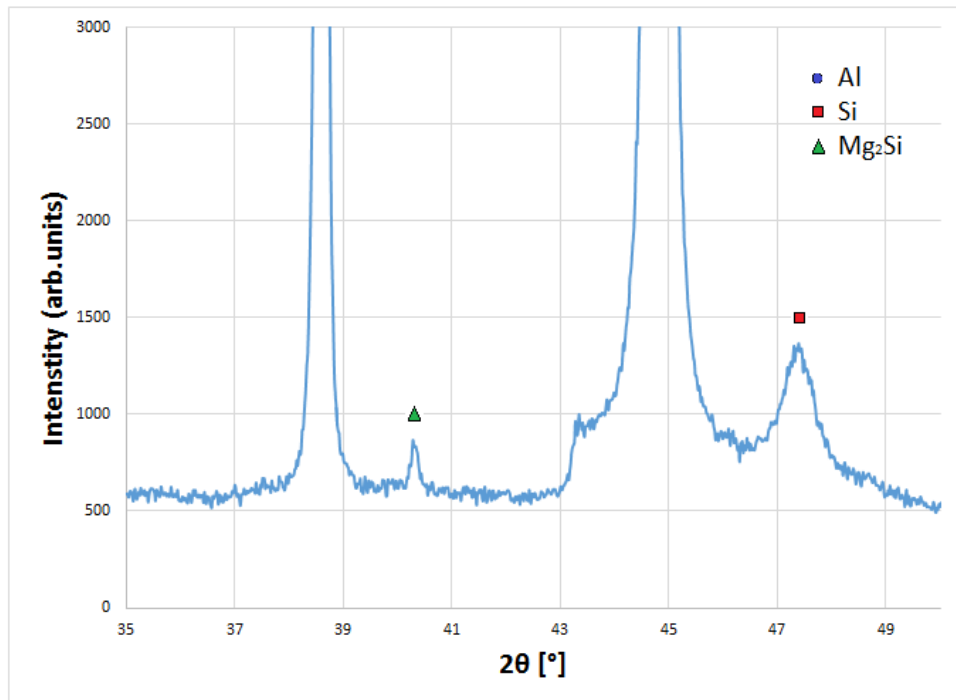
Fig.4.50: Close-up view of the Mg_2Si peak.

Similar results were found by L.P. Lam *et.al* (2015), during the phase analysis and microstructure characterization of AlSi10Mg parts produced via Laser Melting.

After the heat treatments, all samples were subjected to the XRD analyses in order to evaluate the effect of the temperature and duration of heat treatments on the microstructure, focusing the attention on the Al, Si and Mg_2Si peaks. Two set of heat treatments are separately considered, those having a duration of 30 minutes and those having a duration of two hours. In general, the width of the peak and shift of a peak have been evaluated. A peak shift means the distance between atomic planes has changed, and this phenomenon could be associated to the stress release.

Comparing the XRD analyses between them and analyzing the Al peaks, they all show a shift towards lower angles of reflection and an increasing of the width with increasing the temperature of heat treatment (Fig.4.51), except for the peak represented in Fig.4.52 where the reduction of the peak width, among untreated and treated samples, was found.

In Fig.4.51 (a), the increasing of the duration has the effect to further increase the peak width, shifting the peaks towards lower degrees of reflection. This phenomenon could mean that a better stress release considering 263°C and 294°C occurred, increasing the

heat treatment times. However, performing the heat treatment at 320°C the stress release occurred also in 30 minutes
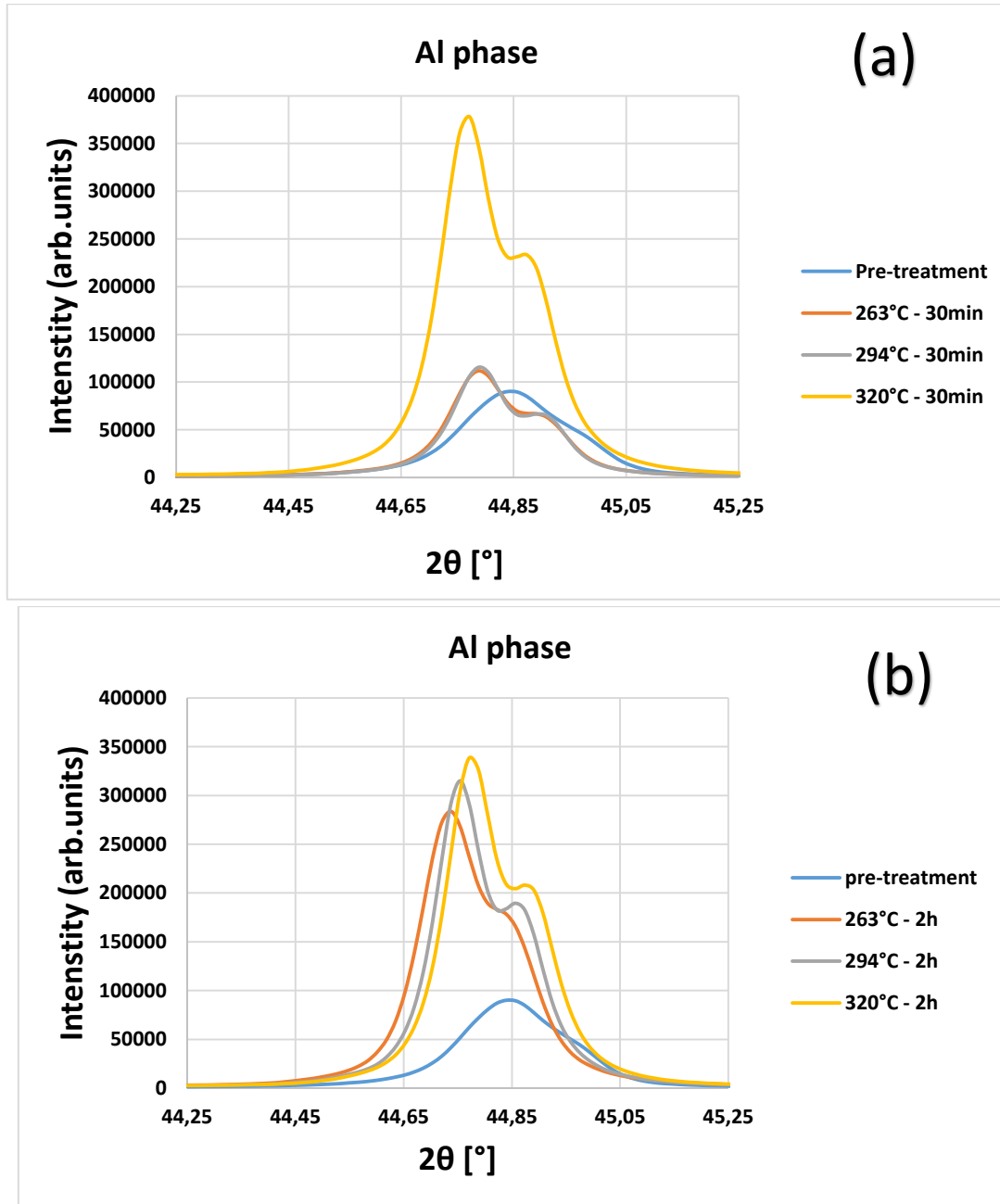
Fig.4.51: Diffractogram of AlSi10Mg sample considering different heat treatment conditions and just the Al phase. The peaks shift with increasing the temperature of heat treatment is appreciable. In figure (a) the duration is 30 minutes while in figure (b) the duration is 2 hours.
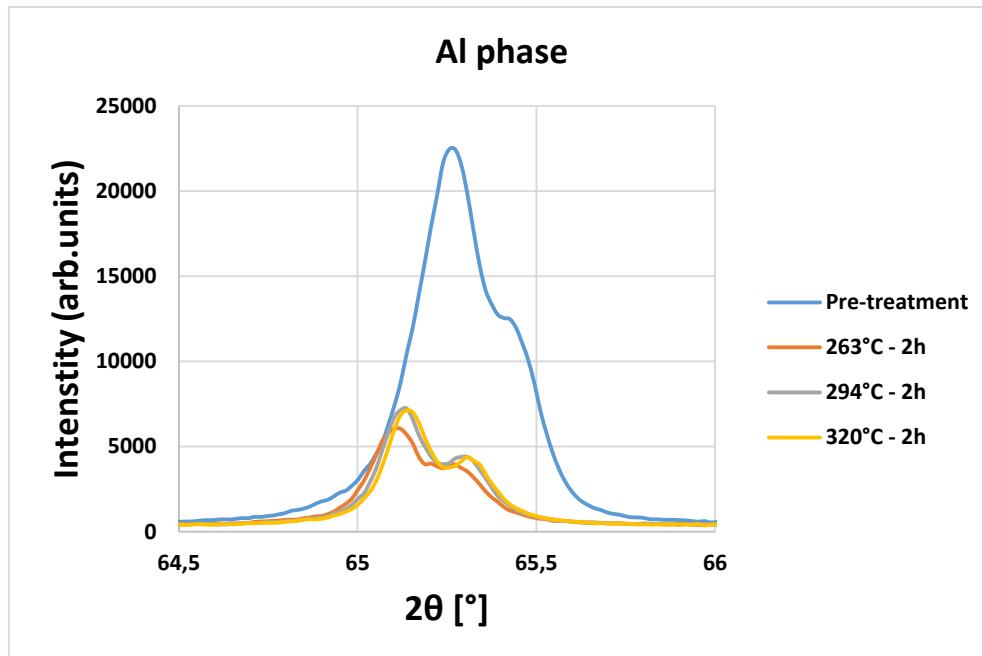
Fig.4.52: Diffractogram of AlSi10Mg sample considering different heat treatment conditions and just the Al phase. The peak shift untreated and heat-treated samples is visible.

As far as the Si phase is concerned, also in this case the peak width shows a reduction increasing the heat treatment temperature (Fig.4.53). This effect is more pronounced considering a duration of 2 hours (Fig.4.53 (b)).
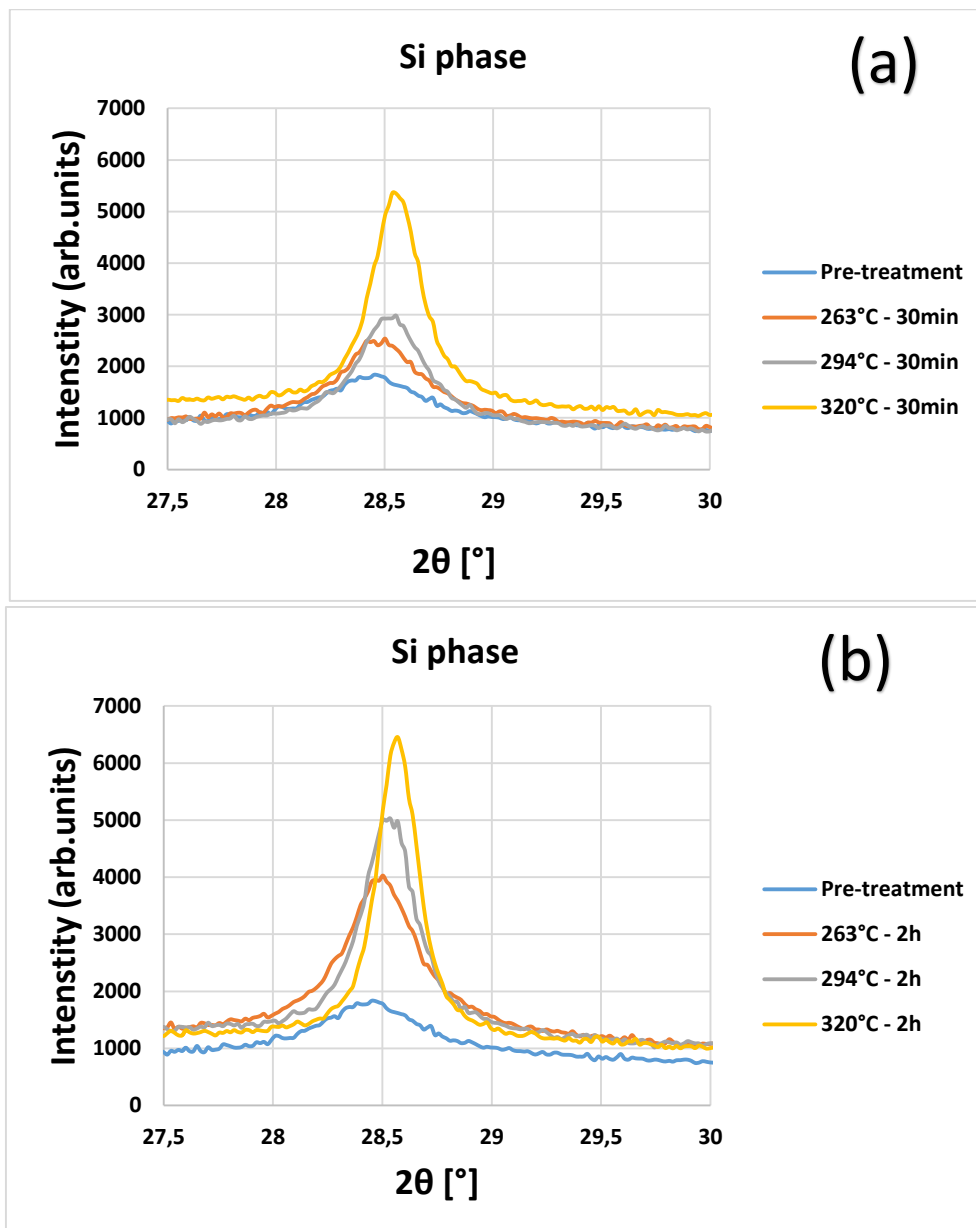
Fig.4.53: Diffractogram of AlSi10Mg sample considering different heat treatment conditions and just the Si phase. Intensity increasing and peak shifting are visible.

Also the Mg_2Si phas has been analyzed and no variations occurred considering the heat treatments with a duration of 30 minutes, exept for the heat-treatment performed with a temperature of 320°C (Fig.4.54) that shows an increasing of the widht. Different considerations can be made about the samples subjected to the heat treatments with a duration of 2 hours (Fig.4.55), where an increasing of peak hight occurred.
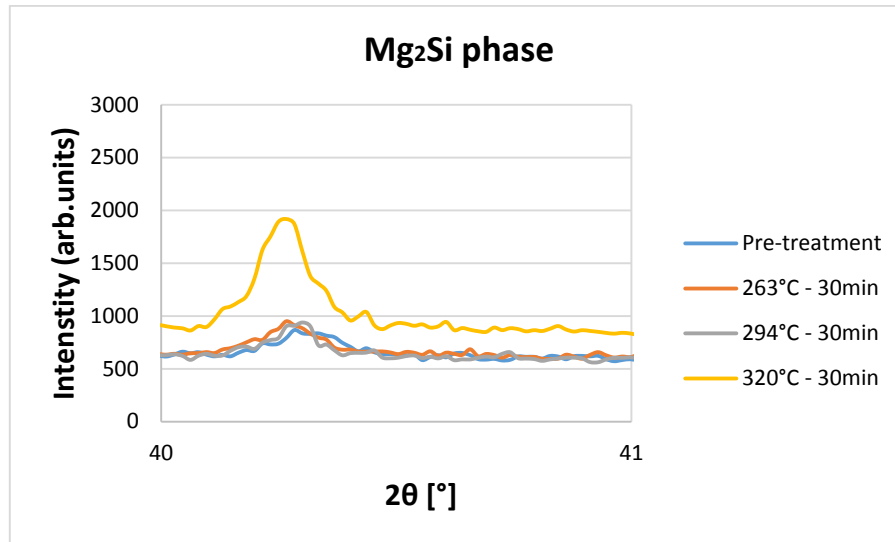
Fig.4.54: Diffractogram of AlSi10Mg sample considering different heat treatment conditions and just the Mg_2Si phase. Intentesity increasing is observed just in the heat treatment performed at 320°C.
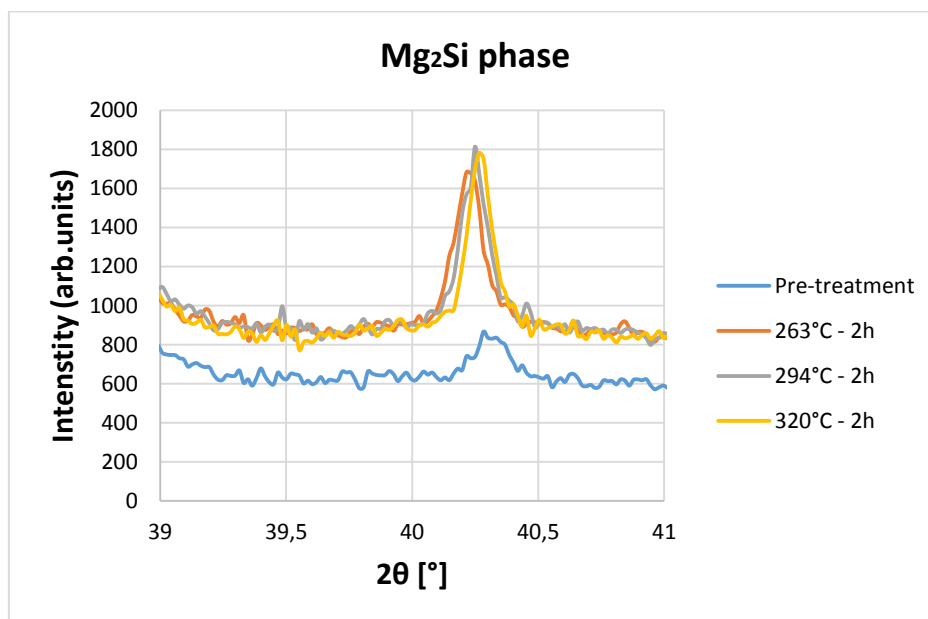
Fig.4.55: Diffractogram of AlSi10Mg sample considering different heat treatment conditions and just the Mg_2Si phase. Intentesity increasing and peaks shifting are visible.

After the XRD analyses, it is possible to state that a general peaks shift of the Al phase occurred. This shift could be associated to a stress release of residual tensions left by the laser melting process. Performing the heat treatment for 30 minutes, it is necessary to hold the material inside the furnace at 320°C to induce the stress release. For the other temperatures, it is necessary to select 2 hours as duration of the heat treatments, to induce stress release in the laser melted part. Connecting the results with that of the DSC analyses it is possible to state that, while the first exothermic reaction is reasonably a peculiarity of the material referred to the precipitation of Mg_2Si, the second exothermic reaction is dependent on the process conditions, which generate a state of residual stress concentration inside the fabricated part.

Chapter 5

Conclusion and Future Works

In this thesis the experimental characterization of AlSi10Mg alloy, produced via Laser Beam Melting technology has been performed.

The aim of this activity is to study the effects of the Power, Exposure Time and Build Plate Temperature on the samples density, morphology, chemical composition, microstructure and mechanical properties. Recent literature considers the aluminum powders a material that is not widely used in powder bed Laser Melting processes due to the number of difficulties in processing it by using this technology. However, being a technology in expansion, which is passing from the prototypes fabrication to the real production of components in different fields of application, with this thesis a further contribution is given to the research, trying to define a specific approach to investigate the feasibility area of the process, for the aluminum alloy.

Analyzing the collected results, several conclusions can be made about this thesis.

By varying the process parameters, the samples density is varied too. Through the statistical analysis of the variable conditions (Power, Exposure Time and Build Plate Temperature) it is possible to state that there is a strong correlation between samples density variation and Build Plate Temperature, in particular, increasing this latter one, the density reduces. The maximum relative density achieved is 97,82% with 300W of Power, 120μs of Exposure Time and without considering pre-heating of Build Plate. However, this result is not satisfactory considering that the relative density requirement for the components production, is at least 99%. Further increasing in these three process parameters causes a strong reduction in samples density.

The variation of Power, Exposure Time and Build Plate Temperature strongly influence the process stability. A further increasing of the selected process parameters causes the progressive enhancement of the process instability. This phenomenon intensifies the pores formation, due to the gas bubbles entrapment occurring during the solidification process, and hence interfering on the final density of the fabricated part. The effect of the increasing of the Build Plate Temperature causes a reduction in the pores density and, at the same time, an increasing in their size, hence a global reduction of the sample density.

The selected parameters do not induce a variation in the chemical composition of the fabricated samples, which have been compared to the one of the fresh powder (this is verified in EDS section analysis). This is confirmed also by the fact that no variation in the melting point occurs comparing samples fabricated in different process conditions.

During the Laser Melting process, the combined effect of directional cooling and rapid solidification induced by repeated thermal cycles, has a profound influence on the microstructures of the alloy, which presents fine grains, along the build direction (following the principle of epitaxial solidification), in the melted zone (MZ) (inside the melted-pool) and coarse grain in heat-affected zone (HAZ) and re-melted (RZ) (caused by the overlapping of the scan tracks). The microstructure strongly influences the resulting hardness of the fabricated samples. High Power and short laser-material interaction times determine high temperature gradients together with high cooling rates, resulting in a fine microstructure and high hardness, in fact the maximum hardness has been found with the following conditions: Power=400W, Exposure Time =120µs and Build Plate at room temperature. However, an increasing in the Build Plate Temperature causes the grains growth and induces a reduction of the hardness.

The hardness of heat treated samples, have been investigated and compared with the as-built sample. It shows a global reduction with increasing the temperature and time of heat treatments. Heat treating at 263°C for 30 minutes and 2 hours, results in a decrease of the hardness by almost 11%, heat treating at 294°C for 30 minutes and 2 hours, the hardness reductions are respectively by almost 18% and the 27% with respect the as-built sample. Further increases of temperature and duration cause a reduction of the hardness by 25% in treated sample at 320°C for 30 minutes, and by 35% in heat treated sample at 320 °C for 2 hours (both compared to the as-built sample).

Different SEM analyses of the samples subjected to heat treatments with a duration of 2 hours, were performed. The results show that no big differences in Si particles size and distribution were observed between the as-built sample and the one heat treated at 263°C. The network of Si phase is continuous in both cases. Performing the heat treatment at 294°C the Si phase starts to change morphology and the network becomes discontinuous as occurred at 320°C, where the Si particles tend to agglomerate increasing their size. The effects of the microstructural variations have been associated to the hardness variation of heat treated sample. The increasing in size of Si particles and the network discontinuity due to thermal treatment were no longer able to limit the dislocations motion as occurred in as-built sample. Considering the hardness reduction, it has been supposed that the effect of the stress release due to heat treatment was

predominant on the precipitation phenomenon (that would have to cause an increase of the hardness).

Carrying out heat treatments on a single sample (the one having the maximum density) by varying the temperatures and the time duration was identified the phase evolution through the XRD analysis. The phase evaluation was performed, verifying the diffractograms, first of all on the as-built sample and then on heat treated samples. The as-built sample revealed the α-Al and Si phases. Also small amount of Mg_2Si precipitates were present. After heat treatments a general increasing of peaks intensity related to the Al and Si phases was appreciable. It has been determined that 30 minutes is not a sufficient holding time to increase the Mg_2Si precipitate peak, as concern the 263°C and 294°C heat treatment temperatures, while with a temperature equal to 320°C the intensity peak of this phase increases. Performing heat treatments for 2 hours increases the amount of the precipitates of a nearly equal amount, independently by the heat treatment temperatures. A global peaks shifting after all heat treatments is present and it represents the stress release.

Performing the DSC analyses on samples fabricated with different process conditions, two exothermic reactions were present during the heating cycle. The nature of this reactions has been studied through further DSC analyses on the fresh powder and AlSi7Mg sample (fabricated via casting process), that revealed the presence of a single exothermic reaction having the same onset/offset temperatures of reaction present in laser melted samples. For these reasons, it has been supposed that the first peak is dependent on the material properties (Mg_2Si precipitation) while the second one is associated to fabrication conditions (Laser Melting process). These hypothesis were confirmed by the XRD analyses which revealed the presence of the Mg_2Si in as-built sample and the stress release (peak shifting) after the heat treatments. For these reasons it is possible to state that the first peak is associated to the precipitation phenomenon while the second one to the stress concentration induced by the laser melting process.

The Laser Melting process is a new technology with a great potential in the production field. This potential has been recognized by the market whose requirements are in continuous evolution, as said in the chapter concerning the goals of the work. They are passing from components compliance in terms of geometry and surface finish quality, to the satisfaction of the metallurgical and mechanical ones, that are more difficult to reach. This is the reason why the continuous improvement of this technology is fundamental.

Thus, possible points for future works are:

  - ➢ Implement the samples fabrication performed via Laser Melting technology in the industrial production field.
  - ➢ Find out the optimal set of *Fill Hatch* parameters and feasibility area of Laser Melting process, starting from the consideration of this thesis, trying to vary also other parameters that have been kept constant.
  - ➢ Find out the optimal set of *Border* and *Additional Border* parameters of Laser Melting process in order to respond to specific surface requirements.
  - ➢ Study the reduction of porosity during the Laser Melting process.
  - ➢ Study the reduction of porosity through post processing treatments (hot isostatic pressing process).
  - ➢ Formulate a specific heat treatment to reach desired mechanical properties of laser melted parts.

Bibliography

Abe F., Osakada K., Shiomi M., Uematsu K., Matsumoto M., The manufacturing of hard tools from metallic powders by selective laser melting, 2001.

Aboulkhair N.T., Everitt N.M., Ashcroft I., Tuck C., Reducing porosity in AlSi10Mg parts processed by selective laser melting, 2014.

Agarwala M., Bourell D., Beaman J., Marcus H., Barlow J., Direct selective laser sintering of metals, 1995.

Ammar H.R., Samuel A.M., Samuel F.H., Porosity and the fatigue behaviour of hypoeutectic and hypereutectic aluminum– silicon casting alloys, 2008.

Asgharzadeh H., Simchi A., Effect of sintering atmosphere and carbon content on the densification and microstructure of laser-sintered M2 high-speed steel powder, 2005.

Bassoli E., Sewell N., Denti L, Gatto A. Investigation into the failure of Inconel exhaust collector produced by laser consolidation, 2013.

Brandl E., Heckenberger U., Holzinger V., Buchbinder D., Additive manufactured AlSi10Mg samples using Selective Laser Melting (SLM): Microstructure, high cycle fatigue, and fracture behavior, 2012.

Buchbinder D., Schleifenbaum H., Heidrich S., Meiners W., Bultmann J., High power selective laser melting (HP SLM) of aluminum parts, 2012.

Calignano F., Design optimization of supports for overhanging structures in aluminum and titanium alloys by selective laser melting, 2014.

Cao X., Wallace W., Immarigeon J.P., Poon C., Research and progress in laser welding of wrought aluminum alloys, 2003.

Chlebus E., Kuz´nicka B., Kurzynowski T., Dybała B., Microstructure and mechanical behaviour of Ti–6Al–7Nb alloy produced by selective laser melting, 2011.

Collur M.M., Paul A., DebRoy T., Mechanism of alloying element vaporization during laser welding, 1987.

Dadbakhsh S., Hao L., Effect of Al alloys on selective laser melting behavior and microstructure of in situ formed particle reinforced composites, 2012.

Dadbakhsh S., Hao L., In-situ formation of particle reinforced Al matrix composite by selective laser melting of Al/Fe2O3 powder mixture, 2012.

Dadbakhsh S., Hao L., Jerrard P.G.E., Zhang D.Z., Experimental investigation on selective laser melting behavior and processing windows of in situ reacted Al/Fe2O3 powder mixture, 2012.

Dalgarno K.W., Wright C.S., Approaches to processing metals and ceramics through the laser scanning of powder beds – a review, 2001.

Daia D., Gua D., Effect of metal vaporization behavior on keyhole-mode surface morphology of selective laser melted composites using different protective atmosphere, 2015.

Das S., Physical aspects of process control in selective laser sintering of metals, 2003.

Deepak K. Pattanayak A., Fukuda, Matsushita T., Takemoto M., Bioactive Ti metal analogous to human cancellous bone: Fabrication by selective laser melting and chemical treatments, 2011.

Dongdong Gu., Shen Y., Balling phenomena in direct laser sintering of stainless steel powder: Metallurgical mechanisms and control methods, 2009.

Foroozmehr A., Badrossamay M., Foroozmehr E., Golabi S., Effect of metal vaporization behavior on keyhole-mode surface morphology of selective laser melted composites using different protective atmospheres, 2015.

Foroozmehr A., Badrossamay M., Foroozmehr E., Golabi S., Finite Element Simulation of Selective Laser Melting process considering Optical Penetration Depth of laser in powder bed, 2015.

Fischer P., Locher M., Romano V., Weber H.P., Kolossov S., Glardon R., Temperature measurements during selective laser sintering of titanium powder, 2004.

Fischer P., Roman V., Weber H.P., Karapatis N.P., Boillat E., Glardon R., Sintering of commercially pure titanium powder with a Nd:YAG laser source, 2003.

Ghosh S.K., Bandyopadhyay K., Saha P., Development of an in-situ multi-component reinforced Al-based metal matrix composite by direct metal laser sintering technique – optimization of process parameters, 2014.

Gu D., Hagedorn Y-C, Meiners W, Meng G, Joao R, Batista S., Densification behaviour, microstructure evolution, and wear performance of selective laser melting processed commercially pure titanium, 2012.

Gu D., Meiners W., Microstructure characteristics and formation mechanisms of in situ WC cemented carbide based hard metals prepared by selective laser melting, 2010.

Gu D., Shen Y., Balling phenomena during direct laser sintering of multi-component Cu-based metal powder, 2007.

Gu D., Shen Y., Processing and microstructure of submicron WC–Co particulate reinforced Cu matrix composites prepared by direct laser sintering, 2006.

Gu D., Shen Y., Wu X., Formation of a novel W-rim/Cu-core structure during direct laser sintering of W–Cu composite system, 2008.

Gusarov, A.V., Kruth, J.P., Modelling of radiation transfer in metallic powders at laser treatment, 2005.

Kathuria Y.P., Microstructuring by selective laser sintering of metallic powder, 1999.

Kempena K., Thijsb L., Van Humbeeckb J., J.-P. Krutha, Mechanical properties of AlSi10Mg produced by Selective Laser Melting, 2012.

Kobryn P.A., Semiatin S.L., Mechanical properties of laser-deposited Ti–6Al–4V, 2006.

Kruth J.P., Deckers J, Yasa E. and Wauthlé R., Assessing and comparing influencing factors of residual stresses in selective laser melting using a novel analysis method, 2012.

Kruth, J.P.; Froyen, L.; Morren, B. & Bonse, J.E., Selective laser sintering of WC-Co 'hard metal' parts, 1997.

Kruth J-P, Froyen L., Van Vaerenbergh J., Mercelis P., Rombouts M., Lauwers B., Selective laser melting of iron-based powder, 2004.

Kruth J-P, Levy G., Klocke F., Childs T.H.C., Consolidation phenomena in laser and powder-bed based layered manufacturing, 2007.

Kruth J-P., Mercelis P., Van Vaerenbergh J., Froyen L., Rombouts M., Binding mechanisms in selective laser sintering and selective laser melting, 2005.

Kumari S., Pillai R.M., Rajan T., Pai ., Effects of individual and combined additions of Be, Mn, Ca and Sr on the solidification behaviour, structure and mechanical properties of Al–7Si–0.3Mg–0.8Fe alloy, 2007.

Kyogoku H., Hagiwara M., Shinno T., Freeform Fabrication of Aluminum Alloy Prototypes Using Laser Melting, 2010.

Lam L.P., Zhang D.Q., Z.H. Liu & C.K. Chua, Phase analysis and microstructure characterisation of AlSi10Mg parts produced by Selective Laser Melting, 2015.

Leuders S., Thone M, Riemer A., Niendorf T., Troster T., Richard H.A., On the mechanical behaviour of titanium alloy TiAl6V4 manufactured by selective laser melting: fatigue resistance and crack growth performance, 2013.

Liu R., Dong Z., Pan Y., Solidification crack susceptibility of aluminum alloy weld metals, 2006.

Li X.P., Wang X.J., Saunders M., Suvorova A., Zhang L.C., Liu Y.J., Fang M.H., Huang Z.H., Sercombe T.B., A selective laser melting and solution heat treatment refined Al-12Si alloy with a controllable ultrafine eutectic microstructure and 25% tensile ductility, 2015.

Lott P., Schleifenbaum H., Meiners W., Wissenbach K., Hinke C., Bültmann J., Design of an Optical system for the In Situ Process Monitoring of Selective Laser Melting (SLM), 2011.

Louvis E., Fox P., Sutcliffe C.J., Selective laser melting of aluminum components, 2011.

Ma M., Wang Z., Gao M., Zeng X., Layer thickness dependence of performance in high-power selective laser melting of 1Cr18Ni9Ti stainless steel, 2015.

Mater A., create radically better products with design optimization and 3D Printing, 2015.

Mercelis P., Control of selective laser sintering and selective laser melting processes, 2007.

Mertens A., Dedry O., Reuter D., Rigo O., Lecomte-Beckers J., Thermal treatment of AlSi10Mg processed by Laser Beam Melting, 2015.

Monroy K., Delgado J., Ciurana J., Study of the pore formation on CoCrMo alloys by selective laser melting manufacturing process, 2013.

Morgan R., Papworth A., Sutcliffe C., Fox P., O'Neill W., High density net shape components by direct laser re-melting of single-phase powders, 2002.

Mrvar, Jožef Medved, Effect of Ce on solidification and mechanical properties of A360 alloy, 2011.

Nastase C., Comsa S., New considerations regarding the use of selective laser sintering technology for biomedical metallic implants, 2009.

Nelson T.W., Lippold J.C., Mills M.J., Nature and evolution of the fusion boundary in ferritic–austenitic dissimilar weld metals. Part I – Nucleation and growth, 1999.

Nesma T. Aboulkhaira, Nicola M. Everitta, Ian Ashcroftb, Chris Tuckb, Reducing porosity in AlSi10Mg parts processed by selective laser melting, 2014.

Niu H.J., Chang I.T.H., Selective laser sintering of gas atomized M2 high speed steel powder, 2000.

Nyahumwa C., Green N.R., Campbell J., The concept of the fatigue potential of cast alloys, 1998.

Olakanmi E.O., Cochrane R.F., Dalgarno K.W., A review on selective laser sintering/melting (SLS/SLM) of aluminium alloy powders: Processing, microstructure, and properties, 2015.

Olakanmi E.O., Cochrane R.F., Dalgarno K.W., Densification mechanism and microstructural evolution in selective laser sintering of Al–12Si Powders, 2011.

Olakanmi E.O., Selective laser sintering/melting (SLS/SLM) of pure Al, Al–Mg, and Al–Si powders: effect of processing conditions and powder properties, 2013.

Olakanmi E.O., Direct selective laser sintering of aluminum alloy powders, 2008.

O'Neill W., Sutcliffe C.J., Morgan R., Landsborough A., Hon K.K.B., Investigation on multi-layer direct metal laser sintering of 316L stainless steel powder beds, 1999.

Pinkerton A.J. and Li L., Direct additive laser manufacturing using gas- and water-atomised H13 tool steel powders, 2005.

Qian G., Hong Y., Zhou C., Investigation of high cycle and very-high-cycle fatigue behaviours for a structural steel with smooth and notched specimens, 2011.

Read N., Wang W., Essa K., Attallah M.A., Selective laser melting of AlSi10Mg alloy: process optimisation and mechanical properties development, 2015.

Rehme O., Emmelmann C., Selective Laser Melting of Honeycombs with Negative Poisson's Ratio, 2009.

Rosenthal I., Stern A., Frage N., Microstructure and Mechanical Properties of AlSi10Mg Parts Produced by the Laser Beam Additive Manufacturing (AM) Technology, 2014.

Ruidi Li & Jinhui Liu & Yusheng Shi & Li Wang & Wei Jiang, Balling behavior of stainless steel and nickel powder during selective laser melting process, 2012.

Sabina L. Campanelli, Nicola Contuzzi, Andrea Angelastro and Antonio D. Ludovico, Capabilities and Performances of the Selective Laser Melting Process, 2010.

Sanz-Guerrero J., Ramos-Grez J., Effect of total applied energy density on the densification of copper–titanium slabs produced by a DMLF process, 2008.

Savage W.F., Nippes E.F., Erickson J.S., Solidification mechanisms in fusion welds, 1976.

Schaffer G.B., Sercombe T.B., Lumley R.N., Liquid phase sintering of aluminum alloys, 2001.

Simchi A., Pohl H., Effect of laser sintering processing parameters on the microstructure and densification of iron powder, 2003.

Simchi A. , Petzoldt F., Pohl H., On the development of direct metal laser sintering for rapid tooling, 2003.

Spierings A.B., Herres N., Levy G., Influence of the particle size distribution on surface quality and mechanical properties in AM steel parts, 2011.

Srivastava D., Chang I.T.H., Loretto M.H., The effect of process parameters and heat treatment on the microstructure of direct laser fabricated TiAl alloy samples, 2001.

Stamp R., Fox. P, O'Neill W., Jones E. and Sutcliffe C., The development of a scanning strategy for the manufacture of porous biomaterials by selective laser melting, 2009.

Starink M.J., Analysis of aluminum based alloys by calorimetry: quantitative analysis of reactions and reaction kinetics, 2004.

Steen, W.M., Laser Material Processing, 2003.

Su W.N., Erasenthiran P., Dickens P.M., Investigation of fully dense laser sintering of tool steel powder using a pulsed Nd:YAG laser, 2003.

Thijs L., Verhaeghe F., Craeghs T., Van Humbeeck J., Kruth J.P., A study of the microstructural evolution during selective laser melting of Ti–6Al–4V, 2010.

Wang X.J., Zhang L.C., Fang M.H., Sercombe T.B., The effect of atmosphere on the structure and properties of a selective laser melted Al–12Si alloy, 2014.

Wang Y., Bergstrom J., Burman C., Characterization of an iron-based laser sintered material, 2006.

Wang Y, Bergstrom J, Burman C. Four-point bending fatigue behaviour of an iron-based laser sintered material, 2006.

Wei L., Shuai L., Jie L., Ang Z., Yan Z.,Qingsong W., Chunze Y., Yusheng S. , Effect of heat treatment on AlSi10Mg alloy fabricated by selective laser melting: Microstructure evolution, mechanical properties and fracture mechanism, 2016.

Weingarten C., Buchbinder D., Pirch N., Meiners W., Wissenbach K., Poprawe R., Formation and reduction of hydrogen porosity during selective laser melting of AlSi10Mg, 2015.

Yadroitsev I., Bertrand Ph., Smurov I., Parametric analysis of the selective laser melting process, 2007.

Yadroitsev I., Gusarov A., Yadroitsava I. and Smurov I., Single track formation in selective laser melting of metal powders, 2010.

Yadroitsev I., Krakhmalev P., Yadroitsava I., Johansson S., Smurov I., Energy input effect on morphology and microstructure of selective laser melting single track from metallic powder, 2013.

Yasa E., Kruth J.-P., Deckers J., Manufacturing by combining Selective Laser Melting and Selective Laser Erosion/laser re-melting, 2011.

Zhang B., Liao H, Coddet C., Effects of processing parameters on properties of selective laser melting Mg–9%Al powder mixture, 2012.

Zhang L.C., Klemm D., Eckert J., Hao Y.L., Sercombe T.B., Manufacture by selective laser melting and mechanical behavior of a biomedical Ti–24Nb–4Zr–8Sn alloy, 2011.

Zhao H., DebRoy T., Welding metal composition change during conduction mode laser welding of aluminum alloy 5182, 2001.

Zhu H.H., Lu L, Fuh J.Y.H., Influence of binder's liquid volume fraction on direct laser sintering of metallic powder, 2004.